



universität
wien

DISSERTATION / DOCTORAL THESIS

Titel der Dissertation / Title of the Doctoral Thesis

Self-associating hybrid polymers under shear

verfasst von / submitted by

Diego Felipe Jaramillo - Cano

angestrebter akademischer Grad / in partial fulfilment of the requirements for the degree of

Doktor der Naturwissenschaften (Dr. rer. Nat.)

Wien, 2020 / Vienna, 2020

Studienkennzahl lt. Studienblatt /
degree programme code as it appears on the student
record sheet:

A 796 605 411

Dissertationsgebiet lt. Studienblatt /
field of study as it appears on the student record sheet:

Physik

Betreut von / Supervisor:

Univ.-Prof. Dipl.-Ing. Dr. Christos N. Likos

Abstract

Star block-copolymers (SBCs) have been demonstrated to constitute self-assembling building blocks with specific softness, functionalization, shape, and flexibility. In this work, we study the behavior of an isolated SBC and suspensions of SBCs under shear flow by means of particle-based multi-scale simulations. We systematically analyze the conformational properties of low-functionality stars as well as the formation of attractive patches on their corona as a function of the shear rate. We cover a wide range of system parameters, including functionality, amphiphilicity, and solvent quality. Three mechanisms of patch reorganization under shear were identified, which determine the dependence of the patch numbers and orientations on the shear rate, namely, free arms joining existing patches, a fusion of medium-sized patches into bigger ones, and fission of large patches into two smaller ones at high shear rates. As well as, the dynamics of the SBC was investigated by means of the so-called Eckart's frame, which allows separating pure rotational and vibrational motions. It is shown that SBCs display a richer structural and dynamical behavior than athermal star polymers in a shear flow. We also investigated the behavior of dilute and semidilute suspensions of SBCs under linear shear flow for a wide range of parameters of the system; the latter include the monomer packing fraction. Our analysis focus on the dynamical behavior of the network structures formed at equilibrium as a consequence of the patch reorganization induced by the shear flow. The obtained results have interesting implications on the system's rheological properties and viscoelastic response in dilute and semidilute bulk phases because the SBCs are able to form a variety of different intermolecular transient bonds involving rather weak ones between individual arms and much stronger ones between multiarm patches. In the final part of this work, we propose two generalizations of the Multi-Particle Collision Dynamics (MPCD) numerical method, in the first we use the density profile information to obtain a polymer system with effective monomers in which we eliminate the monomer-monomer interaction, in the second we use a more advanced model called penetrable soft colloid, we design new collision rules for the interaction between the solvent and the penetrable soft colloid. We apply these two generalizations for linear polymers and star polymers, we compare the results of the mean square displacement, we find that our first approach is consistent with linear polymers while the second is consistent with polymer stars. Our approaches can be extended to more complex polymer systems.

Zusammenfassung

Sternblock-Copolymere (SBCs) sind geeignete Makromoleküle, um Selbstorganisation-Bausteine mit spezifischer Weichheit, Funktionalisierung, Form und Flexibilität zu bilden. In dieser Arbeit untersuchen wir das Verhalten eines isolierten SBC und Suspensionen von SBCs unter Scherströmung mittels partikelbasierter Mehrskalensimulationen. Wir analysieren systematisch die Konformationseigenschaften von Sternen mit niedriger Funktionalität sowie die Bildung attraktiver Flecken (Patches) auf ihrer Korona in Abhängigkeit von der Scherrate. Wir decken eine Vielzahl von Systemparametern ab, darunter Funktionalität, Amphiphilizität und Lösungsmittelqualität. Es wurden drei Mechanismen der Patch-Reorganisation unter Scherung identifiziert, die die Abhängigkeit der Patch-Zahlen und -Orientierungen von der Scherrate bestimmen, nämlich freie Arme, die bestehende Patches verbinden, eine Verschmelzung von mittelgroßen Patches zu größeren und die Spaltung großer Patches in zwei kleinere Patches bei hohen Scherraten. Zudem wurde die Dynamik des SBC mit Hilfe des sogenannten Eckart-Rahmens untersucht, der die Trennung reiner Rotations- und Schwingungsbewegungen ermöglicht. Es wird gezeigt, dass SBCs ein ausgeprägteres strukturelles und dynamisches Verhalten aufweisen als athermale Sternpolymere in einer Scherströmung. Wir untersuchten auch das Verhalten von verdünnten und halbverdünnten Suspensionen von SBCs unter linearem Scherfluss für einen weiten Bereich von Parametern des Systems; letztere schließen die Monomerverpackungsfraction ein. Unsere Analyse konzentriert sich auf das dynamische Verhalten der im Gleichgewicht geformten Netzwerkstrukturen als Folge der durch den Scherfluss induzierten Patches-Reorganisation. Die gewonnenen Ergebnisse haben interessante Auswirkungen auf die rheologischen Eigenschaften des Systems und die viskoelastischen Reaktionen in verdünnten und halbverdünnten Bulk-Phasen, da die SBCs in der Lage sind, eine Vielzahl verschiedener intermolekularer transientser Bindungen zu bilden, die eher schwache Bindungen zwischen einzelnen Armen und viel stärkere Bindungen zwischen Mehrarm-Patches beinhalten. Im letzten Teil dieser Arbeit schlagen wir zwei Verallgemeinerungen der numerischen Multi-Particle Collision Method (MPCD)-Methode vor; in der ersten verwenden wir die Dichteprofilinformation, um ein Polymersystem mit effektiven Monomeren zu erhalten, in dem wir die Monomer-Monomer-Wechselwirkung eliminieren, in der zweiten verwenden wir ein ausgeklugtes Modell, namens "durchdringbares weiches Kolloid", wir entwerfen neue Kollisionsregeln für die Wechselwirkung zwischen dem Lösungsmittel und dem durchdringbaren weichen Kolloid. Wir wenden diese beiden Verallgemeinerungen für lineare Polymere und Sternpolymere an, wir vergleichen die Ergebnisse der mittleren quadratischen Verschiebung und, wir finden, dass unser erster Ansatz mit linearen Polymeren konsistent ist, während der zweite mit Polymersternen konsistent ist. Unsere Ansätze können auf komplexere Polymersysteme ausgedehnt werden.

Acknowledgements

I would like to express my sincere gratitude to my advisor Prof. Christos Likos for his continuous and unconditional support in the development of my Ph.D studies. His patience, motivation, and immense knowledge helped me to successfully complete my thesis. I thank my TAC mentor Prof. Manuel Camargo, who was permanently willing to kindly answer all my questions, their support and help were of great importance for the completion of my Ph.D. studies.

I am very grateful to the European Training Network COLLDENSE (H2020-MCSA-ITN-2014, Grant No. 642774) and to the Dissertation Completion Fellowship Programme of the University of Vienna for their financial support, which was crucial to carry out this work. The computer time at the Vienna Scientific Cluster (VSC) is gratefully acknowledged.

Last but not least, I would like to thank my family: my parents, to my sisters, brother, and brother-in-law, for supporting me spiritually during the writing of this thesis and my life in general. Feeling your affection and love has made my stay away from home much easier. Finally, I have to thank all the people who in one way or another contributed to the development of this work.

Preface

The research in this thesis has been published in five papers, which constitute the following chapters:

- **Chapter 3**

- Diego Jaramillo-Cano, Maud Formanek, Christos N. Likos, and Manuel Camargo, *Star Block-Copolymers in Shear Flow*. The Journal of Physical Chemistry B, 2018, 122 (14), 4149-4158 , DOI: 10.1021/acs.jpcc.7b12229.
- Diego Jaramillo-Cano, Christos N. Likos, Manuel Camargo, *Rotation Dynamics of Star Block Copolymers under Shear Flow*. Polymers 2018, 10, 860; DOI:10.3390/polym10080860.

- **Chapter 4**

- Ioana C. Gârlea, Diego Jaramillo-Cano and Christos N. Likos, *Self-Organization of Gel Networks Formed by Block Copolymer Stars*, Soft Matter 15, 3527-3540 (2019). DOI: 10.1039/c9sm00111e.
- Diego Jaramillo-Cano, Manuel Camargo, Christos N. Likos, and Ioana C. Gârlea, *Dynamical properties of concentrated suspensions of block copolymer stars in shear flow*, submitted for publication.

- **Chapter 5**

- José Ruiz Franco, Diego Jaramillo Cano, Manuel Camargo, Christos N. Likos, and Emanuela Zaccarelli, *Multiparticle collision dynamics for a coarse-grained model of soft colloids*, Journal of Chemical Physics 151, 074902 (2019). DOI: 10.1063/1.5113588.

Contents

Abstract	iii
Zusammenfassung	v
Acknowledgements	vii
Preface	ix
1 Introduction	1
1.1 Soft matter	1
1.2 Soft matter rheology	2
1.3 Associative polymers	7
1.4 Star Block Copolymers - (SBCs)	8
1.5 Thesis Outline	9
2 Model and methods	11
2.1 Introduction	12
2.2 Monomer-resolved model for polymers (MRM)	12
2.3 Star Block Polymers method (SBC)	13
2.3.1 Equilibrium properties of SBC	14
2.3.1.a Gyration tensor	14
2.3.1.b Density profile	16
2.3.1.c Patches behavior	17
2.3.2 SBCs system - protocol	19
2.4 Multi Particle Collision Dynamics - MPCD	20
2.4.1 MPCD parameters	21
2.5 Hybrid Program - MD+MPCD	22
2.5.1 Shear rate	22
3 Isolated SBC	25
3.1 Introduction	26
3.2 Model paramters	27
3.3 Geometric properties	27
3.4 Patches behaviour	31
3.5 Rotational frequency	37
3.5.1 Laboratory frame (LF)	37
3.5.2 Eckart frame (EF)	39

CONTENTS

3.5.3	Hybrid frame (HF)	42
3.5.4	Geometrical approach (GA)	43
3.5.5	Global conformation and dynamics	44
3.5.6	Reference configuration update	44
3.5.7	Angular momentum and angular frequency	48
3.6	Conclusions	52
	Appendix 3A: Rotation frequencies	54
	Appendix 3B: Kinetic energy in the Eckart frame	55
	Appendix 3C: Explicit calculation of T_u	56
4	Semidilute and concentrated regimes	58
4.1	Introduction	59
4.2	Model and Methods	60
4.3	Equilibrium Properties	61
4.3.1	Network Structure and Pair Correlations	61
4.3.2	Patch and network characteristics	66
4.4	Dynamical Properties	76
4.4.1	General behavior under shear	76
4.4.2	Geometrical properties	77
4.4.3	Radial correlation functions	82
4.4.4	Patches behavior	85
4.4.4.a	Connectivity	89
4.4.5	Viscosity	91
4.5	Conclusions	92
5	MPCD for a coarse-grained model of soft colloids	95
5.1	Introduction	96
5.2	Methods	99
5.2.1	Multi-Particle Collision Dynamics	99
5.2.2	Effective monomer model (EMM)	100
5.2.3	Soft colloid MD-MPCD simulations	101
5.2.3.a	Coupling between solvent and colloids	102
5.3	Results	105
5.3.1	Monomer and solvent density profiles	105
5.3.2	Results for linear chains	108
5.3.3	Results for star polymers	111

CONTENTS

5.3.4 Effects of core on the dynamics of the penetrable soft colloid model for star polymers	114
5.4 Conclusions	115
5.5 Appendix 5A: Radius of gyration and moment of inertia	117
Appendix 5A: Radius of gyration and moment of inertia	117
6 Conclusion and Outlook	120
Bibliography	123

1 | Introduction

1.1 Soft matter

In recent years research in the field of soft matter, as a subfield of condensed matter, has been of great interest, due to its wide range of applications in the development of new materials with a rich and wide range of equilibrium and dynamical properties. The study of soft matter is based on the study of complex fluids [1–4], where the most relevant physical properties occur in the energy scale of the order of the thermal energy at room temperature [4]. Complex fluids are typically composed of mesoscopic particles which span characteristic length scales from about 1nm (monomer size) to macroscopic scales of about 1mm, dispersed in a solvent consisting of particles typically of atomic characteristic length scale [4]. A central part of the study and a rich area of research is the combination of polymeric mesoscopic systems with colloids [2, 5, 6]. Given the difference in characteristic length scales, systems in the field of soft matter present a wide range of characteristic times [4], the dynamics of solvent particles are much faster than the diffusive processes of monomer or colloidal particles, so a complete description of the degrees of freedom of the solvent is not very efficient both theoretically and computationally. Numerical techniques have been developed [7, 8], where the dynamics of the solvent particles and the interaction between the solvent and the monomers or colloids are simplified (incorporating hydrodynamic interactions), numerical hybrid simulations with results according to experimental results, which have generated efficient methods in the numerical treatment. Similarly, in theoretical developments, specific interaction potentials have been generated where the effect of the solvent is considered as a mediator [4] between the colloid-colloid interaction.

The main systems of interest in soft matter physics research are flexible polymers, with different topologies and properties. Among the most studied systems are linear polymers, ring polymers [9, 10], polymer stars [11, 12], micelles [13, 14], dendrimers [15, 16], as well as hard colloid systems (hard spheres) such as patchy particles [17–19], other systems are liquid crystals and other mesoscopic constituents [3]. Polymers are composed of chemical units called monomers [3]. The typical number of monomers present in a polymer can be thousands, however, for macropolymers or macro-molecules this number can be much higher and reach millions of chemical units. The properties of polymers are governed by the pair interaction potential between monomers. To move from a complex description of the chemical unit to a simpler description the coarse grained description is known [4], each monomer is completely defined by its center of mass and the solvent is treated in an implicit way obtaining monomer resolved description. Similarly, one can use information from a macromolecule to consider it as a single soft sphere and describe its dynamic behavior only with its center of mass.

In linear polymers, it is considered that the monomer is spherical and elastic connections are associated between consecutive monomers, the aggregation of linear polymers creates the

1 INTRODUCTION

branched polymer or network polymer (cross-linked) [3]. Stars polymer are an aggregation of linear polymers where the first monomer of each linear polymer is linked by an elastic potential to a central monomer called the star's core. In soft matter physics, the physics description is more relevant than the chemical details in most cases [1], since all the systems of study present properties that are studied from statistical physics, all the polymers and colloids present Brownian motion, all the interactions between the systems of interest in soft matter physics can be modeled by means of effective potentials. One of the systems with greater current interest are the proteins of the DNA and RNA, modeled as bio-polymers [20–22], in this model the fundamental chemical unit is related to the nucleotides [3], the DNA and RNA can be represented by means of polymers of repeated chains of nucleotides.

The usual form of classification of materials is based on materials soluble in water (hydrophilic), whereas those that like oil (oleophilic - hydrophobic) are not soluble in water [3]. There is a class of materials with a great richness in both structural and dynamic properties, known as amphiphilic materials or surfactants (surface activating agents). These are molecules that have a hydrophilic and a hydrophobic part connected chemically to each other. The general objective of this doctoral dissertation is the structural and dynamic study of a type of amphiphilic star, i.e., a star polymer that consists of a hydrophilic part adjacent to the core of the star followed by a hydrophobic part [23–28]. Other types of amphiphilic material are micelles (micelle joints), vesicles and tubules.

1.2 Soft matter rheology

The study of complex fluid rheology aims to find the constitutive equation, that is, it aims at describing the intrinsic behavior of the complex fluid independent of the specific condition to which it is submitted [29]. In other words, it focuses on the viscoelastic properties of the materials [30]. Microrheology studies how materials store and dissipate mechanical energy as a function of scale length [30]. Microrheology extends the study of rheology by considering the dynamic behavior of materials as a function of the scale length, and it is closely related to the field of microfluids [30]. The applications of complex fluids are impressive, clear examples of this are, in the industrial field, the choice of viscosity for a new shampoo formula or new compounds that change the properties of cement for new challenges in construction; in the medical field, new ways of encapsulating and transporting drugs in the bloodstream; in the food field, design of new attachments so that in the baking of cakes, they experience several phase transitions [30]. A current field of research in rheology deals with colloidal dispersions [31]. Generally speaking, when talking about colloids we refer to a two-component system, in which the elements of the dispersed phase are so small that they are easily observed by optical microscopes [31] and are affected by thermal forces, while in the continuous phase (suspension medium) it is liquid, not easily sedimented, colloidal suspensions are a complex type of fluid.

1 INTRODUCTION

Due to the works of Albert Einstein (1905) on Brownian movement, Marian Smoluchowski (1906) on colloidal aggregation, and G. B. Batchelor (1970) on the suspension of free particles, the framework of study for the rheology of colloidal suspensions is completed [31]. This is a combination between statistical mechanics and the theory of hydrodynamics. The fundamental unit of energy in the colloidal description is the thermal energy $k_B T$, which has two main consequences, the first is the osmotic pressure. For an ideal gas is evident in the equation of state,

$$P = nk_B T \quad (1.1)$$

with n the density number of the atoms. For diluted systems of colloidal dispersions, by analogy, we obtain van Hoff's law,

$$\Pi = nk_B T, \quad (1.2)$$

where Π is the osmotic pressure. In the same way, it is possible to define an adimensional parameter to define the elasticity of the particle (ξ),

$$\xi = \frac{\Delta F}{k_B T} \quad (1.3)$$

where ΔF is the elastic free energy, ξ defines the ability of the particle to deform or compress as a result of external factors such as flow or temperature [32]. The second consequence is the force due to random collisions between molecules of the suspension medium and colloidal particles (Brownian Force = F_B) which is also defined in terms of thermal energy [31],

$$F_B = \frac{k_B T}{r_a} \quad (1.4)$$

where r_a is the colloid radius (assumed to be spherical), F_B is responsible for the diffusive motion. Starting from the mean square displacement,

$$\lim_{t \rightarrow \infty} \langle (\Delta r(t))^2 \rangle = 6Dt, \quad (1.5)$$

where D is known as the Einstein-Smoluchowski diffusion coefficient, for spherical colloids, we obtain the Stokes-Einstein-Sutherland coefficient [31],

$$D_0 = \frac{k_B T}{6\pi\eta_m r_a}, \quad (1.6)$$

where η_m is the viscosity of the suspending medium. When a force is applied to the system, it generally undergoes a deformation. In a solid phase, the system presents a deformation and eventually a rupture. The mechanical behavior of solid

1 INTRODUCTION

materials is described in terms of the deformation induced by the applied stress. To study the deformation in materials it is useful and easy to apply a simple shear [29], in which, a piece of material is contained between two parallel plates which have relative movement. The shear stress σ is defined as the ratio between the applied force F_{xy} (the first sub-index indicates the direction of the force and the second defines the plane of force application [31]) and the section of force application S ,

$$\sigma = \frac{F_{xy}}{S}, \quad (1.7)$$

while the deformation ε is defined as the ratio between the relative displacement Δx between the planes and the perpendicular distance between the planes $y_{max} = H$.

$$\varepsilon = \frac{\Delta x}{H}. \quad (1.8)$$

The constitutive equation for this type of material is a combination of the two previous equations, resulting in

$$\frac{\sigma}{\varepsilon} = \frac{F_{xy}H}{\Delta x S} = G, \quad (1.9)$$

where G is known as the elastic modulus, for this case it is equal to Young's modulus.

In the case of the complex fluid, for the simple flow condition (linear flow), the interstitial liquid is contained between two parallel planes, as explained above, the relative velocity between the planes is low enough to avoid turbulence, the velocity of the neighboring fluid layers of the parallel plates will have the same velocity of the respective plate (non-slip condition), the velocity gradient is a constant, known as the shear rate $\dot{\gamma}$:

$$\dot{\gamma} \equiv \frac{dv_x}{dy} = \frac{v_r}{H} \quad (1.10)$$

In this case, shear stress is a function of shear rate, the constitutive equation for fluids is Newton's law for viscosity [29],

$$\sigma_{xy} = \eta \dot{\gamma} \quad (1.11)$$

This equation represents the intrinsic relationship between stress and the dynamic behavior of the fluid, it should be noted, that this equation will be valid only for Newtonian fluids [29]. For the Non-Newtonian liquids, the viscosity is not constant, and it can depend on the temperature or the applied stress. Non-Newtonian liquids present a more complicated behavior, nevertheless, the

1 INTRODUCTION

apparent viscosity (η_a) can be calculated, as the ratio between the shear stress and the shear rate,

$$\eta_a = \frac{\sigma}{\dot{\gamma}}. \quad (1.12)$$

For general systems, in which there is a wide range of mesoscopic elements and several types of interactions, these systems usually present a disoriented structure, so it is very difficult to find the constituent equation, a relationship between the local and the macroscopic behavior [29, 31]. The above is valid as long as the Reynolds number (Re) is much less than 1, which guarantees laminar flows, the Re number is defined as the ratio between the inertial force and the viscous force. For Re values greater than 1, the flow becomes turbulent. The usual rheology techniques are valid for $Re \ll 1$, i.e. in the complex fluid, both the mesoscopic elements and the interstitial fluid must be in the laminar regime.

For suspensions, mesoscopic elements dispersed in Newtonian liquids, when applying a simple shear, the fluid velocity field describes trajectories that depend on the geometric shape of the mesoscopic elements, but it can be shown that if the distribution of elements and space remains isotropic and constant, the suspension is Newtonian [29].

A useful state variable for the study of suspension behavior is the volume fraction (ϕ) which is the ratio between the volume of the elements and the total volume of the sample. When the packing fraction is low enough, the suspension is in the diluted regime, in this regime the mesoscopic elements of the suspension are far from each other, when applying the shear rate, the liquid flows around each element and is disturbed a distance less than the separation distance between the mesoscopic elements, so that hydrodynamic interaction is negligible [29], in this case, the suspension has a rheological behavior similar to that of interstitial fluid, in this case, a good approximation for viscosity is,

$$\eta(\phi) = \eta_0(1 + 2.5\phi) \quad (1.13)$$

This approach is really good for $\phi < 2\%$ [29]. For semi-diluted regimes, the rheological behavior depends on the behavior of both mesoscopic elements and interstitial fluid, for a Newtonian material, there are several empirical formulas that describe the viscosity behavior of the material, a special case is the Krieger-Dougherty equation (for a range of solid fractions greater than 55% [29]),

$$\eta(\phi) = \eta_0 \left(1 - \frac{\phi}{\phi_m}\right)^{-2.5\phi_m}, \quad (1.14)$$

where ϕ_m is defined as the maximum packing fraction, the maximum packing fraction value that can be achieved with mesoscopic elements. It should be noted that the ϕ_m parameter depends on the distribution and geometry of the elements, and may depend on the flow history, i.e. there

1 INTRODUCTION

is no suitable method to determine the exact value of ϕ_m . An approximate value can be derived with the help of the graph of viscosity vs. solid fraction, from the equation (Eq. 1.14), the value of ϕ_m corresponds to the value of the concentration for which the viscosity tends to infinity [29].

In the concentrated regime, the mesoscopic elements are very close, so there is a strong interaction between them. The rheological behavior of the material depends strongly on the type of interaction between the elements; in some cases the behavior of the interstitial liquid becomes negligible, so the suspension can lose its Newtonian character. In this case, the behavior of the material is complex and there is dependence on the flow history. The main source of viscous dissipation can vary from friction between elements to hydrodynamic dissipation with the interstitial liquid since among the mesoscopic elements there is a small layer of fluid [29].

For many non-Newtonian fluids, the apparent viscosity may vary with shear rate, and with flow history, the viscous dissipation is now modified by flow [29]. This type of fluids does not satisfy Newton's law, so the constitutive equation is given by the Navier-Stokes equations [31]. In the case of soft polymers, the elements can be deformed and take new geometrical forms changing their orientation, which will depend on the properties of the applied flow. For example, linear polymers or stars polymer tend to align in the direction of flow and, likewise, the flow can now generate rotation of such objects. For non-Newtonian fluids where the shear stress is completely defined by the instantaneous shear rate, but the relationship is not linear, these fluids are known as generalized Newtonian fluids [31]. Two types of mechanical behaviors can be distinguished [29]: for the first behavior, the alignment arises almost instantaneously for a given flow value and depends strongly on the shear rate, the material presents the "shear-thinning" behavior, the viscosity decreases when the shear rate increases. This is the most frequent rheological behavior in suspensions [31]. The second behavior is the opposite case known as shear-thickening. In this case, the viscosity increases when the shear rate increases, and it occurs for high volume fractions or for high values of the shear rate. These behaviors are related by a non-linear equation between shear stress and shear rate,

$$\sigma \sim \dot{\gamma}^n \tag{1.15}$$

In this equation the power law, for $n < 1$ represents shear-thinning behavior, and for $n > 1$ shear-thickening [31]. In the second behavior, the alignment takes some time and in this case, the apparent viscosity varies in time, in this case, the material presents the "thixotropic" behavior [29].

One of the main objectives in this dissertation is the study of the dynamic properties of isolated Star Block Copolymer (SBC) in order to understand the rheology of the diluted suspensions of SBCs. Of course, in *chapter 4*, we presented and analyzed the viscosity as a function of the shear rate and discuss the implications of the found shear thinning behavior.

1.3 Associative polymers

Associative polymers have segments that have the property to associate in the presence of selective solvents [33, 34]. The distribution of these segments in the polymers can be random or following a specific order, and this drastically influences the static and dynamic properties of the polymer [34]. Associative polymers have adjustable properties which provide a convenient control on the physical properties of both the polymer and the solution containing them. Accordingly, the applications of associative polymers have great industrial importance as rheological modifiers [33], one of the most studied applications being the change of viscosity of solutions [34]. There are different types of associative polymers, three of the most studied are the ones containing charged blocks (ionomers, polyelectrolytes), block polymers dependent on the quality of selective solvents, and associative polymers with hydrogen bonds [33].

In this doctoral dissertation, we study the static and dynamic properties of an associative polymer, which is composed of linear block polymers. In this case, there is only one associative block (B type - solvophobic block) connected by a soluble block (A type - solvophilic). For linear block polymer systems, B type blocks are grouped in dense domains above a Critical Association Concentration (CAC) and/or a Critical Association Temperature (CAT) [34] in a wide range of morphologies and/or geometries. Depending on the properties of the polymers, the concentration, the number of attractive blocks, the size ratio between B type and A type blocks, the solvent quality and the type of bond, the spherical or tube-shaped dense domains are the most common [34]. Similarly, when the surfactant molecules are assembled, the polymeric micelles (spherical dense domains) or worm-shaped micelles (barred dense domains) are reached [34].

In a system of associative polymers, the association of B type blocks is generated by two types of physical bonds that in principle are reversible, as opposed to permanent chemical bonds. The physical bonds can be weak, so the grouping of B type blocks can be formed and eliminated at a certain time. On the contrary, when the physical bonds are strong, the aggregation of B type blocks remains in time, these type of bonds can be destroyed by changing some of the parameters of the experiment [33].

A simple case study is that of linear block polymers with only two blocks, A-type and B type. For selective solvents, the B type block collapses into a dense spherical nucleus connected to a linear polymer consisting of A block. This configuration is known as the tadpole type, and in high concentrations, the dense spherical nuclei assemble and generate the micelle nucleus, Around the core, a crown of A-type block is generated, this type of configuration is similar to a star polymer, and it is called a micelle. The micelles can have different geometries depending on the asymmetry between the A-type and B type blocks or the quality of the solvent. By changing the micellar concentration, the system can present periodic structures of different morphologies and with different rheological properties [33].

1 INTRODUCTION

In dilute solutions of associative polymers, the phenomenon of self-association or self-assembly occurs. Different B type blocks are assembled, resulting in changes in the geometry of the polymer, in physical properties, and likewise in the dynamics of the polymer, such as a change in the frequency of rotation for when the system is applied a simple flow. For high concentrations the systems can form a gel phase; likewise, the type of gel will depend on the type of physical bonds present in the system. When the interaction is weak, it is found that the properties of the system are close to those of the viscoelastic fluids, but when the interaction is strong the properties are close to the soft polymers where a finite elastic module is present [33]. By increasing the number of B-blocks or by increasing the intensity of the attraction force between B-blocks, phase separation can be induced in the system.

The typical parameter for the study of the dynamics of the association polymers is the number of weak bonds formed in the polymer; this parameter is also useful for calculating the average time to generate this bond. In the case of a linear block polymer, this time is related to the time for which a solvophobic block needs to escape from a micelle and attach it to another micelle. This process involves two stages: first, the solvophobic block is removed from the core of the first micelle, and in the second the linear polymer block must be ejected from the micellar corona [33].

1.4 Star Block Copolymers - (SBCs)

Polymers have a wide range of macromolecular architectures [35]. Star polymers are linear polymer aggregates, the first monomer of each linear polymer is linked to the core of the star or central monomer, so that star polymers are a class of branched macromolecules with linear arms. Thanks to current synthesis techniques it is possible to synthesize star polymers in an easy way [35], star polymers have more important properties in different fields of application, especially in the field of nanotechnology [35–37], than linear polymers.

One way of classifying possible star polymer architectures is based on the properties and sequences of the monomers of each arm and the properties of the nucleus or central polymer [35]. There are three different categories for such classification. The first one is based on the distribution of the monomers in each arm of the star: in this category, there are the Homopolymer Star (HS), where all the monomers of the arms have the same properties, and the Star Block Copolymer (SBC) where each arm of the star has two different types of monomers, each type is grouped by blocks of the same type of monomers, and all the star arms are equal. In the second category, the way of classification depends on the different types of star arms: in this category are the so-called Miktoarm Star (MS), if in the star there are only two types of arms, this configuration is known as Compositional Miktoarm Star (CMS). The third category depends on the properties of the nucleus or central monomer of the star: if the nucleus of the star has similar characteristics to the monomers of each arm, this configuration is known as Small Compound Core-Structured Star (SCC-SS), if on

1 INTRODUCTION

the contrary, the nucleus is associated with macromolecular properties, this type of configuration is known as Macromolecule Core-Structured Star (MCS-SS) [35].

In this doctoral research, we focus on the type of star polymer with SBC architecture, since SBC's have been encountered in a wide range of systems due to the possible geometries of nanoparticles used in different applications, including micelles, nanospheres, nanocapsules among others [36]. One of the most interesting and appealing applications of nanoparticles is in the delivery of drugs, where these are considered as the next generation of drug carrier agents [36, 38–40].

As mentioned above, with current synthesis techniques it is easy to create large types of star polymer geometries, there are basically three types of approaches to synthesizing them, which are, nucleus-first, arm-first, or grafting-on [35, 36]. For the synthesis of the type of star used in this doctoral study (SBC), the first nucleus approximation is mainly used. Here, the nucleus of the star is a presynthesized multifunctional initiator and the arms of the star grow from the nucleus. With this, the first block of each arm is synthesized and when the desired length of the block is obtained, the chain is extended. Subsequently, to each arm of the star, the second block is added, finally synthesizing the SBC [35].

1.5 Thesis Outline

This Dissertation is organized as follows: in *chapter 2*, we briefly present the model and the simulation technique as well as some results about the equilibrium properties of isolated SBC. In *chapter 3*, we analyzed our numerical results for the geometric features of SBCs under shear rate. Particular attention is subsequently being paid to the question of patch reorganization as a consequence of shear. In the final part of this chapter, we focus on the dynamics of sheared SBCs analyzed using the so-called Eckart frame, which allows separating pure rotational and vibrational motions. We show that SBCs display a richer structural and dynamical behavior than athermal star polymers in a shear flow and therefore they are also interesting candidates to tune the viscoelastic properties of complex fluids. In *chapter 4*, in the initial part of the chapter, we analyze our results on the association, network formation and connectivity characteristics, pair correlations, and equilibrium diffusion of semi-dilute SBCs system for different values of the packing fraction. In the final part, we devoted to extensively present and discuss our results regarding the conformation properties, the patchiness, and the viscosity of the system as a function of the shear rate and the packing fraction. In *chapter 5*, we propose two new approaches to MD-MPCD simulations of macromolecular systems suspended in a solvent. Finally, in *chapter 6* we summarize and draw several concluding remarks.

2 | Model and methods

In this chapter, we present a brief description of all the computational methods used in this doctoral dissertation. All the computational models were written in the FORTRAN-95 high-level programming language. In the initial part of this chapter, the numerical method used to model purely repulsive stars (Monomer-Resolved Model - MRM) is presented, this model was used to model stars and linear polymers that were used in chapter 5 of this dissertation. With a modification of the MRM method, it is possible to model the behavior of a star blocks copolymer (SBC), that is, to modify the potential of pair interaction between monomers since now in the star are found two types of monomers, the solvophilic type (type - A) and the solvophobic type (type - B). When modifying the potential of interaction between type-B monomers, a parameter is introduced to simulate the quality of the solvent or, equivalently, to modulate the strength of the attractions between type-B monomers. In the second part of this chapter, the method to simulate isolated SBC with implicit solvent is presented, In addition, some results of the equilibrium of isolated SBC are presented varying the parameters of the model. To the previous model, the hydrodynamic interaction can be added, this means, we introduce an explicit solvent in the simulation. The hybrid method of simulation MD+MPCD employed in subsequent chapters. Finally, we present the protocol to find the initial configuration of semi-diluted and concentrated systems of a stars block copolymer with hydrodynamic interaction, used in chapter 4 of this dissertation.

2.1 Introduction

Computational science is a main part of the so-called modern sciences. A particular brand of it is computational physics, having applications in fields of great interest of current research, such as the field of solid-state physics, soft matter physics, fluid physics, nonlinear physics or dynamics of chaotic systems, quantum physics, cosmology, and others. The purpose of computational physics is the generation of computational models of systems of many particles or many degrees of freedom, which in principle do not have an exact analytical solution, or systems which properties are unknown under some specific conditions, i-e, rare events or with a low probability of occurrence. Of course, in computational physics, idealized or simplified models are developed to study properties of physical observables by statistical averaging.

In this doctoral dissertation, we study SBC employing molecular dynamics [41] where the integration method is the velocity-Verlet algorithm, using the Lees-Edwards algorithm to generate the linear shear flow in the system. The rest of the chapter is organized as follows. In *Sec. 2.2* We define the pair interaction potential for purely repulsive monomers and the potential to link two consecutive monomers for the construction of linear polymers. In *Sec. 2.3* We present the modification of the pair interaction potential between monomers (two types of monomer) and introducing the quality of the solvent, as well as numerical results for the equilibrium properties of an isolated star block copolymer with implicit solvent. In the final part of this section, we define the protocol to find the initial configuration for the semi-dilute and concentrated SBC systems regimes. In *Sec. 2.4* we define the algorithm for the implicit solvent that we used throughout the doctoral study as well as the main parameters of this algorithm. In *Sec. 2.5* We define how to implement the hybrid method of numerical simulation as well as the general implementation of the shear flow.

2.2 Monomer-resolved model for polymers (MRM)

Polymers are represented with a bead-spring-like model, where monomers are treated as soft spheres (ss) of diameter σ and mass M interacting through a Weeks-Chandler-Andersen-like pair potential,

$$V_{ss}(r) = \begin{cases} 4\epsilon \left[\left(\frac{\sigma}{r}\right)^{48} - \left(\frac{\sigma}{r}\right)^{24} + \frac{1}{4} \right] & r \leq r_{\text{cut}} \\ 0 & r > r_{\text{cut}}, \end{cases} \quad (2.1)$$

where $r_{\text{cut}} = 2^{1/24}\sigma$, $\epsilon = 2k_B T$ and r is the center-to-center distance between the monomers. Bonding between connected monomers is introduced by means of the finitely extensible nonlinear

2 MODEL AND METHODS

elastic (FENE) potential:

$$V_{\text{bond}}(r) = -\frac{1}{2}K \left(\frac{R_0}{\sigma}\right)^2 \ln \left[1 - \left(\frac{r}{R_0}\right)^2 \right], \quad (2.2)$$

where we fix $K = 30\epsilon$ and $R_0 = 1.5\sigma$.

2.3 Star Block Polymers method (SBC)

We simulate an isolated SBC with a modification of the MRM in the way introduced in [23]. Each arm of the SBC (f) is represented with N_A (solvophilic) inner and N_B (solvophobic) outer monomers ($N_{\text{pol}} = N_A + N_B$), therefore defining the amphiphilicity of the star as $\alpha = N_B/N_{\text{pol}}$. The monomers interacting through pair potentials $V_{AA}(r) = V_{AB}(r) = V(r; 0)$ and $V_{BB}(r) = V(r; \lambda)$ (Fig. 2.1) where,

$$V(r; \lambda) = \begin{cases} V_{ss}(r) + (1 - \lambda)\epsilon & r \leq r_{\text{cut}} \\ \lambda V_0(r) & r > r_{\text{cut}}. \end{cases} \quad (2.3)$$

We consider $k_B T$ and σ as units of energy and length, respectively, the unit of mass is M the mass of the monomer and λ is an attraction-controlling coupling constant, which allows us to modulate the solvent quality for the B-monomers; as explained in [23], to take $\lambda > 0.92$ is equivalent to considering that a polymer made of B-monomers is below its θ -temperature.

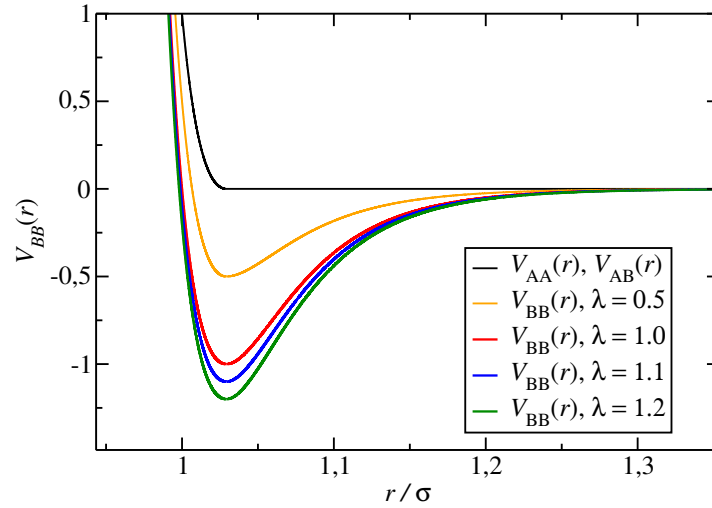


Figure 2.1. Plot of the pair interaction potential between solvophobic monomers for different values of λ , see eq. (2.3)

2 MODEL AND METHODS

2.3.1 Equilibrium properties of SBC

We used Molecular Dynamics (MD) simulation to model the SBC with implicit solvent. In this way, the time evolution of the monomers is described by Newton's equations of motion, which are integrated with the Velocity-Verlet scheme [41] using an integration time step $\Delta t = 10^{-3}\tau$, with $\tau = \sqrt{M\sigma^2/(k_B T)}$ ($M = 1$) being the time unit. We implement the Nose-Hoover Thermostat with $k_B T = 1$. We perform computational simulations with a several sets of the parameter, for the polymerization degree we chose $N_{\text{pol}} = 40, 60, 100$, for amphiphilicity $\alpha = 0.3, 0.5, 0.7$, functionalization $f = 12, 21, 30$ and, solvent quality $\lambda = 0.9, 1.0, 1.1$.

The main idea about the calculation of the equilibrium properties of the isolated SBC is testing the program that we implement in FORTRAN 95. We presented some numerical calculation of the shape, density profile, patches behavior, we define a patch as the aggregation of two or more blocks of type-B monomers, and the distribution of the $\cos(\theta)$, where θ is the angle between the center of mass of two patches, We found similar results reported in [23], the typical behavior of the SBC as a function of the λ is depicted in Fig. 2.2, we found some a set of parameters that the SBC has the soft patchy particle model behavior.

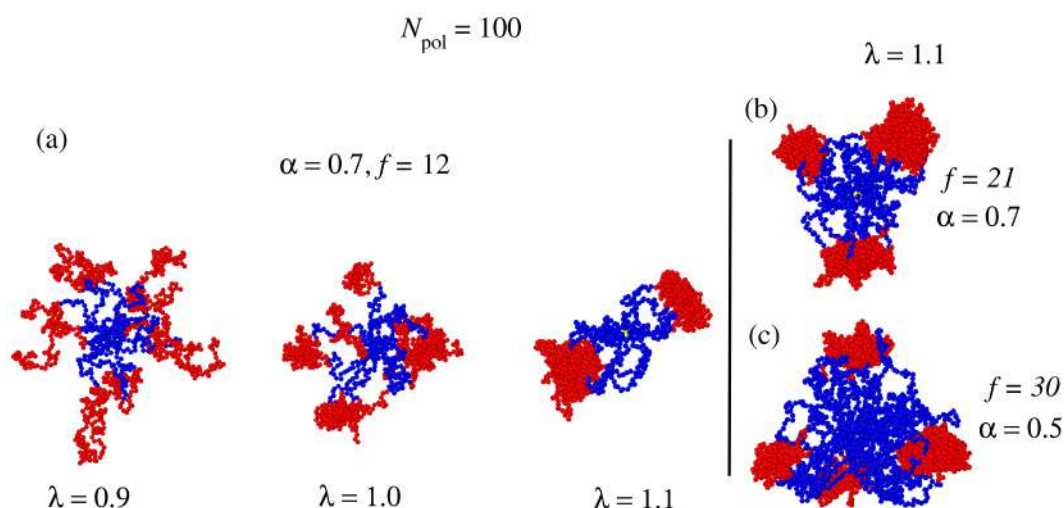


Figure 2.2. Snapshots of isolated SBC [42], (a) patches formation as a function of λ , SBC with the triangular (b) and tetrahedral (c) shapes. Yellow, red and blue spheres correspond respectively to the star core, solvophobic (B-type) monomers and solvophilic (A-type) monomers.

2.3.1.a Gyration tensor

One of the main results in the doctoral research is the complete analysis of the shape of an isolated SBC in shear flow and suspensions of SBCs in equilibrium and in shear rate. To accurately describe the shape of SBC we make use of the three eigenvalues $\lambda_1 > \lambda_2 > \lambda_3$ of the gyration

2 MODEL AND METHODS

tensor, which reads:

$$G_{\mu\nu} = \frac{1}{N_{\text{mon}}} \sum_{i=1}^{N_{\text{mon}}} (r_{i,\mu} - r_{\text{cm},\mu})(r_{i,\nu} - r_{\text{cm},\nu}), \quad (2.4)$$

where $r_{i,\mu}$ and $r_{\text{cm},\mu}$ are the μ components ($\mu = 1, 2, 3$ represent Cartesian coordinates) of the positions of the i -th monomer and of the star center of mass, respectively. The three eigenvalues can be used to define the following invariants:

$$\begin{aligned} I_1 &= \lambda_1 + \lambda_2 + \lambda_3, \\ I_2 &= \lambda_1\lambda_2 + \lambda_2\lambda_3 + \lambda_1\lambda_3, \\ I_3 &= \lambda_1\lambda_2\lambda_3. \end{aligned} \quad (2.5)$$

The first invariant corresponds to the square of the radius of gyration ($R_{\text{gyr}} = \sqrt{\langle I_1 \rangle}$). With the help of these invariants we can define the asphericity δ , the prolateness S , and the acylindricity c as:

$$\delta = 1 - 3 \left\langle \frac{I_2}{I_1^2} \right\rangle, \quad (2.6)$$

$$S = \left\langle \frac{(3\lambda_1 - I_1)(3\lambda_2 - I_1)(3\lambda_3 - I_1)}{I_1^3} \right\rangle, \quad (2.7)$$

$$c = \left\langle \frac{\lambda_2 - \lambda_3}{I_1} \right\rangle, \quad (2.8)$$

where the angular brackets denote ensemble averages [43–45]. The asphericity δ assumes values from 0 to 1, where the lowest value corresponds to a fully spherical object. The prolateness S ranges from -0.25 to 2, the negative values indicating oblate shapes whereas the positive ones map to prolate objects. The acylindricity is a positively defined quantity with $c = 0$ describing a perfect cylindrical symmetry; note, however, that also a perfect sphere has vanishing acylidricity.

In Fig. 2.3 we show that all values of the radius of gyration increase when f increases. For low values of α , the behavior of the SBC has a similar behavior as the completely repulsive stars. For $\alpha = 0.3$, $f = 30$ and all values of N_{pol} , the SBC has the spherical-like shape, the values of the δ and c are close to zero. When the parameter α increase, special case $\alpha = 0.5, 0.7$, $f = 21$ and $N_{\text{pol}} = 100$, c takes the maximum value, in this cases, the geometric shape on average becomes more close to cylindrical shape (see Fig. 2.2 (b)).

An interesting behavior is for $\alpha = 0.7$, the asphericity δ and de prolateness S in most cases decrease when f increase, nevertheless, the acylindricity c has different trends as a function of N_{pol} and f . The first one is for $N_{\text{pol}} = 40$, the trend is decreasing when f increases, while f increases

2 MODEL AND METHODS

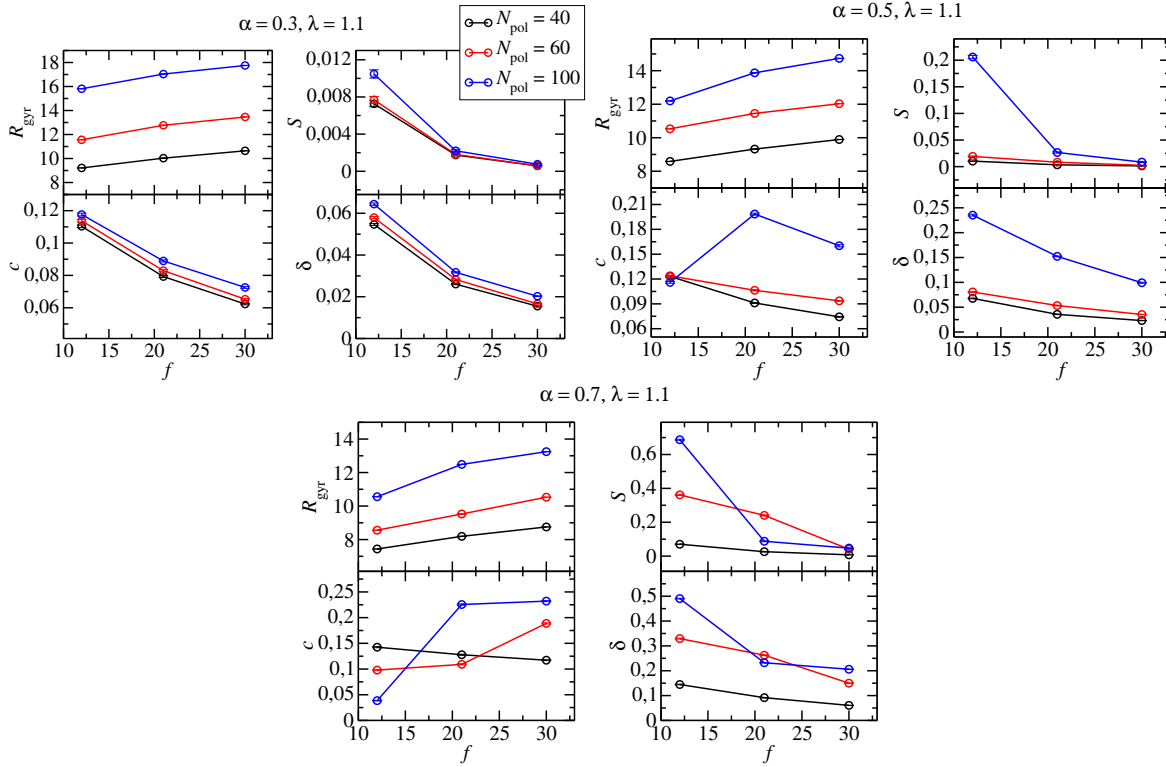


Figure 2.3. Shape parameters for an isolated SBC with, (Left-Up) $\alpha = 0.3$, (Right-Up) $\alpha = 0.5$, (Down) $\alpha = 0.7$, in all cases $\lambda = 1.1$.

the SBC tends to be more spherical. The second one for $N_{\text{pol}} = 60$, for values of $f < 21$, c remains almost constant and for $f > 21$, c increase with f . The third one for $N_{\text{pol}} = 100$, there is a rapid growth for $f < 21$, and for $f > 21$ the three shape parameter are saturated, the average geometry of the SBC is independent of f , for these values, the SBC preserves the triangular shape (Fig. 2.2 (b)).

2.3.1.b Density profile

In the last part of the doctoral research work we explored a new possible computational technique to simulate star polymer from the information obtained from the density profile (Chapter 5). For the moment, we calculated the density profiles of all sets of the parameter, finding, for values of $\alpha = 0.3$ all stars have the same density profile as complete repulsive star, we find the same decay law $\rho(r) \sim r^{-4/3}$ (Chapter 5 Sec. 5.3.1). However, for values of $\alpha = 0.7$ the tail of the distribution presents an important change with respect to the distribution for $\alpha = 0.3$, this change evidences the presence of patches of monomers (type - B) for all values of N_{pol} considered Fig. 2.4.

2 MODEL AND METHODS

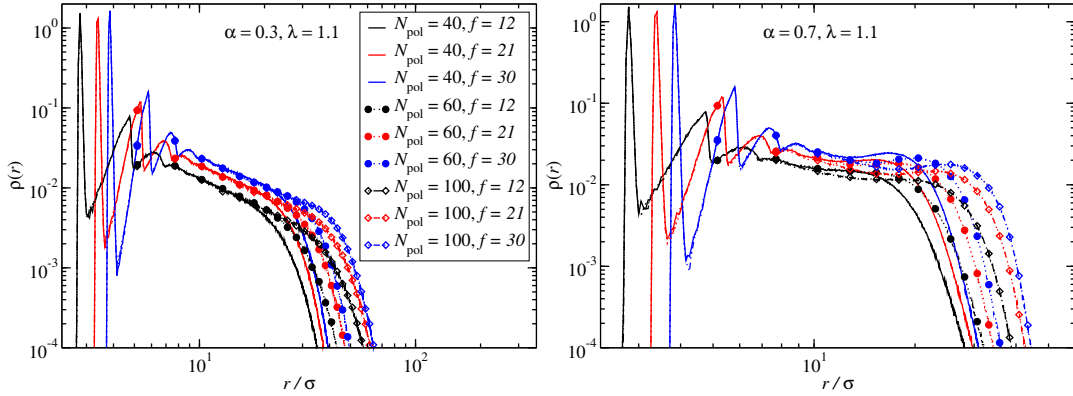


Figure 2.4. Density profile around the center of the SBC.

2.3.1.c Patches behavior

One of the changes induced by the amphiphilicity parameter α is the modification in the conformation shape of the SBC. This due to the creation of patches by the solvophobic tail of the SBC. Another main point in this research is the study of the dynamic behavior of the patches of type-B monomers. As mentioned above, we defined a patch as the aggregation of two or more solvophobic blocks. The criterion was chosen on the basis of the minimum distance between monomers type B of different blocks of the star. In particular, if two monomers of different blocks are at a distance $r_{\text{cutoff}} \leq 1.08\sigma$ we consider that the two blocks are united by a patch. In Fig. 2.5 we present the behavior of the patches and the number of type-B monomers present in each patch (population of the patches).

Fig. 2.5 shows the behavior of the number of the patches and the population of the patches on average, where we only considered configurations in which the SBC presents at least one patch. For $\alpha = 0.3$, the patches are on average made only for two arms and the average time of life of the patch counted in molecular dynamics steps is only a few steps: these patches are counted only by the proximity of the arms of the SBC. In the case of $\alpha = 0.5$ the size of the patches increases and these patches are more stable as shown in Fig. 2.2 (c), in this case, all arms of the star participate in the patches, this is only for the value of $N_{\text{pol}} = 100$ and $f = 30$, for the other values stable patches can be presented together with free arms. For the last value of $\alpha = 0.7$ in all cases, the system always presents stable patches (see Fig. 2.2 (a), $\lambda = 1.1$) and in this special case a smaller number of patches is found on average than in the case of $\alpha = 0.5$. The conformation of the patches produces changes in the geometric properties of the SBC. For the last value of α , the number of patches is saturated around four patches for values of $N_{\text{pol}} = 40$ with a spherical-like geometry of the SBC, and three patches for $N_{\text{pol}} = 100$ with a cylindrical-like geometry of the SBC.

To complete the study of the equilibrium properties of an isolated SBC with an implicit solvent, we calculate the distribution of $\cos(\theta)$ as long as the SBC has two or more patches Fig. 2.6.

2 MODEL AND METHODS

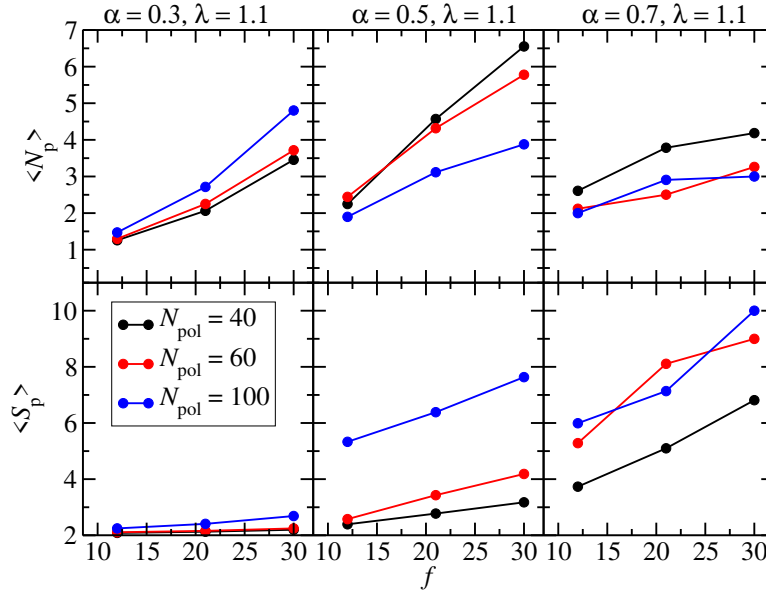


Figure 2.5. Averages number of Patches $\langle N_p \rangle$ and arms participating in a patche $\langle S_p \rangle$ as a function of f .

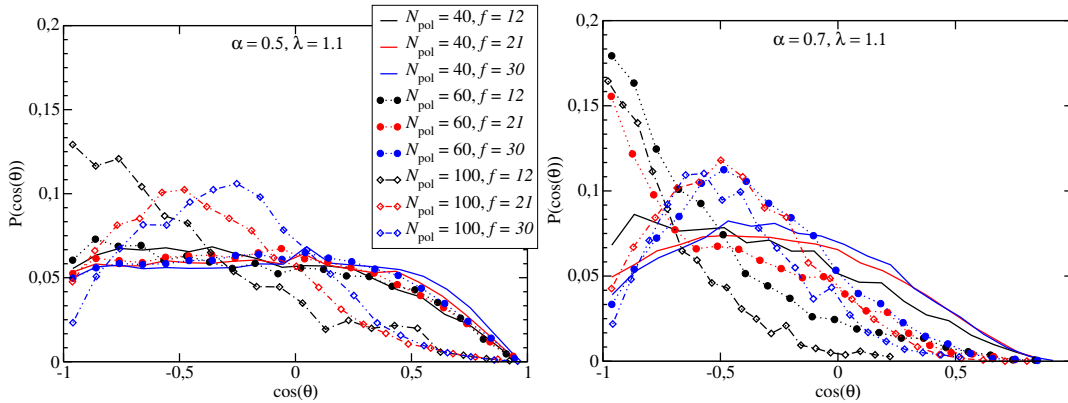


Figure 2.6. Distribution of the $\cos(\theta)$.

For values of $\alpha = 0.3$, the distribution of $\cos(\theta)$ is completely flattened because the dynamics of the patches consist of continuous creation and destruction, there is no explicit order in the same. For values of $\alpha = 0.5$ the distribution has the same behavior as for $\alpha = 0.3$, except for $N_{\text{pol}} = 100$, where we see a transition of the most probable value of $\cos(\theta)$ as a function of f . For $f = 12$ the most probable value of $\cos(\theta)$ is -1 , this signifies that the angle between the patches is 180 degrees, this is consistent with Fig. 2.5, the SBC has two patches, on average each patch has a size of 5 arms and these patches are diametrically opposite. When the value of $f = 21$, the most probable value of $\cos(\theta)$ takes the value of -0.5 , this implies that the angle between patches is around 120 degrees, the SBC presents 3 patches and presents the triangular-like configuration Fig. 2.5. For $f = 30$ the most probable value of the cosine of the angle is around -0.25 , This

2 MODEL AND METHODS

involves a pyramidal-like configuration Fig.2.2 (c). All the results presented are consistent with [23]. We found a similar behavior for $\alpha = 0.7$, however, for this value, the SBC has a maximum of 3 patches with a triangular shape of the SBC Fig. 2.5.

2.3.2 SBCs system - protocol

In *chapter 4* of this doctoral dissertation, where our main results are presented, we study the properties in equilibrium and the dynamic properties of SBC systems in semi-dilute and concentrated regimes. In this section, the algorithm used to find the initial configuration is explained. For the SBCs system, the algorithm that was chosen is divided into three parts. In the first part an arrangement of a body-centered cubic network is used, where, in each position of an atom completely stretched SBC is located, in such a way that the shortest distance between two close neighbors is such that they are considered isolated SBCs Fig. 2.7. In this part, $\lambda = 0$, and the model used is the MRM. We proposed for the first equilibration and thermalization step $MD_{\text{steps}} = 5 \times 10^6$ in molecular dynamics steps.

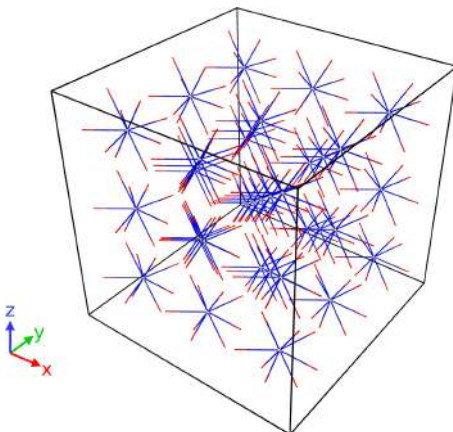


Figure 2.7. Snapshots from the simulation for the first part. In the left are 35 repulsive stars completed stretched.

In the second part, the simulation box is compressed until the desired monomer density (ϕ) is reached, followed by the introduction of the explicit solvent (using the MPCD algorithm, *Sec. 2.4*) and $\lambda = 0$, with which the algorithm in this step is the MRM+MPCD hybrid method (*Sec. 2.5*), again $MD_{\text{steps}} = 5 \times 10^6$ is used for equilibration and thermalization of the system. Fig. 2.8.

In the final part of this protocol, the value of the λ -parameter, modeling solvent quality changes to the desired value, and at this point, the final hybrid algorithm of MD + MPCD is used using the potential associated with the SBC. In this last stage, we used $MD_{\text{steps}} = 8 \times 10^6$ for thermalization and equilibration. In Fig. 2.9 initial conditions are observed for two sets of parameters in a concentrated regimen. For the study of dynamic properties, the shear flow is applied to the previous initial conditions through the Lees-Edwards boundary conditions (*Sec. 2.5.1*) where shear is applied

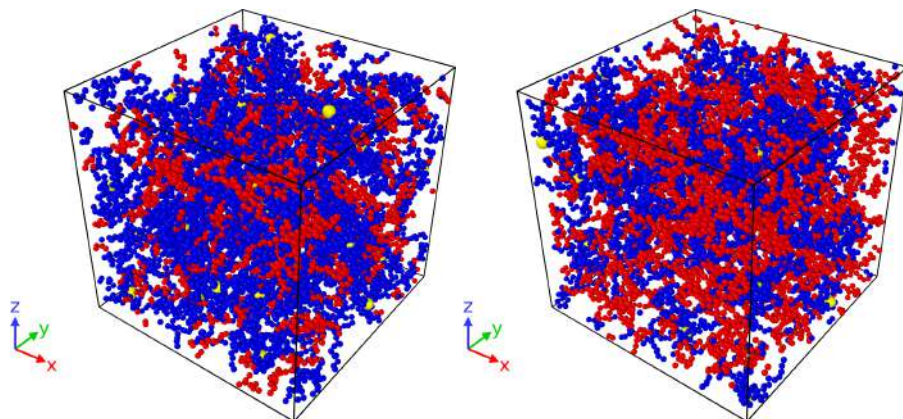


Figure 2.8. Snapshots from the simulation, for the second part of the protocol. In the left the parameters are $\alpha = 0.3$ and $\phi = 0.06$, in the right the parameters are $\alpha = 0.5$ and monomer volumen fraction $\phi = 0.06$.

gradually until the desired value of the shear flow is reached, adding another $\text{MD}_{\text{steps}} = 8 \times 10^6$ for thermalization and equilibration.

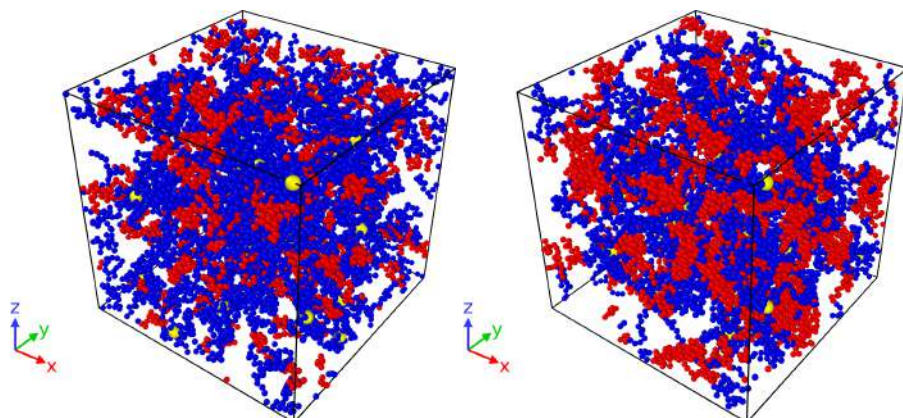


Figure 2.9. Snapshots from the simulation, for the last part of the protocol. For the same parameters of Fig. 2.8.

2.4 Multi Particle Collision Dynamics - MPCD

Multi-particle collision dynamics (MPCD) was employed to mesoscopically simulate the solvent [7, 8, 46]. The latter is assumed to be composed of N_s point-like particles of mass m , whose dynamics follow two steps: first, a streaming step, in which the solvent particles move ballistically as,

$$\mathbf{r}_i(t+h) = \mathbf{r}_i(t) + h \mathbf{v}_i(t) \quad (i = 1, \dots, N_{\text{sol}}), \quad (2.9)$$

where h denotes the time interval between collisions and \mathbf{r}_i and \mathbf{v}_i represent respectively the

2 MODEL AND METHODS

position and the velocity of the i -th solvent particle. Second, a collision step, in which the solvent particles exchange linear momentum. To do that, particles are sorted into cubic cells with length a , and their relative velocities with respect to the cell center-of-mass are rotated by an angle χ around a random axis [7, 8, 47].

$$\mathbf{v}_i(t+h) = \mathbf{v}_{\text{cm}}(t) + \hat{\mathcal{R}}(\chi)[\mathbf{v}_i(t) - \mathbf{v}_{\text{cm}}(t)], \quad (2.10)$$

where $\hat{\mathcal{R}}(\chi)$ is the corresponding rotation operator and \mathbf{v}_{cm} is the center-of-mass velocity of the cell to which particle i belongs. This is defined as

$$\mathbf{v}_{\text{cm}} = \frac{1}{N_c} \sum_{j=1}^{N_c} \mathbf{v}_j, \quad (2.11)$$

with N_c the number of the solvent particles within the cell. Hydrodynamic interactions are reproduced if both local momentum conservation and Galilean invariance are guaranteed. While the first requirement is satisfied immediately by Eq. (2.10), for the second one a random mesh shift of the collision cells must be performed before each collision step [48]. The average number of solvent particles per collision cell $\langle N_c \rangle$, the collision angle χ and the MPCD time step h determine the bulk number density $\rho_{\text{sol,bulk}} = \langle N_c \rangle / a^3$, the mass density $\hat{\rho}_{\text{sol}} = m \langle N_c \rangle / a^3$ and the (dynamic) viscosity of the solvent $\eta_{\text{sol}} = \eta_{\text{kin}} + \eta_{\text{col}}$, where

$$\begin{aligned} \eta_{\text{kin}} &= \frac{\langle N_c \rangle k_B T h}{a^3} \left[\frac{5 \langle N_c \rangle}{(\langle N_c \rangle - 1)(4 - 2 \cos \chi - 2 \cos(2\chi))} - \frac{1}{2} \right] \\ \eta_{\text{col}} &= \frac{\langle N_c \rangle m}{18 a h} (1 - \cos \chi) \left(1 - \frac{1}{\langle N_c \rangle} \right), \end{aligned} \quad (2.12)$$

with k_B is the Boltzmann constant and T the absolute temperature, which is set in MPCD by employing a cell-level thermostat [49].

2.4.1 MPCD parameters

The typical MPCD parameters are, the cell size $a = \sigma$, serving as the unit of length, making the presence of two monomers in the collision cell very unlikely, the number of solvent particles per MPCD-collision cell is $\rho = 5$ and their mass is $m = 1$, serving as the unit of mass, energy $k_B T$, the timescale is defined as $\tau_{\text{mpcd}} = a \sqrt{m/k_B T}$, The remaining MPCD-parameters were set as follows: the time between collisions is $\Delta t_{\text{mpcd}} = 0.1 \tau$, the rotation angle is $\chi = 130^\circ$.

2.5 Hybrid Program - MD+MPCD

The coupling between the monomers of the SBC and the solvent particles is achieved during the collision step, in which the former are included as point particles in the evaluation of the center-of-mass velocity of each cell (Eq. 2.13) [50, 51], and their velocities are also randomly rotated. This interaction is strong enough to keep the monomers at the desired temperature, once a thermostat for the solvent particles has been introduced, which in the present case corresponds to a cell-level, Maxwell-Boltzmann scaling [49]. During the collision step mass, momentum and energy are conserved, leading to correlations among the particles and giving rise to hydrodynamic interactions.

$$\mathbf{v}_{\text{cm}} = \frac{1}{m N_c + M N_c^{(m)}} \left(m \sum_{i=1}^{N_c} \mathbf{v}_i + M \sum_{j=1}^{N_c^{(m)}} \mathbf{V}_j \right), \quad (2.13)$$

where $N_c^{(m)}$ is the number of monomers in the considered collision cell, \mathbf{V}_j is the monomer velocity and $M = \langle N_c \rangle m$ is the monomer mass.

2.5.1 Shear rate

Lees-Edwards boundary conditions were used to generate a shear velocity field $\mathbf{v}(y) = \dot{\gamma} y \hat{\mathbf{e}}_1$, characterized by the shear rate $\dot{\gamma}$, as schematically depicted in Fig.2.10.

As a dimensionless measure of the shear rate, we consider the Weissenberg number Wi , which is the product of the shear rate with the longest relaxation time of the polymer. For the latter, we take the longest Zimm relaxation time τ_Z of a polymer with N_{pol} monomers, which is given by the expression [47, 52]

$$\tau_Z = \frac{\eta_s}{k_B T} \sigma^3 N_{\text{pol}}^{3\nu}, \quad (2.14)$$

where η_s is the (MPCD) solvent viscosity and $\nu = 3/5$ is the Flory exponent for self-avoiding chains.

2 MODEL AND METHODS

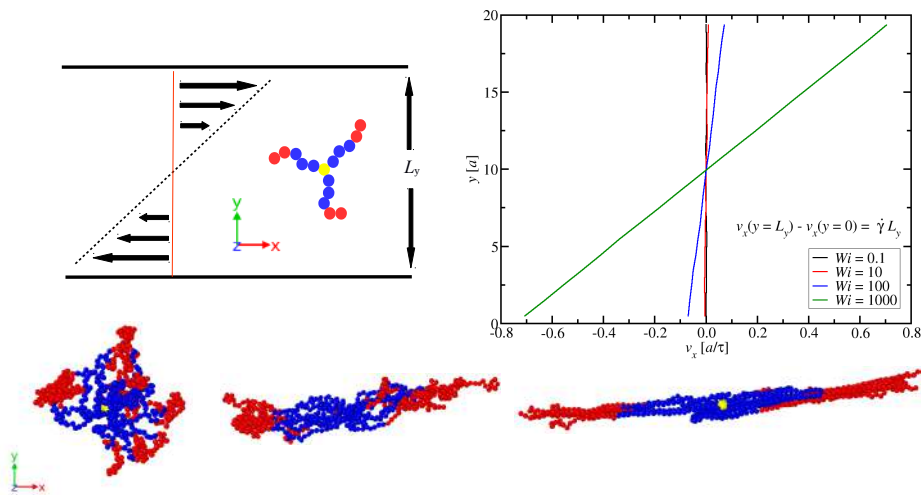


Figure 2.10. Top left: Schematic illustration of the simulation setup, demonstrating the shear ($\hat{x} = \hat{e}_1$), gradient ($\hat{y} = \hat{e}_2$), and vorticity ($\hat{z} = \hat{e}_3$) directions of planar, Couette flow. Top right: velocity profiles for the pure solvent obtained in our MPCD-simulation for different shear rates, corresponding to the Weissenberg numbers Wi of the polymer which are indicated in the legend. We emphasize that no polymer was dissolved in this case and the Wi is only used as a convenient way to characterize the flow strength. Bottom: Representative conformations of a SBC, viewed from the vorticity axis and projected on the xy -plane (flow-gradient-plane). Here, $f = 15$, $\alpha = 0.3$ and $\lambda = 1.1$. Snapshots are shown at equilibrium (left), intermediate ($Wi \approx 50$, middle) and high shear rates ($Wi \approx 10^3$, right). Yellow, red and blue spheres correspond respectively to the star core, solvophobic (B-type) monomers and solvophilic (A-type) monomers.

3 | Isolated SBC

*Star block-copolymers (SBCs) are macromolecules formed by several diblock copolymers anchored to a common central core, the internal monomers solvophilic and the end monomers solvophobic, SBCs have been demonstrated to constitute self-assembling building blocks with specific softness, functionalization, shape, and flexibility. Depending on different physical and chemical parameters the SBCs can behave as flexible patchy particles. In this chapter, we study the behavior of an SBC under shear flow using a hybrid mesoscale simulation technique. We systematically analyze the conformational properties of low-functionality stars, the formation of attractive patches on their corona as a function of the shear rate as well as the rotational dynamics. We cover a wide range of system parameters, including functionality, amphiphilicity, and solvent quality. It is shown that SBCs display a richer structural and dynamical behavior than athermal star polymers in the shear flow [RIPOLL, WINKLER and GOMPPER, Phys. Rev. Lett., (2006), **96**, 188302] and, therefore, they are also interesting candidates to tune the viscoelastic properties of complex fluids. We identify three factors of patch reorganization under shear that lead to patch numbers and orientations depending on shear rate, namely: free arms joining existing patches; a fusion of medium-sized patches into bigger ones; and fission of large patches into two smaller ones under high shear rates. In the final part of the chapter, we compare three different approaches to analyze the rotational dynamics: the laboratory frame, the non-inertial Eckart's frame, and a geometrical approximation relating the conformation of the SBC to the velocity profile of the solvent. We find that the geometrical approach is adequate when dealing with very soft systems while in the opposite extreme, the dynamics are best explained using the laboratory frame. On the other hand, the Eckart frame is found to be very general and to reproduced well both extreme cases. We also compare the rotational frequency and the kinetic energy with the definitions of the angular momentum and inertia tensor from recent publications. Since the conformation of single SBC is expected to be preserved in low-density bulk phases, the presented results are the first step in understanding and predicting rheological properties of semi-dilute suspensions of this kind of polymers.*

3.1 Introduction

Since SBCs can display both intramolecular and intermolecular association phenomena, a great deal of work has been devoted to the study of their conformational features in equilibrium, as well as the structure of their suspensions [23, 24, 53–56]. These studies have established that isolated SBCs behave as self-associating patchy particles (see Section 2.3.1), i.e., they self-assemble into structures with one or multiple aggregation sites or clusters of their solvophobic segments, whose number and extent can be tuned by different factors such as functionality (f), temperature, solvent quality and/or the fraction of solvophobic monomers. Furthermore, when several aggregation sites are present, these are distributed equally over the whole solid angle due to entropic effects and therefore SBCs resemble soft penetrable colloids with attractive patches, such patchiness being a robust property of the SBCs throughout a broad range of polymer concentrations [54].

The understanding of the role that the conformation and softness of polymer-based assemblies have on the rheological properties of their suspensions, on the other hand, is of considerable interest from both fundamental and applied perspectives [32, 57]. Extensive simulation studies have considered the behavior of isolated polymers of diverse architectures (linear, ring, star-like and hyper-branched) in shear flow, demonstrating particular features due to the conformational degrees of freedom, which distinguish them sharply from rigid colloidal particles [47, 58–64]. In the particular case of athermal star polymers, i.e., stars without solvophobic end groups, it has been shown that their structural flexibility leads to the mutual influence of fluid and polymer, resulting in both a change in the conformation of the star and a deviation from the mean velocity profile of the fluid. Also, stars with small functionality f exhibit a tumbling motion characterized by alternating collapsed and stretched conformations, resembling the behavior of linear polymers, while high-functionality stars perform a continuous tank-treading rotation similar to fluid droplets and capsules [47, 62]. Furthermore, telechelic, stiff linear polymers assemble in equilibrium into scaffold-like networks, whose properties are governed by polymer flexibility and end-attraction strength. Shear flow induces significant structural changes featuring three major rheological regimes, depending on the strength of the applied shear flow [65, 66].

The rest of this chapter is organized as follows: In Sec. 3.2 we defined the parameter for the SBC model. In Sec. 3.3, we show and discuss our findings for the geometric features, i.e. sizes and shapes, of SBCs under shear. In Sec. 3.4 We discuss the patch reorganization as a consequence of shear, In Sec. 3.5 we presented the analysis of the rotational dynamics in special the calculation of the rotational frequency. Finally, In Sec. 3.6 we summarize and draw our conclusions.

3.2 Model parameters

In the first part of the chapter, we investigate the structural properties of isolated, moderate-functionality ($12 \leq f \leq 18$) SBCs under the influence of homogeneous, linear shear flow using a hybrid simulation approach (see Section 2.5). We quantitatively analyze the behavior of shape and patchiness of an SBC at several amphiphilicities and solvent qualities. We span a range of Weissenberg numbers Wi from zero (equilibrium) to the order of 10^3 , the latter lying into the non-linear regime. We obtain $\tau_z \simeq 1.3 \times 10^4 \tau$ for the specific choices of the MPCD collision parameters (see Chapter 2, Section 2.4.1) and the value $N_{\text{pol}} = 40$ employed here.

In the second part of the chapter, we consider the rotational dynamics of isolated SBCs. We focus on the following three particular sets of parameters: $\{f, \alpha, \lambda\} = \{12, 0.3, 1.0\}$ (Case 1), $\{15, 0.5, 1.1\}$ (Case 2) and $\{18, 0.7, 1.1\}$ (Case 3). The dynamic behavior of single SBCs must be considered to gain some insights about the influence of these patch rearrangements on the rheology of dilute suspensions. Motivated by very recent work on the rotational dynamics of star polymers in shear flow [67, 68], this part of the chapter focuses on the dynamics of sheared SBCs analyzed using the so-called Eckart frame, which allows separating pure rotational and vibrational motions.

We performed 14 independent runs with different initial conditions for each set of parameters $\{f, \alpha, \lambda, Wi\}$ investigated. A preparation run of 5×10^6 MD steps was executed in first place, which was long enough for the SBC to reach its stationary state and then, a production cycle of 1.5×10^7 MD steps took place. Depending on the shear rate, the simulation box has dimensions $60\sigma \leq L_x \leq 110\sigma$ and $L_y = L_z = 60\sigma$. Data for shape parameters, patch number and patch sizes were evaluated every 2×10^4 MD steps and averaged during the production cycle.

3.3 Geometric properties

The global conformational features of the SCB at different shear rates are summarized in Figs. 3.1 and 3.2. In first place, the dependency on Wi of the radius of gyration (see Chapter 2, Section 2.3.1.a) (R_{gyr}) and of both the asphericity (δ) and the acylindricity (c) parameters are reported in Fig. 3.1. In general, SBCs feature a smaller spatial extension R_{gyr} than their athermal counterparts, the difference between the two growing for larger values of α and λ . The radius of gyration of all systems increases with shear rate, a feature due to the stronger stretching along the flow direction, which overcompensates for the concomitant shrinking in the gradient-and vorticity directions. Referring in particular to the inset of the upper panel of Fig. 3.1, we can distinguish, roughly, three regions in the dependence of the polymer size on Wi . For $Wi \lesssim 10$, the macromolecules essentially maintain their equilibrium sizes and conformations, whereas for $10 \lesssim Wi \lesssim 400$ shear has a profound influence on the shape and conformation of the stars, leading

3 ISOLATED SBC

to rearrangements of the attractive patches and changes of their number and orientation, as it will be shown in more detail in what follows. In this regime, the ratio r_{gyr} of the gyration radius of the SBCs to that of the athermal stars has a non-monotonic dependence on Wi , as shown in the inset of the upper panel of Fig. 3.1, a manifestation of the strong rearrangements of the SBC-arms. Finally, in the very strong shear regime, $Wi > 400$, the arms of the SBCs become strongly stretched and all stars tend to very similar, elongated conformations. In particular, the arms of all SBCs are forced to stretch and the gyration radius of all molecules approaches the same value as that of athermal stars.

On the other hand, the behaviour of the asphericity δ suggests that as the shear rate increases the SBC loses its spherical symmetry and develops a rod-like shape ($\delta \rightarrow 1$), whose associated acylindricity drops monotonically for $10 < Wi < 400$. As before δ and c tend to the same values of the athermal stars for high Wi , it being particularly notorious for the case $\alpha = 0.7$ and $\lambda = 1.1$, which displays a clearly different global shape with respect to the other SBCs for $Wi < 10$.

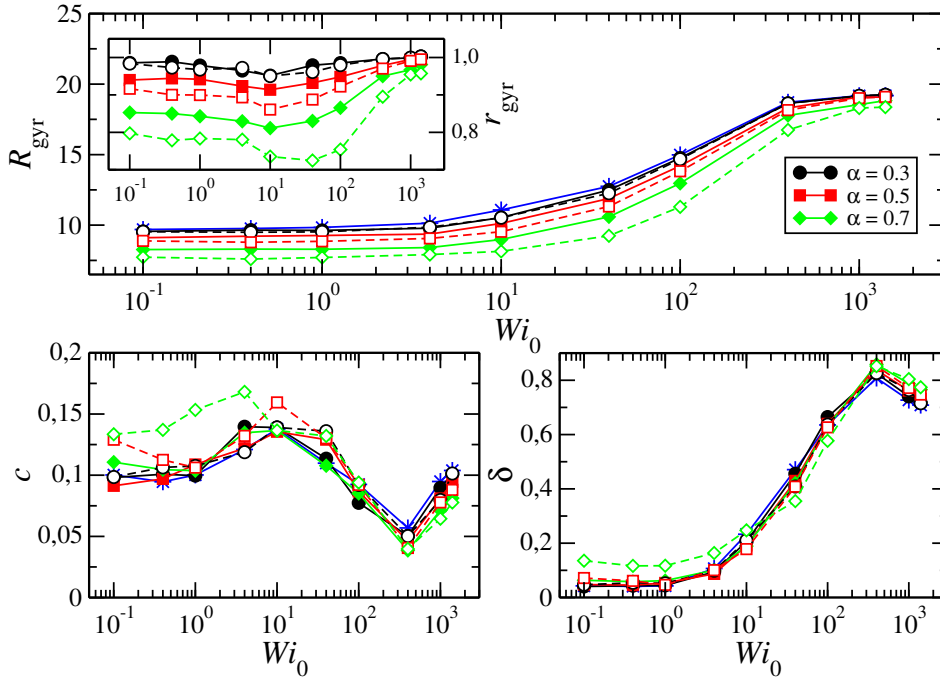


Figure 3.1. Average shape descriptors as a function of the Weissenberg number for $f = 15$ and polymerization degree $N_{\text{pol}} = 40$. Radius of gyration (top), asphericity (bottom-right) and acylindricity (bottom-left) are shown for $\lambda = 1.0$ (filled symbols) and $\lambda = 1.1$ (empty symbols). Blue stars indicate the data for pure repulsive stars ($\lambda = 0$ or $\alpha = 0$). Inset: Normalized radius of gyration $r_{\text{gyr}} = R_{\text{gyr}}/R_{\text{gyr}}^{(\text{ath})}$, where $R_{\text{gyr}}^{(\text{ath})}$ is the corresponding value for athermal stars at a given Wi .

An interesting feature in Fig. 3.1 is a ‘kink’ in the asphericity and in the acylindricity at the highest values of the Weissenberg number ($Wi > 400$), which is also found for the vorticity-component G_{zz} of the gyration tensor. This kink is caused by a combination of shear-induced

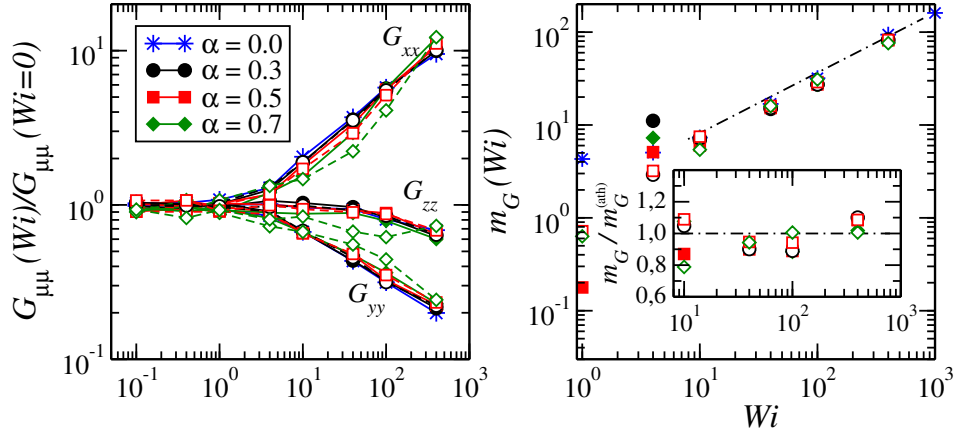


Figure 3.2. Diagonal components of the gyration tensor (left) and orientational resistance (right) at different shear rates for $f = 18$, $\lambda = 1.0$ (filled symbols) and $\lambda = 1.1$ (empty symbols). In the inset, data for m_G are normalized by a factor $m_G^{(\text{ath})} = 0.84 f^{0.27} Wi^{0.65}$, which corresponds to the scaling law (dash-dot lines) found for athermal stars at $Wi \gtrsim 10$ [47].

confinement of the stars, the strong steric interactions, and crowding at the star core, as well as the relatively short arm length, $N_{\text{pol}} = 40$. Characteristic snapshots Fig. 3.3. At low values of Wi the stars are hardly distorted, whereas for $Wi \gtrsim 10$ the molecules become increasingly anisotropic, expanding in the flow direction and shrinking most strongly in the shear direction and less so along the vorticity axis. Around the value $Wi \simeq 400$, the confinement in the gradient direction is so strong that the stars resemble two-dimensional objects [69]. Beyond this point, no further shrinkage along the vorticity direction is possible anymore, because the arms become strongly stretched and the steric hindrance close to the anchoring point in the center pushes these stretched, rod-like arms back out into the vorticity direction. In the employed model of the SBC, the anchoring points of arms to the core are allowed to freely glide along the core surface, i.e., the grafting points are not spatially fixed. As a consequence of this, for $Wi > 400$ an antagonistic effect appears between the shear-induced shrinkage and the strong monomer packing close to the core poles; as mentioned above, the crowding at the poles becomes so strong that arms start getting ejected sideways along the vorticity direction (see bottom panels of Fig. 3.3). This behavior is associated with the kink of shape-descriptors curves at a very high Wi . Since it does not reflect the general features of the SBC, we consider it no further. At this point, it is also worth to note that, at high Wi , loose arms rotate in the flow-vorticity plane in the course of the SBCs tank-treading-like motion, getting reattached to the extended arms at the two ends of the star while other ones leave those patches to perform further rotations.

The above considerations on the shape of the stars are quantified by the analysis of the diagonal components $G_{\mu\mu}(Wi)$ ($\mu = x, y, z$) of the gyration tensor as a function of Wi , shown in Fig. 3.2. There is a remarkable collapse of almost all curves for the reduced quantities (over their value

3 ISOLATED SBC

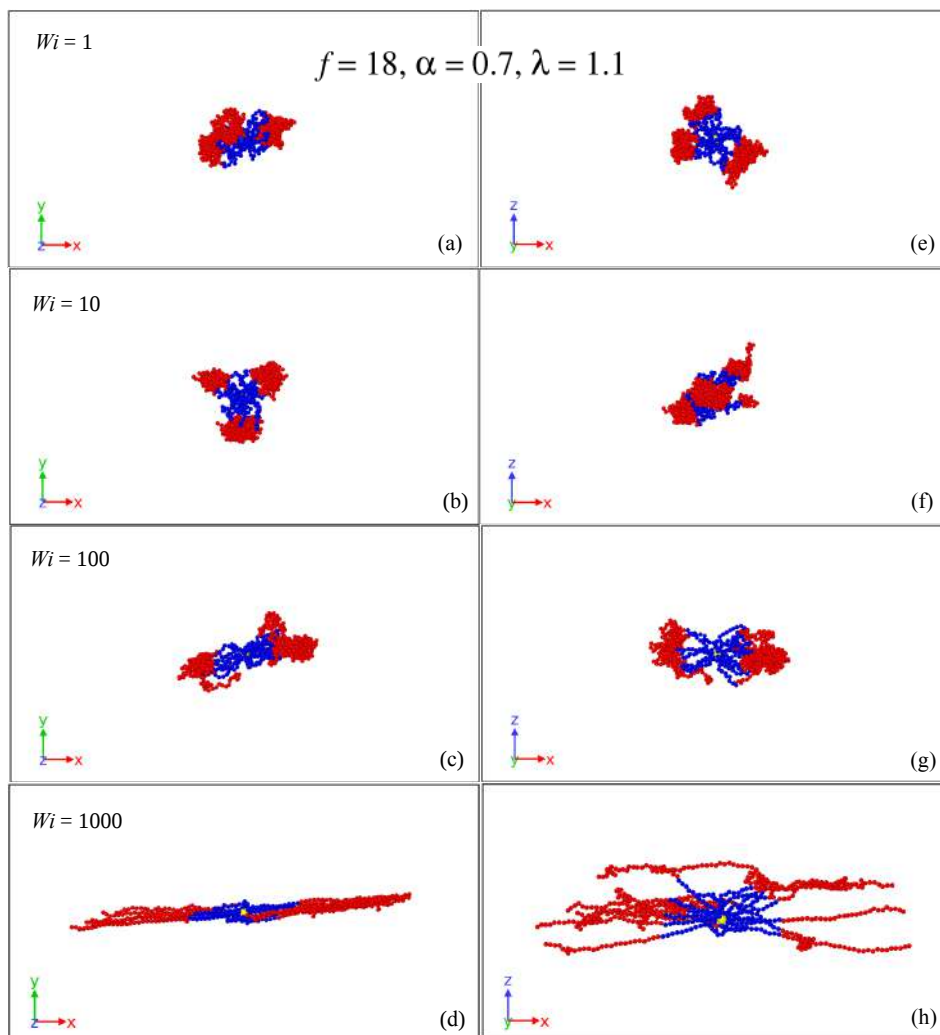


Figure 3.3. Typical simulation snapshots of the SBC with parameters $f = 18, \alpha = 0.7, \lambda = 1.1$ under shear at the Wi -values indicated on the legends. Panels (a)-(d) show the view from the vorticity axis on the flow-gradient plane at the given Weissenberg numbers, whereas for panels (e)-(h) the same snapshot as at the panel on the left is shown from the gradient axis looking onto the vorticity-flow plane. Solvophilic monomers are rendered as blue beads and solvophobic ones as red ones.

at equilibrium, $Wi = 0$), irrespective of the α - or λ -values; an exception is the extreme case $f = 18, \alpha = 0.7, \lambda = 1.1$, which forms three ‘bulky’ patches at equilibrium and thus does not deform under shear as strongly as the other molecules do. As a further global parameter to characterize the conformation of the SBC, we consider the orientational resistance m_G , which measures the average alignment of the polymer induced by the flow and is related to the angle χ_G formed between the eigenvector \hat{e}_1 (see Fig. 2.10) associated to the largest eigenvalue λ_1 and the flow (\mathbf{x}) direction.

3 ISOLATED SBC

This is defined in terms of components of the gyration tensor as [47],

$$\frac{m_G}{Wi} = \tan(2\chi_G) = \frac{2G_{xy}}{G_{xx} - G_{yy}}. \quad (3.1)$$

The right panel of Fig. 3.2 displays the orientational resistance of the SBCs, demonstrating a remarkable insensitivity to the details of the molecular architecture for a fixed functionality f . Neither the strength of the attraction nor the fraction of attractive monomers affect the orientational resistance, which in fact follows, for sufficiently high values of Wi , the same power law as athermal stars, $m_G^{(\text{ath})} \propto f^{0.27} Wi^{0.65}$. Though the individual values of the diagonal and the flow-gradient components of the gyration tensor differ among different SBCs, these differences cancel out once the ratio of Eq. (3.1) is formed and the orientational resistance becomes a universal quantity.

3.4 Patches behaviour

After grasping the characteristics of the global conformation of the stars, we now focus our attention on the features of the patches, i.e., the clusters formed by the solvophobic monomers of the outer block. In the good solvent limit, $\lambda \rightarrow 0$, as well as for low amphiphilicities $\alpha < 0.3$, no patches are formed in equilibrium [24, 54] for the values of λ considered here ($0.9 \leq \lambda \leq 1.1$). In such cases, the entropic intra-star repulsions dominate over the enthalpic attractions between the solvophobic tails and the stars behave in the same manner as athermal stars [70]. For $\alpha \geq 0.3$ patches form, whose number N_p and population S_p first increase as the attraction coupling constant λ does, whereas subsequently N_p decreases again as different patches start merging into bigger ones [23]. Since both athermal and amphiphilic star polymers elongate and take on a more prolate shape under linear shear conditions [47, 63], it is to expect that applying shear on SBC promotes clustering and leads to an increase in patch number and size compared to equilibrium conditions.

To characterize the behaviour of the formed patches under shear, we evaluate the distribution $P(N_p)$ of the number of clusters found per SBC, its average value $\langle N_p \rangle$ and the corresponding distribution $P(S_p)$ and average $\langle S_p \rangle$ for the patch population (size); the latter represents the number of arms bonded together in a given patch ($S_p \geq 2$). Patches are defined by a threshold-based clustering algorithm, in the same way as in [23], where two arms are defined to belong to the same cluster if at least two of their B-monomers (one in each arm) are connected neighbours, i.e., their distance is less than a threshold value of $r_{\text{cluster}} = 1.1\sigma$. The quantity,

$$F = f - \langle N_p \rangle \langle S_p \rangle, \quad (3.2)$$

is also introduced to express the typical number of free arms present (i.e., not belonging to any patch) in the configuration. We discuss the three generic types of behaviour emerging from our

3 ISOLATED SBC

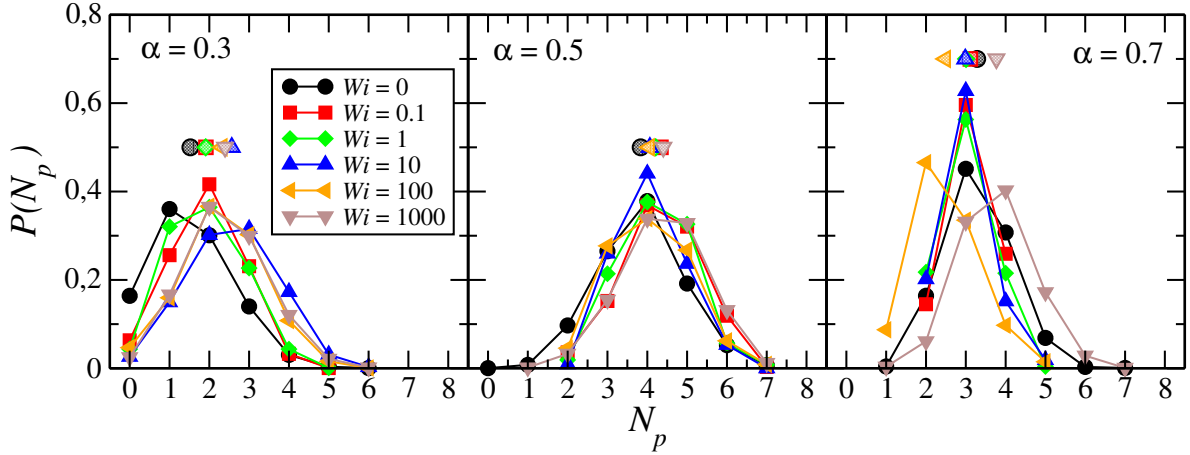


Figure 3.4. Distribution of number of patches for $f = 18$ and $\lambda = 1.1$. Symbols above the distributions indicate the corresponding average number of patches $\langle N_p \rangle$ per SBC.

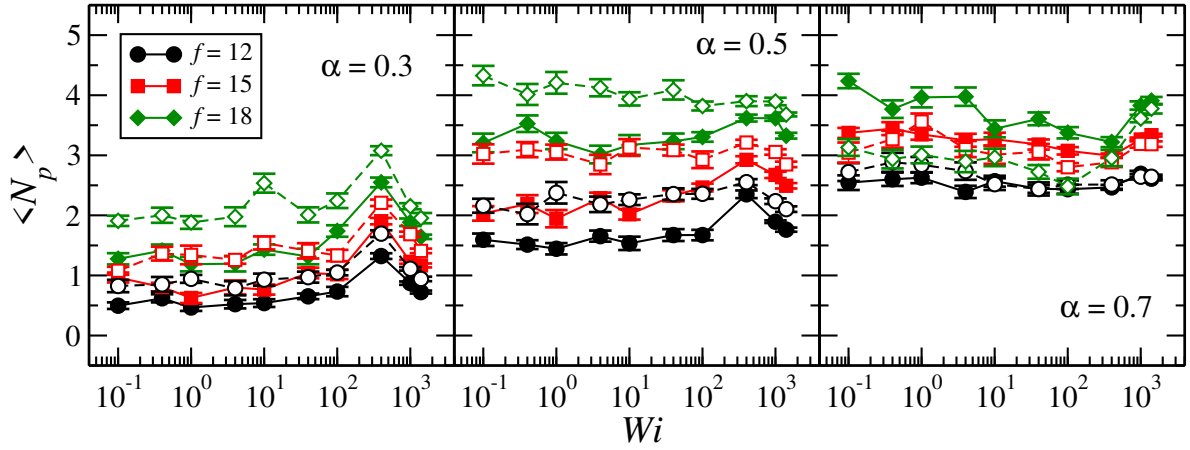


Figure 3.5. Average number of patches as a function of the Weissenberg number for SBC of different functionality ($N_{\text{pol}} = 40$) at $\lambda = 1.0$ (filled symbols) and $\lambda = 1.1$ (empty symbols).

numerical experiments and the underlying mechanisms of patch organization and rearrangements in what follows. In Fig. 3.4 we display the dependence of $P(N_p)$ on different shear rates for the case $f = 18$ and $\lambda = 1.1$ with three different values of the fraction of attractive monomers: $\alpha = 0.3, 0.5$ and 0.7 . The behaviour shown there is characteristic of all cases studied and then summarized in Fig. 3.5 for the expectation value $\langle N_p \rangle$, so that a discussion of its features covers all cases studied. At the same time, the information on the number of patches should be read in conjunction with the distribution $P(S_p)$ of the number of arms participating in the patch and the expectation value $\langle S_p \rangle$, shown in Figs. 3.6 and 3.7, respectively.

Let us start with the smallest fraction of attractive monomers, $\alpha = 0.3$. In this case, many arms are unattached to any patch at equilibrium and there is even a finite probability that there

3 ISOLATED SBC

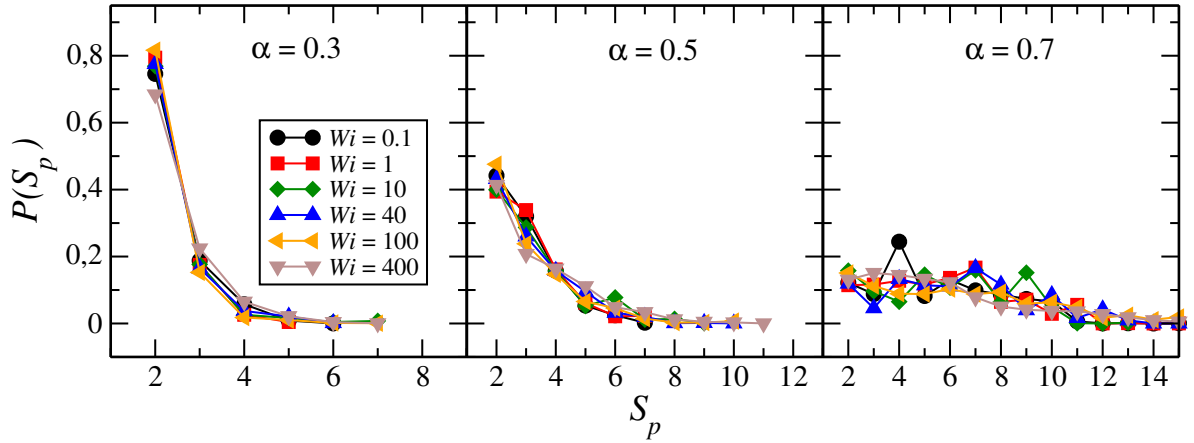


Figure 3.6. Distribution of patch population for $f = 18$, polymerization degree $N_{\text{pol}} = 40$, $\lambda = 1.1$. Symbols above the distributions indicate the corresponding average value $\langle S_p \rangle$.

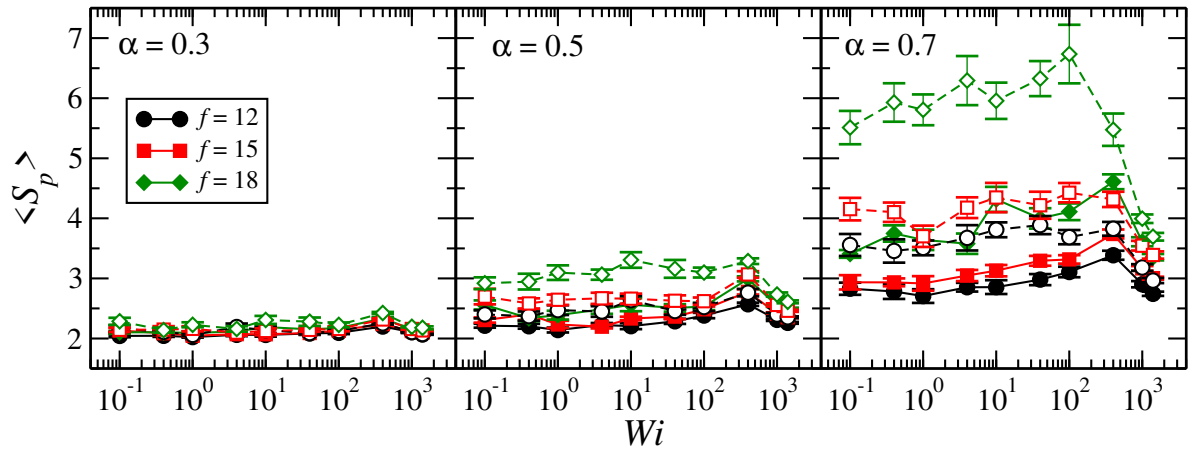


Figure 3.7. Average number of arms participating in patch formation as a function of the Weissenberg number for SBCs of different functionality ($N_{\text{pol}} = 40$) at $\lambda = 1.0$ (filled symbols) and $\lambda = 1.1$ (empty symbols).

exist zero patches, i.e., all arms are unattached, see Fig. 3.4. For such an initial situation, shear fields bring about a monotonic increase of both the number of patches N_p and the number of arms participating in the patch, S_p . Indeed, the distribution $P(N_p)$ of Fig. 3.5 moves to the right and the probability of finding no patches becomes strongly suppressed; similarly, the expectation value $\langle N_p \rangle$ grows with Wi , see Fig. 3.5, and it only drops at very high Wi due to the strong arm stretching mentioned before, which causes stars to swell in the vorticity direction, an effect strongly affected by the relatively small value of the polymerization degree $N_{\text{pol}} = 40$. The growth of the number of patches is accompanied by a growth also of the patch population, seen in Figs. 3.6 and 3.7. It follows that the effect of the shear for such SBCs for which many arms are free at equilibrium ($F \gg 1$), is to bring non-associated arms into new forming patches. Note, however, that even at the maxima of the $\langle N_p \rangle$ - and $\langle S_p \rangle$ -curves, the majority of arms for $\alpha = 0.3$ are still free. Accordingly,

3 ISOLATED SBC

it is expected that in a concentrated, sheared solution such SBCs will be able to form a variety of different intermolecular transient bonds involving rather weak ones between individual arms and much stronger ones between multi-arm patches.

The above scenario maintains its validity in part also for $\alpha = 0.5$. As can be seen in Fig. 3.5, also in this case the curves display a increasing trend, expressing the creation of new patches as the shear rate grows. At the same time, however, for $f = 15$ and $f = 18$ and for the strongest attraction, $\lambda = 1.1$, the expected number of patches $\langle N_p \rangle$ is remarkably insensitive to the shear rate at the values $\langle N_p \rangle \cong 3$ for $f = 15$ and $\langle N_p \rangle \cong 4$ for $f = 18$, respectively. The corresponding distribution $P(N_p)$, shown in Fig. 3.4, is also remarkably robust, whereas $\langle S_p \rangle$ shows a moderate growth with Wi Fig. 3.7. In both of these cases, there exist free arms at equilibrium but they are in the minority: $F \cong 6$ for $f = 15$ and $F \cong 5$ for $f = 18$ (see Fig. 3.8). Accordingly, the SBC at equilibrium consists of a small number of well-organized multi-arm patches and a few remaining free chains. The imposed shear has the effect of driving additional free chains onto the existing patches. In this way, the population of the patches is increased without change in the number of patches themselves.

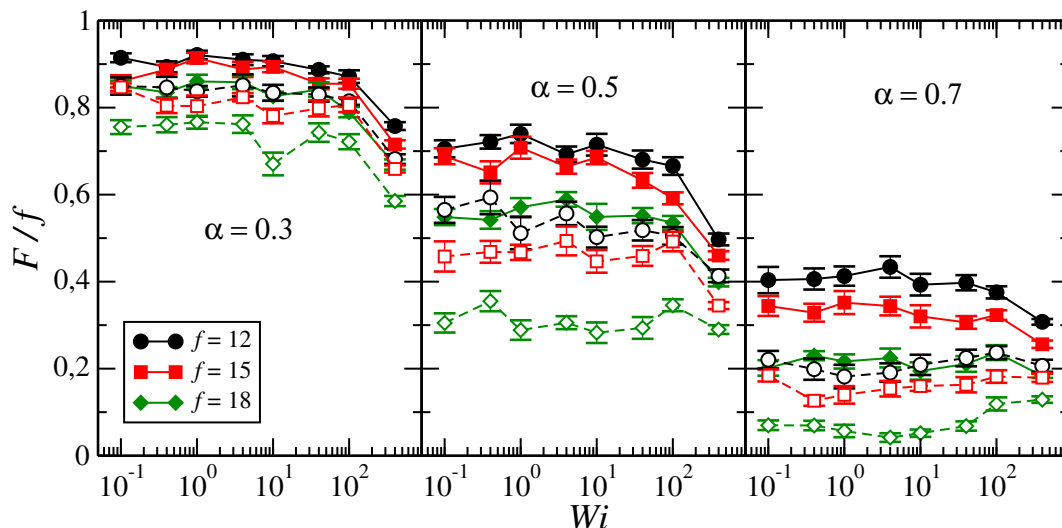


Figure 3.8. Typical fraction of free arms as a function of the Weissenberg number for SBCs of different functionality ($N_{\text{pol}} = 40$) at $\lambda = 1.0$ (filled symbols and continuous lines) and $\lambda = 1.1$ (empty symbols and dashed lines).

In this parameter domain, in which $F \lesssim f/2$ but there is still a considerable number of free chains, the SBCs act as robust patchy particles as far as the number of patches is concerned. However, the geometric arrangement of these patches with respect to one another is dramatically influenced by the imposed shear. To quantify this arrangement, we calculate the position of the center of mass for each patch and we draw vectors connecting the star core with those points. Subsequently, we measure the probability distribution function $P(\cos \theta)$ for the mutual angle θ between any pair of those vectors. Results are shown in Fig. 3.9 for the histograms and they

3 ISOLATED SBC

are visualized via characteristic simulation snapshots in Fig. 3.10 that follows. The number of patches is fluctuating around the average value $\langle N_p \rangle = 4$ for all values of Wi but the geometric arrangement of the patches changes markedly. At equilibrium, $Wi = 0$, the distribution of angles in Fig. 3.9 is rather broad due to the rather short length of the arms, with the well-defined tetrahedral distribution for the much longer arms of the SBCs seen in previous work at equilibrium [23]. Increasing the shear rate causes a gradual squeezing of the star towards the flow-vorticity plane and the patches assume a concomitant planar configuration with two of them pointing ‘forward’ and two of them ‘backward’, see Fig. 3.10 panels (c) and (g). At the highest value shown, $Wi = 10^3$, there are two pairs of patches on either side, bringing forward a bimodal distribution $P(\cos \theta)$ with two pronounced maxima at $\cos \theta = \pm 1$. At the same time, a few arms break free and they rotate on the flow-vorticity plane, see Fig. 3.10, panel (h).

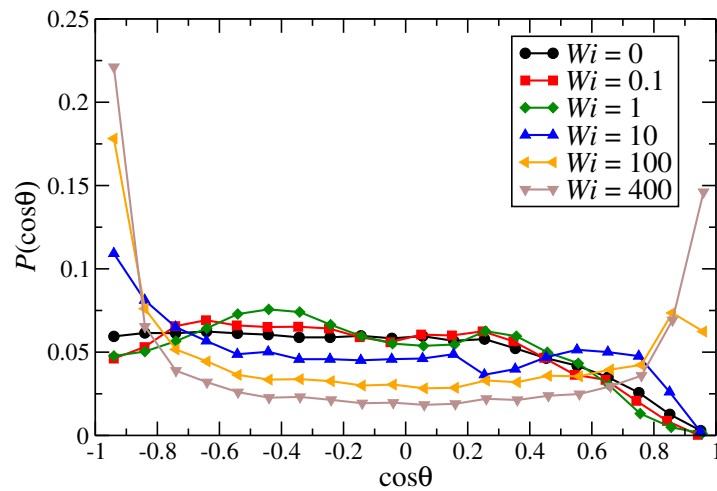


Figure 3.9. The distribution of the cosine of the angle θ between the vectors connecting the SBC-center with the centers of mass of the patches for the case $f = 18$, $\alpha = 0.5$, $\lambda = 1.1$ for different values of the Weissenberg number, as indicated by the legend.

A third pattern of behaviour of SBCs under shear is finally observed for the highest fraction of attractive monomers, $\alpha = 0.7$ seen at the bottom panels of Figs. 3.5 and 3.7. One encounters the already discussed scenario of $\langle N_p \rangle$ remaining unaffected by shear but, in addition to it, and for the cases $f = 18$, $\lambda = 1.0$ and $f = 18$, $\lambda = 1.1$, a new scenario shows up. Here, the average number of patches $\langle N_p \rangle$ first decreases with increasing Wi accompanied by a simultaneous increase in $\langle S_p \rangle$, see the empty- and filled-diamonds Figs. 3.5 and 3.7. At very high shear rates, the trend reverses itself: the number of patches increases and their population becomes smaller. It can be easily seen that this is happening for the cases in which there are hardly any free arms for the SBC at equilibrium: $F \ll f$. All of the linear chains are organized in patches of 3 or 4 members and the attractions are too strong for the patches to be destroyed under moderate or even high shear. Accordingly, the effect of the external drive is to drive the *fusion* of existing, big patches into new,

3 ISOLATED SBC

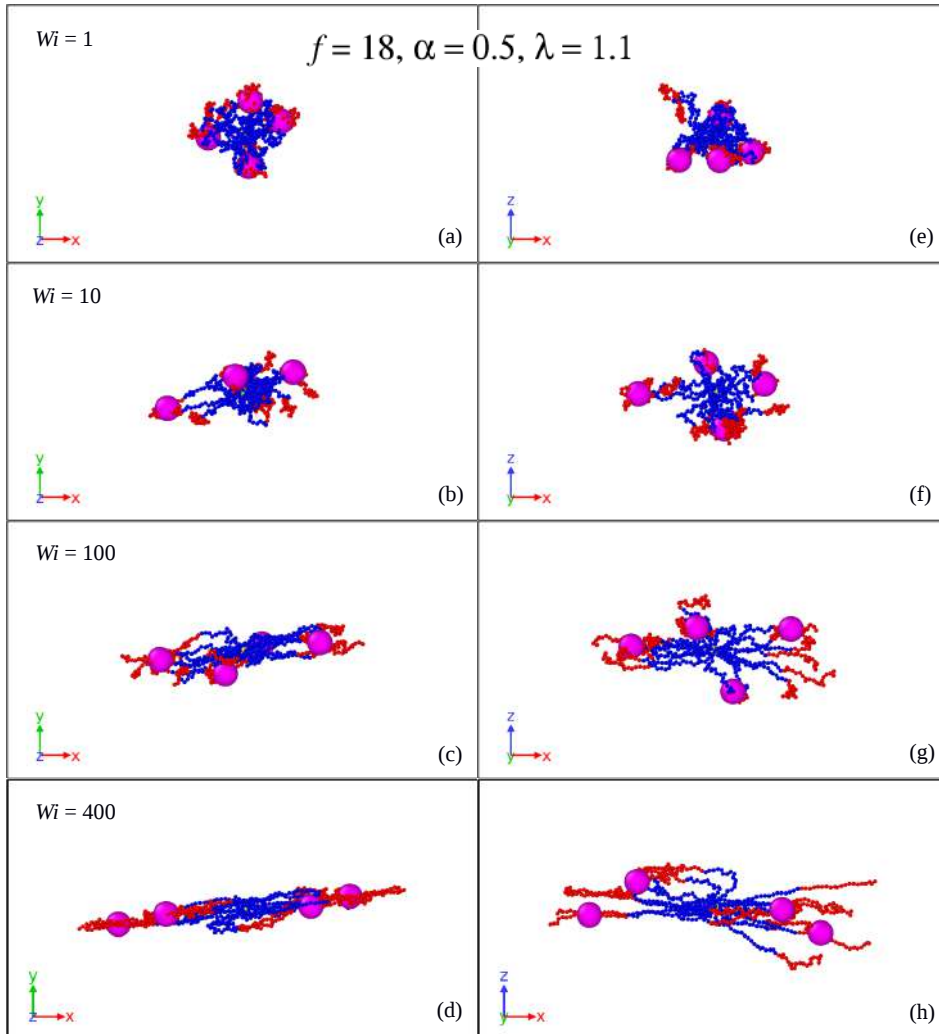


Figure 3.10. Characteristic simulation snapshots of the SCB ($f = 18, \alpha = 0.5, \lambda = 1.1$) under shear at increasing Weissenberg numbers as indicated on the panels. The left column displays the conformations on the flow-gradient plane, seen from the vorticity axis, whereas the right column on the flow-vorticity plane, seen from the gradient axis. Solvophilic and solvophobic monomers are rendered as blue and red beads, respectively. The larger magenta-colored spheres are centered at the centers of mass of the patches built by the end-groups.

bigger ones, thus decreasing their number and increasing their population. However, these patches are now too bulky, so that at very high shear rates, $Wi \gtrsim 500$, the shear is capable of breaking them up. It is now *fission* of big patches that reverses the trend and makes $\langle N_p \rangle$ go up and $\langle S_p \rangle$ go down. In all cases, the number of free arms is very low and $F \ll f$ holds. As already mentioned, the whole patch rearrangement scenario is accompanied by interesting dynamical aspects such as tumbling and arm rotation. These topics deserve careful analysis on their own and would be presented in a detailed way in the future, specially in the light of a very recent study suggesting the need to separate different relaxation (rotation, oscillation and breathing) modes to describe

the dynamics of athermal star polymers under shear [67, 68].

3.5 Rotational frequency

Soft colloids and polymers under shear flow deform and undergo a succession of complex motion patterns, such as tumbling and tank-treading, which are hard to decouple from one another and analyse quantitatively. Recent studies aimed to a better understanding of the complex dynamics of (athermal) star polymers in shear flow, have demonstrated that Eckart’s formalism allows to separate correctly the different characteristic motions of the polymer, i.e., pure rotation, vibration with no-angular momentum and vibrational angular momentum [67, 68]. In the following, a brief description of this formalism is given, which will be subsequently employed to analyse our simulation results. We use in what follows a number of abbreviations, whose meaning is summarized in Table 3.1 below.

Table 3.1. List of shorthands and abbreviations for systems and methods used.

Abbreviation	Meaning
Case 1	$\{f, \alpha, \lambda\} = \{12, 0.3, 1.0\}$
Case 2	$\{f, \alpha, \lambda\} = \{15, 0.5, 1.1\}$
Case 3	$\{f, \alpha, \lambda\} = \{18, 0.7, 1.1\}$
LF	Laboratory frame
EF	Eckart frame
HF	Hybrid frame
GA	Geometric approximation

According to our previous results (Sec. 3.4), the Cases represent the typical trends found in regard to the patchiness of the SBCs, namely, no patches are formed (Case 1), several patches are formed having a small population (Case 2), and few (one or two) bulky patches are formed (Case 3).

3.5.1 Laboratory frame (LF)

Here, the frame of reference is fixed in space and it is customarily and conveniently chosen in such a way that the first axis lies along the flow direction, the second along the gradient direction and the third along the vorticity direction, as shown in Figure 2.10. Taking \mathbf{r}_k and $\dot{\mathbf{r}}_k$ as the position and the velocity of the k -th monomer in the laboratory frame of reference, the total

3 ISOLATED SBC

angular momentum of a star polymer with respect to its center of mass is, by definition

$$\mathbf{L} = M \sum_{k=1}^{N_{\text{mon}}} \Delta \mathbf{r}_k \times \Delta \dot{\mathbf{r}}_k, \quad (3.3)$$

with $k = 1, \dots, N_{\text{mon}} = f N_{\text{pol}} + 1$, N_{mon} the total number of monomers, $\Delta \mathbf{r}_k = \mathbf{r}_k - \mathbf{r}_{\text{cm}}$ and $\Delta \dot{\mathbf{r}}_k = \dot{\mathbf{r}}_k - \dot{\mathbf{r}}_{\text{cm}}$. Here \mathbf{r}_{cm} and $\dot{\mathbf{r}}_{\text{cm}}$ are, respectively, the position and the velocity of the center of mass, i.e.,

$$\mathbf{r}_{\text{cm}} = \frac{1}{N_{\text{mon}}} \sum_{k=1}^{N_{\text{mon}}} \mathbf{r}_k. \quad (3.4)$$

The time evolution of the k -th monomer position can be evaluated as [67, 68, 71, 72],

$$\dot{\mathbf{r}}_k = \dot{\mathbf{r}}_{\text{cm}} + (\boldsymbol{\omega} \times \Delta \mathbf{r}_k) + \tilde{\mathbf{v}}_k, \quad (3.5)$$

where $\tilde{\mathbf{v}}_k$ denotes a purely vibrational motion which is angular momentum-free in the laboratory frame, i.e., $\tilde{\mathbf{v}}_k$ and $\Delta \mathbf{r}_k$ are parallel [cf. Eq. (3.3)]. The angular frequency $\boldsymbol{\omega}$ can be expressed as

$$\boldsymbol{\omega} = \mathbf{J}^{-1} \mathbf{L}, \quad (3.6)$$

with the components of the moment of inertia tensor \mathbf{J} being defined as

$$J_{\mu\nu} = M \sum_{k=1}^{N_{\text{mon}}} [\Delta r_k^2 \delta_{\mu\nu} - \Delta r_{k,\mu} \Delta r_{k,\nu}] \quad (\mu, \nu = 1, 2, 3), \quad (3.7)$$

with $\delta_{\mu\nu}$ the Kronecker delta and $r_{k,\mu}$ the μ -th component of position vector of the k -th monomer. In the case of rigid-body motion, $\tilde{\mathbf{v}} = 0$ and $\boldsymbol{\omega}$ coincides with the rotational angular velocity. The full kinetic energy E_{kin} of the sheared polymer results from Eq. (3.5) and reads as

$$E_{\text{kin}} = \frac{1}{2} M \sum_k \dot{\mathbf{r}}_k \cdot \dot{\mathbf{r}}_k = \frac{1}{2} M_s \dot{\mathbf{r}}_{\text{cm}} \cdot \dot{\mathbf{r}}_{\text{cm}} + \frac{1}{2} \boldsymbol{\omega} \cdot \mathbf{J} \cdot \boldsymbol{\omega} + \frac{1}{2} M \sum_k \tilde{\mathbf{v}}_k \cdot \tilde{\mathbf{v}}_k, \quad (3.8)$$

where $M_s = N_{\text{mon}} M$ is the total mass of the polymer. The three terms at the r.h.s of Eq. (3.8) represent the translational, rotational, and vibrational contributions to the kinetic energy, respectively. We emphasize, though, that the velocity contribution $\tilde{\mathbf{v}}_k$ in the motion of a monomer is not the only vibrational contribution but just the one that does not contribute to the (instantaneous) angular momentum; there are, in general, additional vibrational contributions included in $\boldsymbol{\omega}$. Therefore, $\boldsymbol{\omega}$ is the apparent angular velocity and it is not possible to separate rotation from vibrational with angular momentum motion within the lab frame.

3.5.2 Eckart frame (EF)

The Eckart's formalism makes use of a non-inertial frame which co-rotates with the polymer at angular velocity Ω (see Eq. (3.14) below) [73, 74]. The first step to built up the Eckart frame is to choose one initial configuration of the SBC as reference, accompanied by an initial frame of reference spanned by the basis vectors $\{\mathbf{f}_1(0), \mathbf{f}_2(0), \mathbf{f}_3(0)\}$. The origin of this frame is located at the center of mass of the chosen reference configuration of the polymer and, as a matter of convenience, the three axes $\{\mathbf{f}_1(0), \mathbf{f}_2(0), \mathbf{f}_3(0)\}$ also coincide with the orientation of the laboratory frame. Due to the choice of the origin, in this system of coordinates the position vectors of the monomers at time $t = 0$, $\{\mathbf{a}_k = \Delta\mathbf{r}_k(0); k = 1, 2, \dots, N_{\text{mon}}\}$, satisfy the relation

$$\sum_{k=1}^{N_{\text{mon}}} \mathbf{a}_k = \mathbf{0}. \quad (3.9)$$

This reference configuration is frozen and co-rotates with the Eckard frame of reference, the latter evolving with time as explained below. In the second step of the process, the unit base (column) vectors $\{\mathbf{f}_1(t), \mathbf{f}_2(t), \mathbf{f}_3(t)\}$ of the instantaneous Eckart frame are evaluated. To achieve that, the vectors

$$\mathcal{F}_\mu(t) = M \sum_k a_{k,\mu} \Delta\mathbf{r}_k(t) \quad (\mu = 1, 2, 3), \quad (3.10)$$

are introduced, which are completely defined in terms of the instantaneous positions $\Delta\mathbf{r}_k(t)$ and the Cartesian components $a_{k,\mu}$ of the reference position vectors \mathbf{a}_k for each monomer. In what follows, we drop the explicit time-dependence from the notation of the various vectors. The right-handed triad of unit vectors $\{\mathbf{f}_1, \mathbf{f}_2, \mathbf{f}_3\}$ is determined as

$$[\mathbf{f}_1, \mathbf{f}_2, \mathbf{f}_3] = [\mathcal{F}_1, \mathcal{F}_2, \mathcal{F}_3] \mathbb{F}^{-1/2}, \quad (3.11)$$

where the elements of the symmetric (Gram) matrix \mathbb{F} are defined as $[\mathbb{F}]_{\mu\nu} = \mathcal{F}_\mu \cdot \mathcal{F}_\nu$ and $\mathbb{F}^{-1/2} \mathbb{F}^{-1/2} = \mathbb{F}^{-1}$. In this way, the position vector \mathbf{c}_k of the k -th monomer in the co-rotating reference configuration, decomposed onto the unit vectors of the rotating Eckart frame of reference, is given by

$$\mathbf{c}_k = \sum_{\mu=1}^3 a_{k,\mu} \mathbf{f}_\mu, \quad (3.12)$$

the coefficients $a_{k,\mu}$ being fixed, time-independent quantities set by the reference configuration, and the triad $\{\mathbf{f}_1, \mathbf{f}_2, \mathbf{f}_3\}$ depending on time as explained above. In this way, the \mathbf{c}_k are *constant* vectors when looked upon from within the rotating Eckart frame and describe the original, rigid configuration.

3 ISOLATED SBC

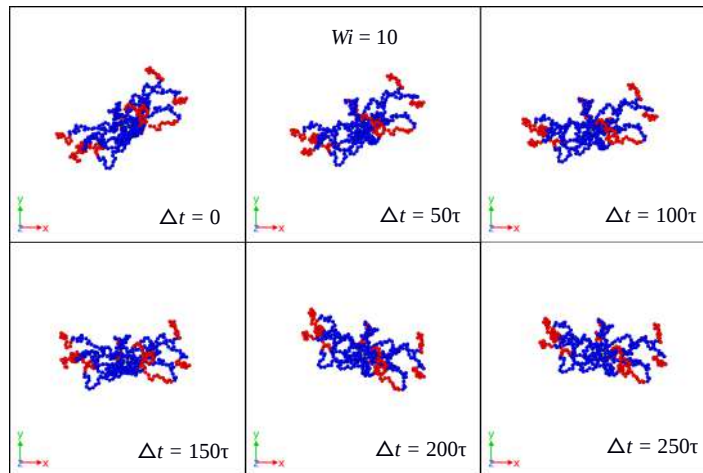


Figure 3.11. Time evolution of the (fixed) reference configuration in the Eckart's frame as seen in the laboratory frame for Case 1 and $Wi = 10$.

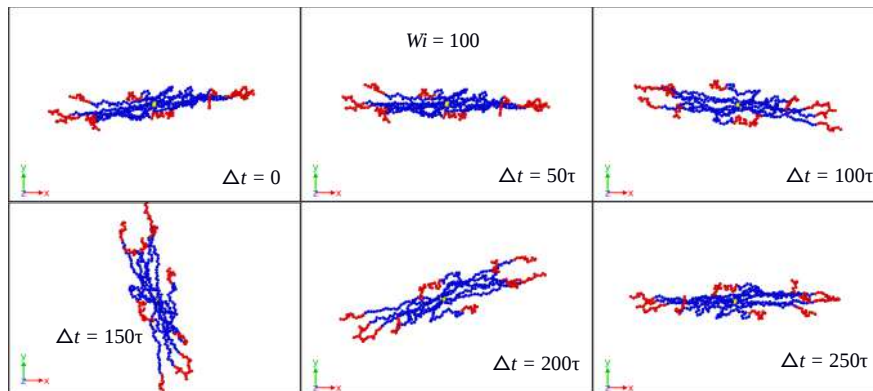


Figure 3.12. Time evolution of the (fixed) reference configuration in the Eckart's frame as seen in the laboratory frame for Case 1 and $Wi = 100$.

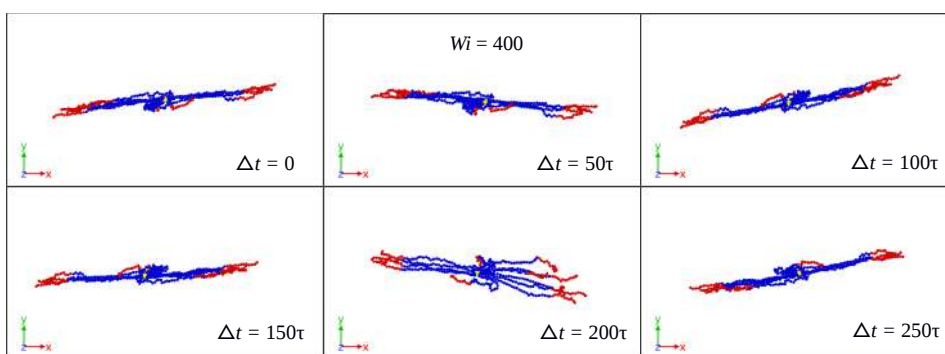


Figure 3.13. Time evolution of the (fixed) reference configuration in the Eckart's frame as seen in the laboratory frame for Case 1 and $Wi = 400$.

3 ISOLATED SBC

Using the initial configuration of the SBC in the production run as the (fixed) reference configuration for the Eckart's frame, Figs. 3.11–3.13 show its time evolution as it is seen in the laboratory frame for Case 1 and different shear rates. For $Wi = 10$, the reference configuration is seen in the lab frame as a rigid body rotating mainly around the vorticity axes. As the shear rate increases, the rotation takes place faster and around all three axes in lab frame, as illustrated by the cases $Wi = 100$ and $Wi = 400$. For the latter, Fig. 3.12 and 3.13 show a significant change of the Eckart frame orientation with respect to the lab frame. The polymer is expected to have a relatively high rotation frequency around the vorticity axis in the lab frame, which is found in the Eckart frame as well (see Appendix 3A).

The angular velocity $\boldsymbol{\Omega}$ of the Eckart coordinate system can be determined by starting from the time derivative of the Eckart condition [68, 71, 72],

$$M \sum_k \mathbf{c}_k \times \boldsymbol{\rho}_k = \mathbf{0}. \quad (3.13)$$

Taking into account that the unit vectors of the Eckart frame evolve in time like rotations of a rigid body, $\dot{\mathbf{f}}_\mu = \boldsymbol{\Omega} \times \mathbf{f}_\mu$, ($\mu = 1, 2, 3$), the Eckart angular velocity $\boldsymbol{\Omega}$ is expressed as:

$$\boldsymbol{\Omega} = \mathbf{J}'^{-1} \mathbf{L}', \quad (3.14)$$

where the 'inertia tensor' \mathbf{J}' and the 'angular momentum vector' \mathbf{L}' are given by the relations:

$$\mathbf{J}' = M \sum_k [(\Delta \mathbf{r}_k \cdot \mathbf{c}_k) \mathbf{I} - \Delta \mathbf{r}_k \otimes \mathbf{c}_k] \quad (3.15)$$

and

$$\mathbf{L}' = M \sum_k \mathbf{c}_k \times \Delta \dot{\mathbf{r}}_k. \quad (3.16)$$

The above equations provide an expression for the (instantaneous) angular velocity $\boldsymbol{\Omega}$ of rotation of the Eckart frame. Note that in the case of a truly rigid body, $\Delta \mathbf{r}_k = \mathbf{c}_k$ at all times and thus \mathbf{J}' and \mathbf{L}' become a true inertia tensor and angular momentum vector, respectively. In this frame, the kinetic energy of the polymer can be written as (see Appendix 3B):

$$E_{\text{kin}} = \frac{1}{2} M_s \dot{\mathbf{r}}_{\text{cm}} \cdot \dot{\mathbf{r}}_{\text{cm}} + \frac{1}{2} \boldsymbol{\Omega} \cdot \hat{\mathbf{J}} \cdot \boldsymbol{\Omega} + \frac{1}{2} M \sum_k \tilde{\mathbf{v}}_k \cdot \tilde{\mathbf{v}}_k + \frac{1}{2} M \sum_k \mathbf{u}_k \cdot \mathbf{u}_k + M \sum_k (\boldsymbol{\Omega} \times \mathbf{c}_k) \cdot \mathbf{u}_k, \quad (3.17)$$

where $\hat{\mathbf{J}}$ is the inertia tensor using the Eckart variables (see Eq. (3.19) below) and \mathbf{u}_k represents the angular contribution of the vibrational motion, i.e., the part of k -th monomer vibrational motion coupled with rotations if the angular velocity is calculated by the (lab frame) standard approach.

3 ISOLATED SBC

The last four terms of Eq. (3.17) represent the kinetic energy contributions from, respectively, pure rotation, vibrations without angular momentum, vibrations with angular momentum, and the Coriolis coupling (see Table 3.2). As can be seen, application of the Eckart frame formalism allows to distinguish between vibrations without and with angular momentum contribution, the latter being displacements with respect to the pure rotation of the reference configuration [68].

Table 3.2. The various contributions to the total kinetic energy in the laboratory, the Eckart frames and hybrid frame.

	Rotational	Vibrational without angular momentum	T_u =Vibrational with angular momentum + Coriolis coupling
LF	$\frac{1}{2} \boldsymbol{\omega} \cdot \mathbf{J} \cdot \boldsymbol{\omega}$	$\frac{M}{2} \sum_k \tilde{\mathbf{v}}_k \cdot \tilde{\mathbf{v}}_k$	–
EF	$\frac{1}{2} \boldsymbol{\Omega} \cdot \hat{\mathbf{J}} \cdot \boldsymbol{\Omega}$	$\frac{M}{2} \sum_k \tilde{\mathbf{v}}_k \cdot \tilde{\mathbf{v}}_k$	$\frac{M}{2} \sum_k \mathbf{u}_k \cdot \mathbf{u}_k + M \sum_k (\boldsymbol{\Omega} \times \mathbf{c}_k) \cdot \mathbf{u}_k$
HF	$\frac{1}{2} \mathbf{W} \cdot \hat{\mathbf{J}} \cdot \mathbf{W}$	$\frac{M}{2} \sum_k \tilde{\mathbf{v}}_k \cdot \tilde{\mathbf{v}}_k$	–

3.5.3 Hybrid frame (HF)

As mentioned before, the introduction of the Eckart frame allows to obtain an optimal separation of rotation and vibration. This feature has been employed in the formulation of symplectic integrators for MD simulations, which are applicable to molecules having one equilibrium configuration and which allows the evaluation of internal high-frequency vibrations [75–78]. Nevertheless its success to describe the vibrational dynamics of small molecules, it is interesting to note that the definition of the inertia tensor for the Eckart’s frame derived from the Eckart condition and given by Eq. (3.15) does not meet in general the symmetry condition, i.e.,

$$\Delta r_{k,\mu} c_{k,\nu} \neq \Delta r_{k,\nu} c_{k,\mu}. \quad (3.18)$$

To fulfil this last condition, we further explored a hybrid frame, in which we combine a proper, rigid-body inertia tensor $\hat{\mathbf{J}}$ [73, 74] with the deformable-body angular momentum \mathbf{L} resolved on its Eckart-frame components, to define a new angular velocity \mathbf{W} . In particular, we define:

$$\hat{J}_{\mu\nu} = M \sum_k [c_k^2 \delta_{\mu\nu} - c_{k,\mu} c_{k,\nu}], \quad (3.19)$$

and the angular momentum (performing a transformation between the laboratory and the

3 ISOLATED SBC

Eckart's frames [74]),

$$\hat{\mathbf{L}} = \sum_{\mu=1}^3 (\mathbf{L} \cdot \mathbf{f}_{\mu}) \mathbf{f}_{\mu}. \quad (3.20)$$

The angular velocity of the hybrid system is then given by the expression:

$$\mathbf{W} = \hat{\mathbf{J}}^{-1} \hat{\mathbf{L}}. \quad (3.21)$$

In analogy with the expressions in the laboratory- and Eckart frames, we also consider here a rotational kinetic energy

$$E_{\text{rot}} = \frac{1}{2} \mathbf{W} \cdot \hat{\mathbf{J}} \cdot \mathbf{W}. \quad (3.22)$$

3.5.4 Geometrical approach (GA)

A last, complementary approach to estimate the rotational frequency of soft colloids under shear is the so-called geometrical approximation (GA). This is based on two assumptions about the behavior of the polymers in linear shear flow [79, 80]. First, it is assumed that the velocity of the monomers is entirely defined by the local, undisturbed velocity profile of the flow according to

$$\Delta \dot{\mathbf{r}}_k \simeq \dot{\gamma} \Delta r_{k,y} \hat{\mathbf{e}}_1. \quad (3.23)$$

Under this assumption the instantaneous angular momentum of the polymer is given by the expression

$$\mathbf{L} = M \sum_k \Delta \mathbf{r}_k \times \Delta \dot{\mathbf{r}}_k \simeq M_s \dot{\gamma} (G_{23} \hat{\mathbf{e}}_2 - G_{22} \hat{\mathbf{e}}_3), \quad (3.24)$$

where $G_{\mu\nu} = N_{\text{mon}}^{-1} \sum_k \Delta \mathbf{r}_{k,\mu} \Delta \mathbf{r}_{k,\nu}$ denotes the $\mu\nu$ -component of the gyration tensor, which measures the overall conformation of the SBC. Furthermore, a long-time average is then performed in Eq. (3.24), whereupon the non-diagonal element of the gyration tensor disappears and thus the average angular momentum has a single component, along the vorticity axis. Finally, it is assumed that the rotation of the SBC takes place mainly around the vorticity axis $\hat{\mathbf{e}}_3$, i.e., $\omega_1 = \omega_2 \approx 0$. Within these approximations $\omega_3 = \omega_G$ has a constant value and using Eq. (3.6) it results into

$$\omega_G \simeq -M_s \dot{\gamma} \frac{G_{22}}{J_{33}} = -\dot{\gamma} \frac{G_{22}}{G_{11} + G_{22}}. \quad (3.25)$$

Though clear by the construction of the GA, it is worth emphasizing once again that the so-obtained estimate for the angular frequency is a result of *averaging the polymer motion* over very

3 ISOLATED SBC

long time intervals while at the same time making the a priori assumption that the instantaneous velocities of the monomers only have a component along the shear direction, dictated by the undistorted solvent velocity profile, see Eq. (3.23). The final result, Eq. (3.25), corresponds to the tumbling (rotation) frequency of a rigid body whose shape is similar to the average shape of the SBC and which also have an angular momentum equal to the value given by the mean flow [67, 68]. At the same time, however, due to Eq. (3.23), the estimate ω_G is also valid for a tank-treading (TT)-type of motion, in which the SBC does not rotate as a whole but rather the individual arms rotate by tank-treading around the geometrical star center, which remains at rest. This is a different, prototypical type of motion, for which the overall shape of the star remains fixed in time, i.e., no tumbling of the soft colloid as a whole takes place.

3.5.5 Global conformation and dynamics

The overall (equilibrium) shape of a SBC depends on the number of patches formed and the compactness of the latter, which in turns depends on f , N_{pol} , α , and λ . Depending on the values of these parameters, three general cases can be recognized. At low α and λ ($\alpha < 0.3$ and $\lambda < 1.0$) the star block copolymers behave very similar to athermal stars ($\alpha = 0$) with no formation of patches or very weak, breakable ones (Case 1). On the other opposite limit, at high α and λ ($\alpha \gtrsim 0.6$ and $\lambda \gtrsim 1.1$), the macromolecule acquires cylindrical symmetry around its principal axis, since it self-assembles into dumbbell-like structures with one or two massive patches (Case 3). At intermediate values of α and λ , the SBCs form a number of patches that can break-up and/or merge as a consequence of shear (Case 2) [23, 54]. These three tendencies can be also observed from the dynamical point of view, as displayed in Fig. 3.14, where characteristic snapshots are shown, helping to visualize the time evolution of the SBCs under shear. As can be seen there, for low amphiphilicity and good solvent, the SBC behaves in a similar way as athermal stars and then the arms perform tank-treading-like (TT) motions. As the contribution of the attractive interaction increases, patches begin to form and TT rotation is also found, but this time the motion is simultaneously performed by all arms forming the cluster. Finally for high α and λ , the SBC motion closely resembles that of a rigid dumbbell. We will explore, in what follows, the ways in which these statements based on impressions from simulation snapshots acquire quantitative character through the comparison of characteristic quantities among different reference frames and approximations.

3.5.6 Reference configuration update

In the original Eckart formalism, the rigid reference configuration of (small) molecules is assumed to be the equilibrium one (all forces on all monomers vanishing) and its dynamics is governed by the time evolution of the positions of the atoms forming the molecule, which are

3 ISOLATED SBC

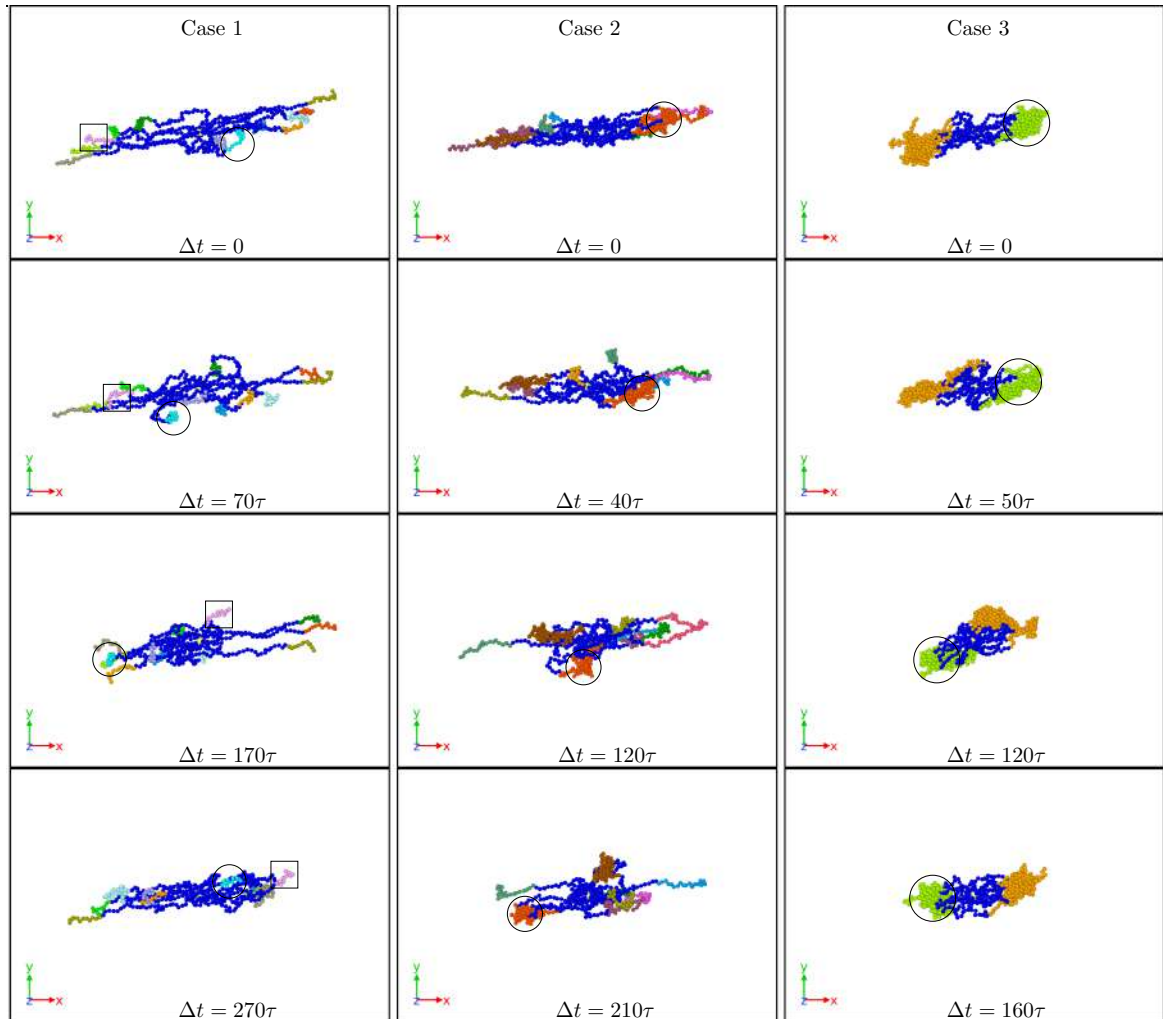


Figure 3.14. Representative simulation snapshots displaying the time evolution of the SBC in shear flow for $\{f, \alpha, \lambda\} = \{12, 0.3, 1.0\}$ (Case 1), $\{15, 0.5, 1.1\}$ (Case 2) and $\{18, 0.7, 1.1\}$ (Case 3). In Case 1, individual arms of the star perform tank-treading motion while in Case 3, the star tumbles as a whole. Case 2 presents a tank-treading-like motion but it is performed by both individual and clustered arms. Circles and squares are guides to follow the motion of arms. In all cases, $N_{\text{pol}} = 40$ and $Wi = 100$. In the panels, Δt represent the elapsed time from the first configuration in τ units.

defined by vectors \mathbf{c}_k , see Eq. (3.12). Since thermally fluctuating (star) polymers do not have such a rigid equilibrium configuration but rather a multitude of typical configurations related to the given conditions (temperature and shear rate), it is plausible to think that, as the simulation advances, the reference configuration needed to built up the Eckart frame must be updated at regularly spaced numbers of MD steps. The period of updating the characteristic, reference configuration is denoted as t_{Eckart} and it can vary at will, from a very frequent update of the reference configuration that tries to follow the details of the particle motion to a rare one, for which the average, time-coarsened rotational dynamics of the molecule is captured.

3 ISOLATED SBC

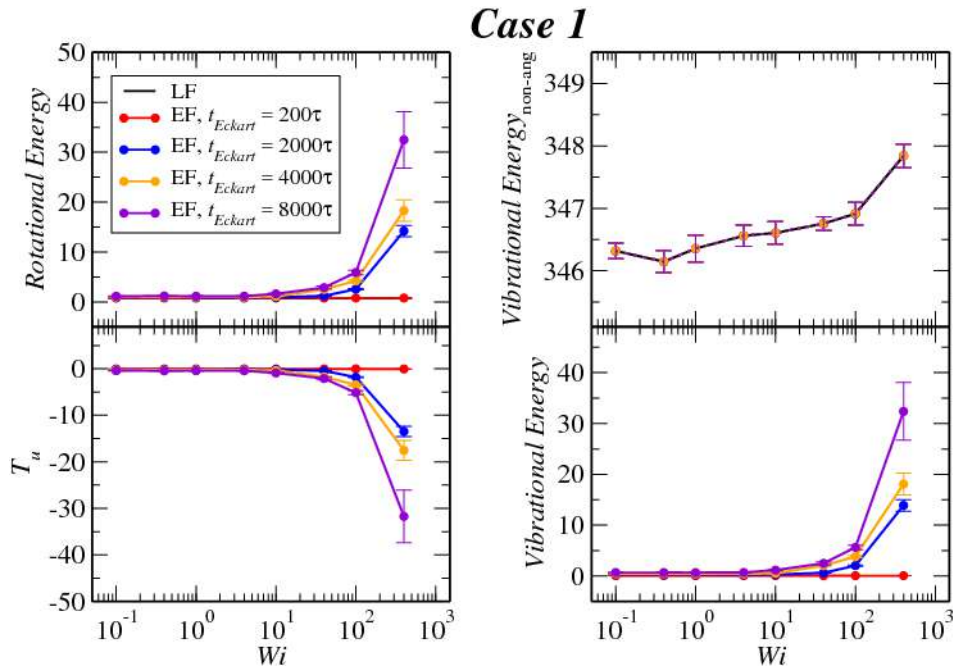


Figure 3.15. Comparison between the values of the kinetic energy for the Case 1 evaluated in both the lab and Eckart frames at different Eckart times (Table 3.2).

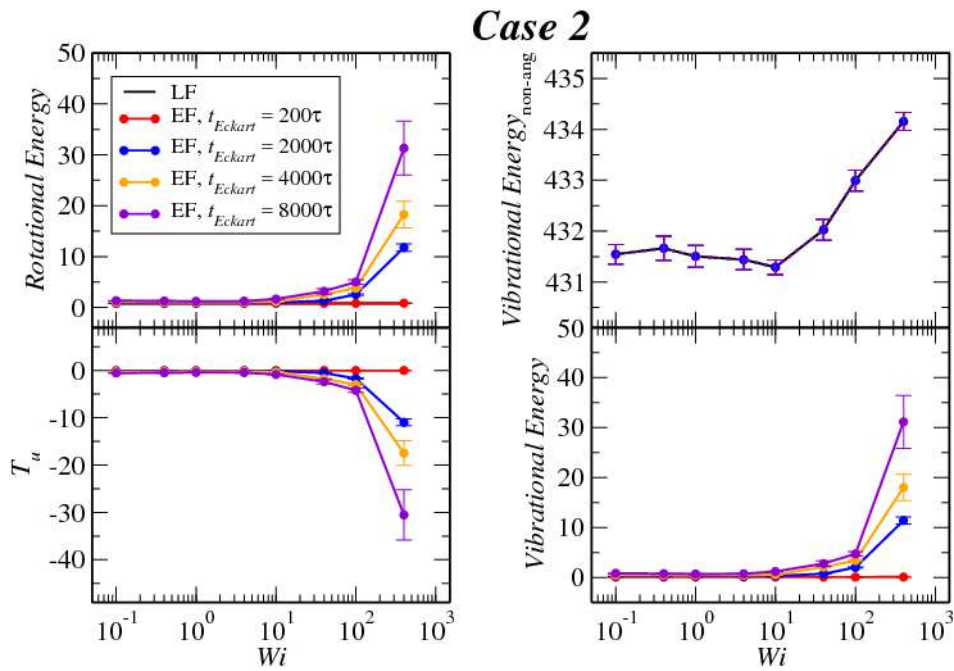


Figure 3.16. Comparison between the values of the kinetic energy for the Case 2 evaluated in both the lab and Eckart frames at different Eckart's times (Table 3.2).

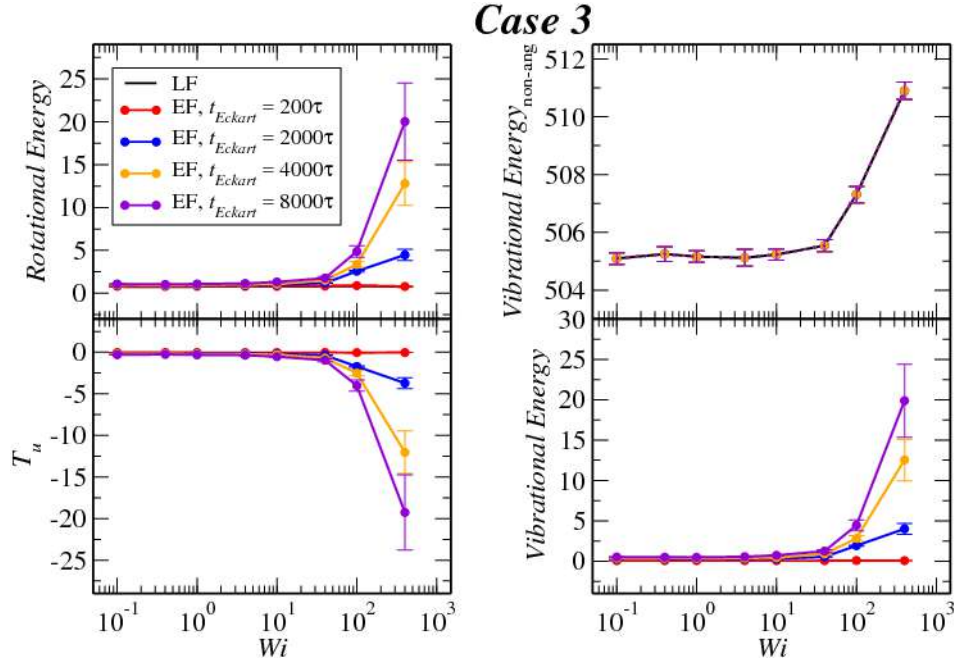


Figure 3.17. Comparison between the values of the kinetic energy for the Case 3 evaluated in both the lab and Eckart frames at different Eckart's times (Table 3.2).

In Figures 3.15–3.17, we compare the behavior of the different contributions to the kinetic energy (see Table 3.2) as a function of the Weissenberg number for different values of t_{Eckart} . For $t_{\text{Eckart}} = 200 \tau$, the rotational energy grows very slowly with Wi (it is essentially constant) and it coincides with the value that it obtains at the laboratory. In this case, where the reference configuration is updated very frequently, the rotational frequencies ω and Ω in the LF and the EF are very similar, i.e., $\omega \simeq \Omega$ and also $\hat{\mathbf{J}} \simeq \mathbf{J}$, resulting into the approximate equality of rotational energies:

$$\frac{1}{2} \omega \cdot \mathbf{J} \cdot \omega \simeq \frac{1}{2} \Omega \cdot \hat{\mathbf{J}} \cdot \Omega \quad (3.26)$$

Related to this approximate equality is the vanishingly small value of the kinetic energy contribution T_u , which emerges as the sum of the angular-momentum-carrying contributions and the Coriolis coupling, viz.:

$$T_u = \frac{M}{2} \sum_k \mathbf{u}_k \cdot \mathbf{u}_k + M \sum_k (\Omega \times \mathbf{c}_k) \cdot \mathbf{u}_k. \quad (3.27)$$

The reason for the smallness of this term lies therein that the quantity \mathbf{u}_k itself is small. Indeed, since $\mathbf{u}_k = \omega \times \Delta \mathbf{r}_k - \Omega \times \mathbf{c}_k$, the proximities of angular velocities and configurations ($\Delta \mathbf{r}_k \cong \mathbf{c}_k$) implies the smallness of \mathbf{u}_k and of both terms at the right-hand side of Eq. (3.27) above. Another

3 ISOLATED SBC

useful way to look into the quantity T_u is to express it as (see Appendix 3C):

$$T_u = \frac{1}{2} \boldsymbol{\omega} \cdot \mathbf{J} \cdot \boldsymbol{\omega} - \frac{1}{2} \boldsymbol{\Omega} \cdot \hat{\mathbf{J}} \cdot \boldsymbol{\Omega}. \quad (3.28)$$

Evidently, T_u is the difference in the rotational energies between the LF and EF and its small value affirms the similarity of the two for frequent updates of the reference configuration in the Eckart frame.

Upon increasing the time intervals between updates of the reference configuration, deviations between the LF and the EF appear in the strongly nonlinear regime, $Wi > 10$. The EF rotational energy grows much higher than its LF counterpart, signaling significant deviations between the (temporally coarse) EF angular velocity $\boldsymbol{\Omega}$ and its LF-counterpart $\boldsymbol{\omega}$. This phenomenon is consistently accompanied by an increase in the magnitude of T_u as well as an increase in the magnitudes of the velocities \mathbf{u}_k , leading to a growth of the angular-momentum carrying vibrational parts of the energy. The second term at the right-hand side of Eq. (3.27) is the Coriolis term E_C , which can be rewritten in the form

$$E_C = E_{C,1} + E_{C,2}$$

$$M \sum_k (\boldsymbol{\Omega} \times \mathbf{c}_k) \cdot \mathbf{u}_k = -M \sum_k (\boldsymbol{\Omega} \times \boldsymbol{\rho}_k) \cdot \mathbf{u}_k + M \sum_k (\boldsymbol{\Omega} \times \Delta \mathbf{r}_k) \cdot \mathbf{u}_k, \quad (3.29)$$

defining the partial terms $E_{C,1}$ and $E_{C,2}$ with the help of the vector $\boldsymbol{\rho}_k = \Delta \mathbf{r}_k - \mathbf{c}_k$, Eq. (3.30). The behavior of each term of the Eq. (3.29) is shown in Fig. 3.18 only for case 1 as representative for all other cases as well. For $t_{\text{Eckart}} = 200 \tau$, the Coriolis coupling is close to zero but for $t_{\text{Eckart}} = 400 \tau$ the Coriolis coupling is negative and the contribution related to $\boldsymbol{\rho}_k$, second term in the right Eq. (3.29), is the dominant in the Coriolis coupling behavior.

Finally, the vibrational kinetic energy associated with the velocities carrying no angular momentum, $E_{\text{vib}} = (M/2) \sum_k \tilde{\mathbf{v}}_k \cdot \tilde{\mathbf{v}}_k$, is very large and its value is essentially independent of t_{Eckart} : the stars have a large number of breathing and fast oscillatory modes. Even for the case of short Eckart times, for which the quantities $\boldsymbol{\rho}_k$ and \mathbf{u}_k are small, the quantities $\dot{\boldsymbol{\rho}}_k = \tilde{\mathbf{v}}_k + \mathbf{u}_k \simeq \tilde{\mathbf{v}}_k$ are significant, and denote fast oscillations of the corresponding displacement variables.

3.5.7 Angular momentum and angular frequency

We now proceed to our results regarding the angular momenta and frequencies of the SBC motions under shear flow. In Fig. 3.19 we compare the component of the total angular momentum around the vorticity direction L_3 in the laboratory frame from Eq. (3.3) to the value evaluated through the geometric approximation, Eq. (3.24). The velocity of the monomers for intermediate

3 ISOLATED SBC

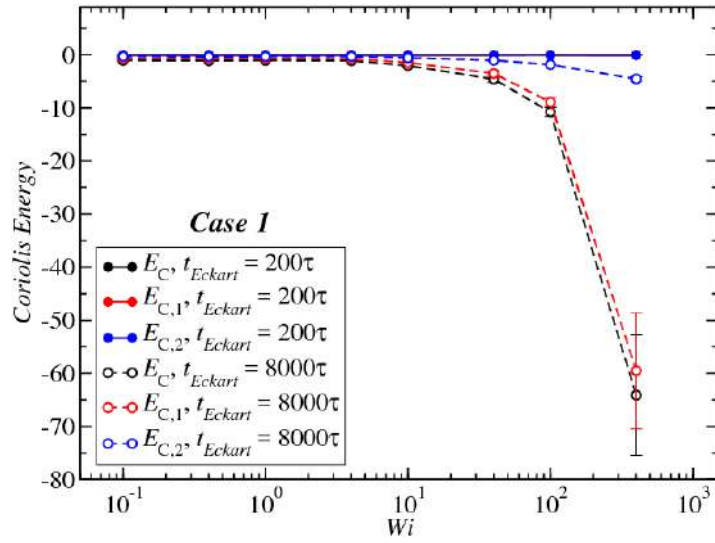


Figure 3.18. The Coriolis coupling for two different values of t_{Eckart} for the case 1 as a function of Wi . For the meaning of the quantities E_C , $E_{C,1}$ and $E_{C,2}$, see Eq. (3.29).

values of Wi is well approximated by Eq. (3.23), i.e., it is mainly determined by the velocity of the fluid, at least in the average sense.

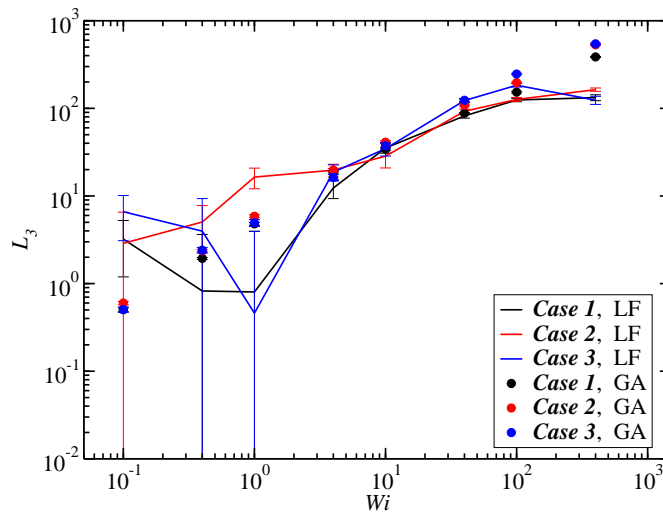


Figure 3.19. Comparison between the exact value of the component L_3 of the angular momentum, Eq. (3.3), with the one obtained from the geometrical approximation, Eq. (3.24).

Results for the angular frequency as a function of Wi and the dependence of this function on the frame of reference as well as on the configuration update time t_{Eckart} are shown in Figs. 3.20–3.22, right panels. According to our analysis, since the block copolymer stars under consideration are very soft systems, the frequency of rotation in the Eckart frame should be closer to the geometrical

3 ISOLATED SBC

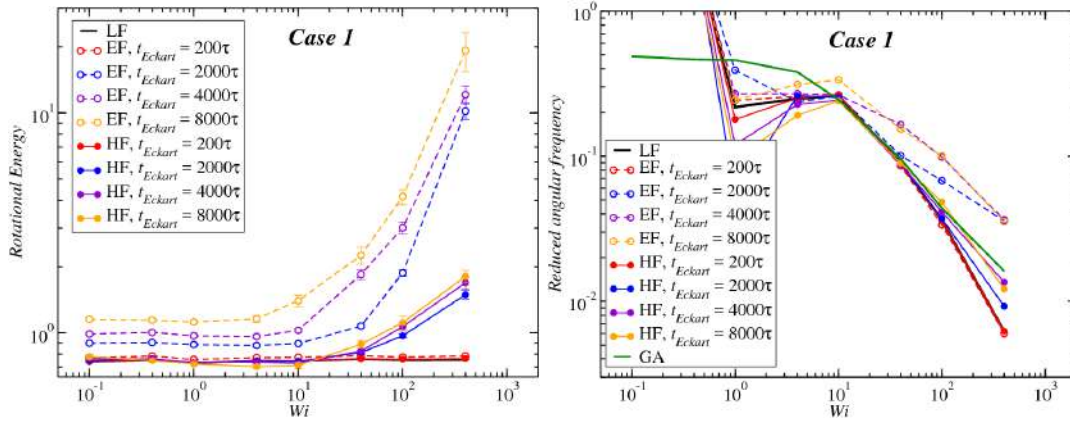


Figure 3.20. Left panel: Rotational energy (LF $\rightarrow \frac{1}{2}\boldsymbol{\omega} \cdot \mathbf{J} \cdot \boldsymbol{\omega}$, EF $\rightarrow \frac{1}{2}\boldsymbol{\Omega} \cdot \hat{\mathbf{J}} \cdot \boldsymbol{\Omega}$, HF $\rightarrow \frac{1}{2}\mathbf{W} \cdot \hat{\mathbf{J}} \cdot \mathbf{W}$) for the different frames a function of the Weissenberg number Wi . Right panel: reduced angular frequency for case 1 (LF $\rightarrow \boldsymbol{\omega}/\gamma$, EF $\rightarrow \boldsymbol{\Omega}/\gamma$, HF $\rightarrow \mathbf{W}/\gamma$, GA $\rightarrow \boldsymbol{\omega}_G/\gamma$) as a function of Wi for different Eckart times.

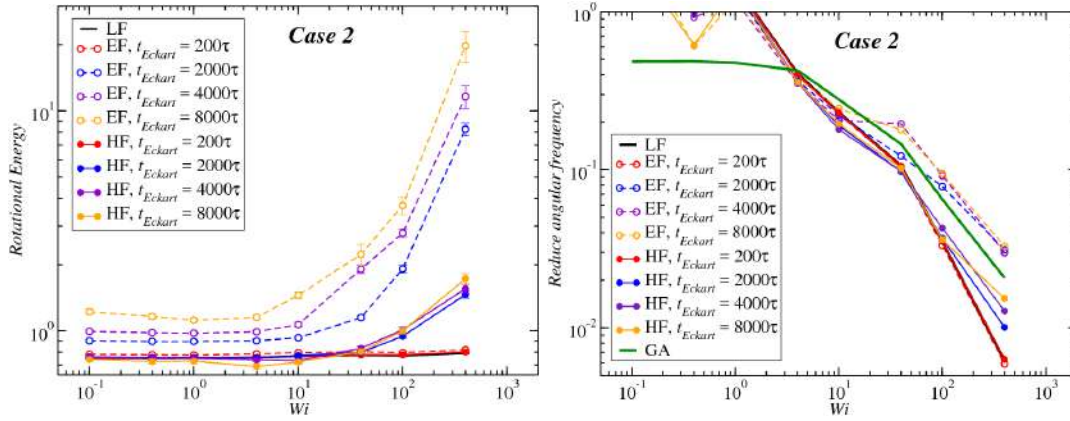


Figure 3.21. Same as Figure 3.20 but for Case 2.

approach and therefore one would expect that the decay law for high Wi should be the same in both approximations for sufficiently long updating intervals t_{Eckart} . Our findings confirm that, indeed, the Eckart rotation frequencies lie closer to those from the geometric approximation and they have the ones obtained by the laboratory frame analysis as a lower bound. As t_{Eckart} grows, the Eckart rotation frequencies move from the LF- towards and beyond the GA-curves, confirming the fact that at coarse time scales the stars, at least for Cases 1 and 2, can be thought of as soft colloids with a tank-treading type of motion of the polymers in their interior.

Case 3 seems exceptional, in the sense that the angular frequency evaluated in the EF appears to be almost independent of the parameter t_{Eckart} and always very close to the GA-result. This is an indication of the fact that, contrary to the other two cases, these star block copolymers do not behave as tank-treading soft colloids. On the contrary, and consistently with their rather compact, elongated, dumbbell-shape, they rotate similarly to rigid prolate ellipsoids under constant shear

3 ISOLATED SBC

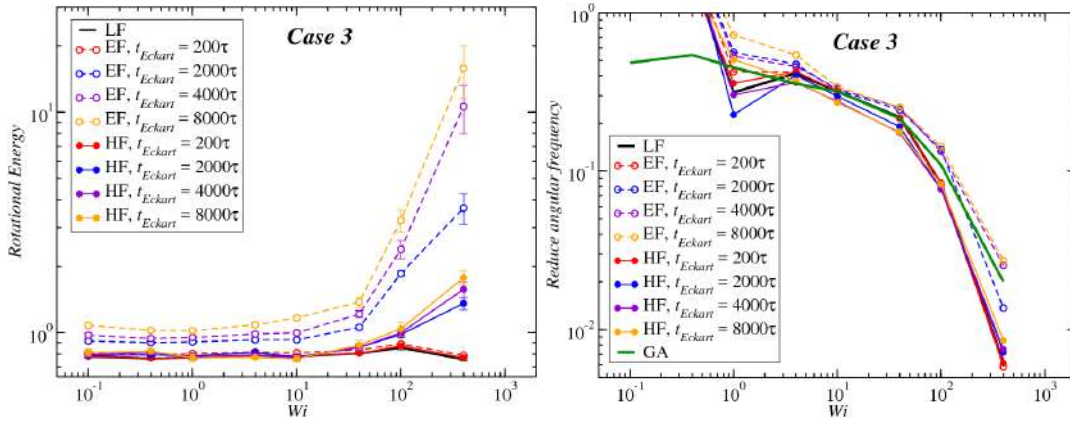


Figure 3.22. Same as Figure 3.20 but for Case 3.

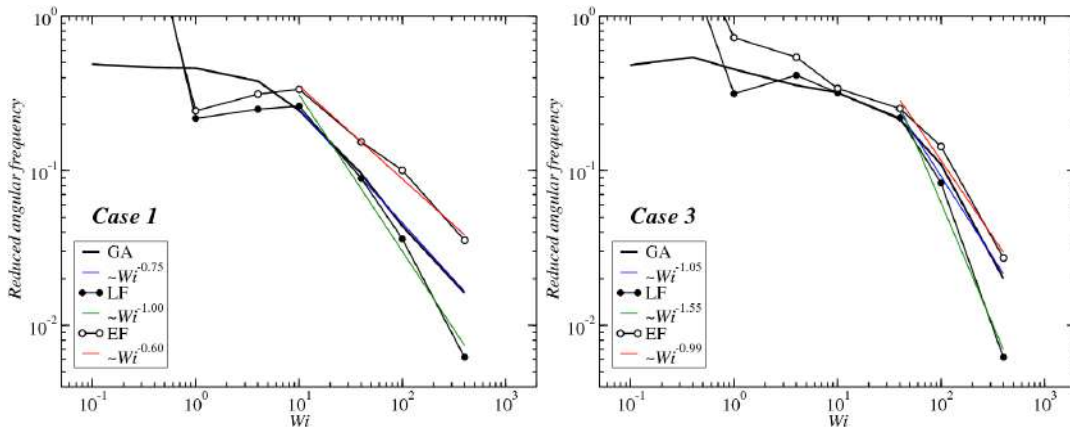


Figure 3.23. The reduced angular frequencies for Case 1 (left) and Case 3 (right) evaluated at the LF, the GA and the EF with the longest Eckart time employed, $t_{\text{Eckart}} = 8000 \tau$.

flow. In particular, the GA-assumption of isolated monomers, each of which is carried through the solvent with the local velocity of the streaming solvent, are responsible for giving these molecules the character of rigid-like, stiff objects, as opposed to the very soft and flexible polymers of Case 1, for which associations among the end-monomers are rare and easily breakable. To emphasize the difference between Case 1 and Case 3, in Fig. 3.23 we plot the angular frequencies for the two limiting frames, LF and GA, together with the EF-result at the longest Eckart time, $t_{\text{Eckart}} = 8000 \tau$. As it can be seen, whereas for Case 1 the EF frequencies exceed both the LF and the GA-ones; for Case 3, EF and GA are very close to one another. Differences in the power-law behavior for large values of Wi between the two cases can also be seen.

3.6 Conclusions

The behavior of patchiness and shape of low-functionality, star block-copolymers in shear flow has been quantitatively analyzed for different values of amphiphilicity and solvent quality. This has been achieved for Weissenberg numbers ranging from $Wi = 0$ (equilibrium) to larger than 10^3 , the latter lying deeply into the nonlinear regime. We have shown that these polymers respond to shear stresses qualitatively differently from athermal stars when the attraction between their solvophobic blocks is sufficiently high and that shear can be utilized as yet another parameter in tuning their self-assembly next to functionality, amphiphilicity, solvent quality, and temperature. While shear increases the patchiness of low amphiphilicity SBCs as a result of their alignment with the flow field, we have found that for high amphiphilicity stars the number and size of patches formed are non-monotonic functions of shear rate. This might have interesting implications on the system's rheological properties and viscoelastic responses in dilute bulk phases since the macro- and microscopic phase behavior of SBCs in equilibrium is governed by their number of association sites or patches. Furthermore, we were able to demonstrate that high amphiphilicity SBCs deform differently than athermal star polymers in the regime of intermediate Weissenberg numbers.

The understanding of how the average number of patches $\langle N_p \rangle$ changes depending on the system parameters $(f, N_{\text{pol}}, \alpha, \lambda, Wi)$ is a key point to tune the functionalization of these molecular building blocks, and hence their hierarchical self-assembling process, without the need to change the molecules in solution [23]. We have found quasi-universal characteristics of the shape and patchiness of the SBCs underflow, which show that knowledge of the star properties in equilibrium can lead to reliable predictions for its behavior in different regimes of the shear rate. In particular, key factors in determining the evolution of the star patchiness and shape under shear are (i) the presence (or absence) of any non-associated arms at equilibrium and (ii) the spatial extent of the original patches. The main mechanisms for patch evolution under shear have been established, these being (i) merging of free arms into new patches (ii) fusion of two patches into one and (iii) fission of existing, bulky patches under strong shear. The antagonistic effects of these sometimes bring about non-monotonic effects on the dependence of patchiness under shear.

We analyzed the rotational dynamics of an isolated star-shaped block copolymer under shear flow for three representative sets of parameters, i.e., a very flexible system (case 1), an intermediate flexible-rigid system (case 2) and finally a rather rigid system (case 3). Motivated by very recent studies on polymer dynamics [67, 68], we explored the quantitative predictions emerging from the employ of the Eckart frame formalism, and compare them to the resulting ones from two different approaches (lab frame and geometrical approach). Additionally, we performed an analysis of each term in the kinetic energy and the contributions of the various kinetic terms to it.

In addition to the standard Eckart formalism [73], extended to polymers underflow in [68, 71, 72], we suggested a 'hybrid' definition of the rotation frequency. As a consequence, we obtained

3 ISOLATED SBC

different analytical approximations for the total kinetic energy and for the numerical value for the rotational frequency of the SBC, which we express using strictly the Eckart's variables. It is important to note that both treatments reproduce correctly the results for the laboratory frame for small updating time t_{Eckart} ($t_{\text{Eckart}} \sim 200\tau$); however for $t_{\text{Eckart}} > 200\tau$, we found differences between both treatments, particularly for the rotational energy term. For $Wi < 10$, we found that the rotational energy is independent of t_{Eckart} in the hybrid formulation, which is not the case for the rotational energy associated with the Eckart rotational frequency. Additionally, both the rotational energy and frequency found in [68] are larger than the outcomes from the hybrid treatment.

The main result concerns the behavior of the associated rotational frequency Ω at high shear rates ($Wi > 100$) for the three different systems. We found that for all cases Ω is bounded from below by the rotational frequencies obtained in the lab frame (ω). For the third case, i.e., self-assembled, dumbbell-like SBC, $\Omega \approx \omega_G$ for sufficiently large values for the updating time t_{Eckart} , demonstrating that the rotation frequency mainly corresponds to tumbling motion of the SBC induced by the shear flow. On the other hand, for case 1, which is closely related to athermal star polymers, the results obtained from the geometrical approximation are consistent with the Eckart frame only for long enough t_{Eckart} ; therefore, the geometrical approximation only captures the average, time-coarsened tank-treading rotational frequency of the polymer. These results agree with the obtained for athermal stars with smaller polymerization degree ($N_{\text{pol}} = 6$), for which was found that the vibrational angular momentum has a larger contribution for softer polymers [68].

The dynamics of the case 2 is richer; although this system features four patches in average, the shear causes those patches to break and to cluster over and over again. Therefore, here the rotational frequency results from the average of the tank-treading motion of free and clustered arms. It remains to establish a more detailed description regarding the statistic of the typical times between break-up and rejoin events, which shed light on their influence on the rheology of semi-dilute suspensions, in particular on the expected shear thinning behavior and how it can be tuned by the amphiphilicity and the solvent quality [57].

Appendix 3A: Rotation frequencies

In Figure 3.24, we show results for all components of the angular frequency. In general, we find that the angular velocity in the vorticity axis is dominant in the angular frequency vector, especially as Wi grows. The vorticity component ω_3 approaches a constant value at high values of Wi or even shows a decrease there, in Case 3.

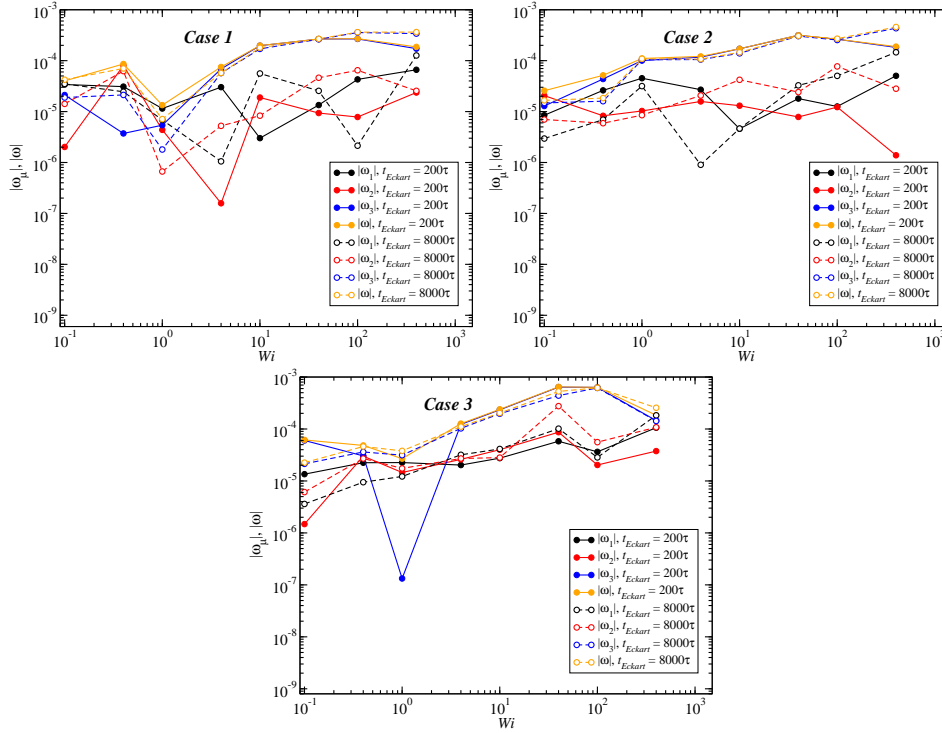


Figure 3.24. Values of the average magnitudes of the components of the angular velocity, $|\omega_\mu|$, and the magnitude of the whole vector, $|\omega|$, for case 1 as a function of Wi for two different values of the t_{Eckart} as indicated in the legend, for Cases 1,2, and 3.

Appendix 3B: Kinetic energy in the Eckart frame

The definition of the displacement vector $\boldsymbol{\rho}$ compatible with the Eckart frame [68, 73, 74] reads as:

$$\boldsymbol{\rho}_k = \Delta \mathbf{r}_k - \mathbf{c}_k, \quad (3.30)$$

Taking the time derivative we find the equation of motion:

$$\dot{\mathbf{r}}_k = \dot{\mathbf{r}}_{cm} + (\boldsymbol{\Omega} \times \mathbf{c}_k) + \tilde{\mathbf{v}}_k + \mathbf{u}_k. \quad (3.31)$$

We note that for $t_{\text{Eckart}} = 200 \tau$, $\boldsymbol{\omega} \approx \boldsymbol{\Omega}$, $\Delta \mathbf{r}_k \approx \mathbf{c}_k$ and $\mathbf{u}_k \approx \mathbf{0}$ (see Section 3.5.6). Concomitantly with Eq. (3.31), the resulting kinetic energy is

$$\begin{aligned} \frac{M}{2} \sum_k \dot{\mathbf{r}}_k \cdot \dot{\mathbf{r}}_k &= \frac{M_s}{2} \dot{\mathbf{r}}_{cm} \cdot \dot{\mathbf{r}}_{cm} + \frac{M}{2} \sum_k (\boldsymbol{\Omega} \times \mathbf{c}_k) \cdot (\boldsymbol{\Omega} \times \mathbf{c}_k) + \frac{M}{2} \sum_k \tilde{\mathbf{v}}_k \cdot \tilde{\mathbf{v}}_k + \frac{M}{2} \sum_k \mathbf{u}_k \cdot \mathbf{u}_k + \\ &\quad \dot{\mathbf{r}}_{cm} \cdot (\boldsymbol{\Omega} \times M \sum_k \mathbf{c}_k) + \dot{\mathbf{r}}_{cm} \cdot M \sum_k \tilde{\mathbf{v}}_k + \dot{\mathbf{r}}_{cm} \cdot M \sum_k \mathbf{u}_k + \\ &\quad M \sum_k (\boldsymbol{\Omega} \times \mathbf{c}_k) \cdot \tilde{\mathbf{v}}_k + M \sum_k (\boldsymbol{\Omega} \times \mathbf{c}_k) \cdot \mathbf{u}_k + M \sum_k \tilde{\mathbf{v}}_k \cdot \mathbf{u}_k. \end{aligned} \quad (3.32)$$

Since the following equalities hold [73, 74],

$$M \sum_k \mathbf{c}_k = \mathbf{0}, \quad (3.33)$$

$$M \sum_k \Delta \dot{\mathbf{r}}_k = M \boldsymbol{\Omega} \times \sum_k \mathbf{c}_k + M \sum_k \tilde{\mathbf{v}}_k + M \sum_k \mathbf{u}_k = \mathbf{0} \rightarrow M \sum_k \mathbf{u}_k = \mathbf{0}, \quad (3.34)$$

and the definition of \mathbf{u}_k implies

$$M \sum_k \tilde{\mathbf{v}}_k \cdot \mathbf{u}_k = M \sum_k \tilde{\mathbf{v}}_k \cdot (\boldsymbol{\omega} \times \Delta \mathbf{r}_k) - M \sum_k \tilde{\mathbf{v}}_k \cdot (\boldsymbol{\Omega} \times \mathbf{c}_k) = -M \sum_k \tilde{\mathbf{v}}_k \cdot (\boldsymbol{\Omega} \times \mathbf{c}_k), \quad (3.35)$$

then the kinetic energy can be expressed as in Eq (3.17).

Appendix 3C: Explicit calculation of T_u

Starting with the definition of vector \mathbf{u}_k , Eq. (3.31), the energy T_u (Table 3.2) can be written as,

$$\begin{aligned} T_u &= \frac{M}{2} \sum_k \mathbf{u}_k \cdot \mathbf{u}_k + M \sum_k (\boldsymbol{\Omega} \times \mathbf{c}_k) \cdot \mathbf{u}_k \\ &= \frac{M}{2} \sum_k (\boldsymbol{\omega} \times \Delta \mathbf{r}_k - \boldsymbol{\Omega} \times \mathbf{c}_k) \cdot (\boldsymbol{\omega} \times \Delta \mathbf{r}_k - \boldsymbol{\Omega} \times \mathbf{c}_k) + M \sum_k (\boldsymbol{\Omega} \times \mathbf{c}_k) \cdot (\boldsymbol{\omega} \times \Delta \mathbf{r}_k - \boldsymbol{\Omega} \times \mathbf{c}_k). \end{aligned} \quad (3.36)$$

Grouping in a convenient way,

$$T_u = \frac{1}{2} (\boldsymbol{\omega} \cdot \mathbf{J} \cdot \boldsymbol{\omega} + \boldsymbol{\Omega} \cdot \boldsymbol{\mathcal{J}} \cdot \boldsymbol{\Omega} - 2M(\boldsymbol{\omega} \times \Delta \mathbf{r}_k) \cdot (\boldsymbol{\Omega} \times \mathbf{c}_k)) + (M(\boldsymbol{\omega} \times \Delta \mathbf{r}_k) \cdot (\boldsymbol{\Omega} \times \mathbf{c}_k) - \boldsymbol{\Omega} \cdot \boldsymbol{\mathcal{J}} \cdot \boldsymbol{\Omega}), \quad (3.37)$$

so that

$$T_u = \frac{1}{2} \boldsymbol{\omega} \cdot \mathbf{J} \cdot \boldsymbol{\omega} - \frac{1}{2} \boldsymbol{\Omega} \cdot \boldsymbol{\mathcal{J}} \cdot \boldsymbol{\Omega}. \quad (3.38)$$

4 | Semidilute and concentrate regimes

In the previous chapter, we showed that the dynamics of isolated SBC under shear flow is rich. The SBC constitute versatile, self-assembling building blocks with tunable softness, functionalization, and shape. The equilibrium properties of SBC networks are studied via computer simulations. We employ both Molecular Dynamics and Multiparticle Collisional Dynamics simulations to investigate the self-organization of SBC with $f = 9$ functionalized arms close to their overlap concentration under conditions of different fractions of solvophobic monomers and varying attraction strength. We find three distinct macroscopic self-organized states depending on the fraction of attractive end-monomers and the strength of the attraction. At weak attractions, ergodic, diffusive liquids result, with short-lived bonds between the stars. As the attraction strength grows, the whole system forms a percolating cluster, while at the same time the individual molecules are diffusive. Finally, arrested gels emerge when the attractions become strong. The conformation of the SBC in these solutions is found to be strongly affected by the concentration, with the stars assuming typically spherical, open configurations in seeking to maximize inter-star associations as opposed to the inter-star collapse that results at infinite dilution, giving rise to strongly aspherical shapes and reduced sizes. In the last part of the chapter, we investigate the dynamical properties of suspensions of SBC under linear shear flow employing extensive particle-based multiscale simulations. We determine the properties of the system for representative values of monomer packing fraction ranging from semidilute to concentrate regimes. We systematically analyze the formed network structures as a function of both the shear rate and the packing fraction, the reorganization of solvophobic patches, and the corresponding radial correlation functions. Connecting our findings with rheology, we calculate the viscosity as a function of the shear rate and discuss the implications of the found shear thinning behavior.

4.1 Introduction

For finite densities, when the block copolymer stars interact with one another, most of what is known is based on Monte Carlo simulations of lattice models [25–27, 55]. It has been shown there that for low functionalities and low fractions of functionalized monomers, the SBCs self-organize into micelles, which, as density grows, interconnect and can form elongated, wormlike aggregates. For intermediate functionalities and attraction strengths, the growth of extended network structures has been seen in lattice Monte Carlo [26], but neither the structure of the network nor the conformational and dynamical characteristics of the stars in the network have been analyzed. Also, the system has not been investigated at all in the continuum and, of course, no information about the dynamics has been gained from the aforementioned Monte Carlo investigations [25–27, 55], which included several special moves to accelerate equilibrium sampling that are unphysical from the dynamics point of view. Here we perform detailed Molecular Dynamics and Multiparticle Collisional Dynamics simulations to analyze the structure and the diffusion dynamics of concentrated solutions of SBCs of intermediate functionalities, $f = 9$. Since at infinite dilution these soft patchy colloids have the form of dumbbells [23], they do not self-organize into micelles but, rather, they form networks. We find, however, that in forming these networks the SBCs become reconfigured concerning their infinite-dilution conformation, assuming in concentrated solution rather open, spherical shapes in attempting to maximize inter-star association. Our model system has many similarities with the telechelic star polymers in the recent work of Metri [81] who performed a joint experimental and simulation investigation of the stress-relaxation and rheological properties of the physical networks formed by these molecules.

From a general dynamical point of view, the behavior of dilute solutions of associative polymers is mainly determined by intramolecular associations, while in the semi-diluted non-entangled regime, where an interplay between inter- and intra-molecular associations takes place, viscoelastic properties are expected to be characterized by at least by two-time scales, i.e., the typical time for formation and breakage of intermolecular associations and the relaxation time of inter-molecular chain segments [34]. Of course, these factors influence the response of the system in non-equilibrium conditions.

For example, telechelic, linear polymers assemble in equilibrium into scaffold-like networks, whose properties are governed by the polymer flexibility and end-attraction strength [66]. In these systems, shear flow induces significant (reversible) structural changes that can be associated with major rheological regimes which, depending on the strength of the applied shear flow, include Newtonian behavior, shear banding and shear thinning [66, 82].

In isolated SBCs the shear can be utilized as yet another parameter for tuning the intra-molecular self-assembly behavior. Shear increases the patchiness of low-amphiphilic-fraction SBC's, i.e., $\alpha \lesssim 0.3$, as a result of their alignment with the flow field, while for high-amphiphilic-fraction stars,

4 SEMIDILUTE AND CONCENTRATED REGIMES

i.e., $\alpha \gtrsim 0.7$, the number and size of patches formed are non-monotonic functions of shear rate. The key factors in determining the evolution of the star patchiness and global configuration under shear are the presence of non-associated arms and the spatial extent of the patches. Depending on these factors, the main mechanisms for patch evolution under shear involve the merging of free arms into new patches, the joining of two patches into one, and the split-off of bulky patches under strong shear [83].

On the other hand, for semi-dilute solutions of low functionality telechelic star polymers ($f \leq 3$), which also form connected networks, an increasing viscosity is predicted as the concentration, the functionality or the attraction between B-monomers increases [28, 56]. Furthermore, the steady-state response of these solutions under shear flow features both Newtonian and shear-thinning behaviors, the latter being linked to the fission of inter- and intra-star patches.

The aforementioned examples show how differences in the structure of associating polymers give rise to large changes in their properties. Until now, studies under shear flow have been carried out for three- or four-armed SBCs. Since it is expected that larger functionality SBCs facilitate the formation of stiffer networks than those of lower functionality and similar mass [84]. We systematically analyze the effect of shear flow on the global structure and the molecular conformations of the SBCs in reversible percolating systems which are not too dense yet topologically interesting. For these systems, our results suggest that the orientation and elongation of the SBCs induced by the shear flow, give rise to the reorganization of both the patchiness and the network connectivity, leading to shear thinning behavior with the thinning exponent growing in magnitude with the concentration of the solution.

The rest of this chapter is organized as follows: In Sec. 4.2 we present the model employed for the SBCs system with implicit solvent, and the values of the parameter for the hybrid simulation (Sec. 2.5). In Sec. 4.3 we present and analyze our results on association, network formation and connectivity characteristics, pair correlations and equilibrium diffusion. In Sec. 4.4 is devoted to extensively present and discuss our results regarding the conformation properties, the patchiness, and the viscosity of the system as a function of the shear rate and the packing fraction. Finally, In Sec. 4.5 we summarize and draw our conclusions.

4.2 Model and Methods

For the static equilibrium properties, we employed two simulation approaches: considering the solvent implicit and performing molecular dynamics simulations (Star Block Polymers method, Sec. 2.3), by modeling the macromolecules with $f = 9$, $N = 30$. We perform NVT Molecular Dynamics simulation of SBC, we keep the temperature fixed at $k_B T = 0.5$ using a Nosé-Hoover thermostat. The strength of the attractive potential was varied from $\lambda = 1$ to $\lambda = 1.75$. We start each simulation with all SBCs, which are randomly distributed in the simulation box, in an

4 SEMIDILUTE AND CONCENTRATED REGIMES

open star configuration i.e., one in which no attractive beads are aggregated; this is equivalent to abruptly lowering the temperature at the beginning of our simulation time. For the single-star simulations, we placed one single star in a cubic box with periodic boundary conditions of side length $L = 200\sigma$. For the networks we simulated $N_s = 52$ SBCs in a box of linear size $L = 50\sigma$, which amounts to a monomer volume fraction $\phi = \frac{v_0 n}{L^3} = 0.06$, where $V_0 = \frac{\pi}{6}(Nf\sigma^3 + \sigma_{anchor}^3)$ is the volume of one SBC considered as the sum of the monomers forming it. Typical runs consist of 10^7 molecular dynamics steps with a time-step $\Delta t = 0.002\tau$. Equilibrium times are in the order of 10^6 MD steps. And by explicitly representing the solvent using the MPCD method (Sec. 2.4), but in this case, the number of SBC is $N_s = 35$ (see chapter 2 in sec. 2.3.2). Even if the second approach may seem more realistic, it is also much more demanding computationally. We found that differences between the two approaches are within simulation error bars, as they should, since in equilibrium, hydrodynamics, which is present in the MPCD-MD scheme, has no influence on the system properties.

For the dynamical properties, We focus our study on three particular values, $\phi = 0.01, 0.06$ and 0.1 . The lowest volume fraction corresponds to a dilute regime in which SBC interact, forming small inter-star associations. At the intermediate ϕ , the SBCs form in equilibrium a percolating network even if this volume fraction accounts only for around $0.65\phi^*$, with $\phi^* = V_0 / \left[(4/3)\pi R_{gyr}^3 \right]$ being equivalent to the polymer overlap concentration, where R_{gyr} denotes the gyration radius of an isolated SBC at equilibrium. Finally, the highest ϕ -value lies above the overlap concentration ($\phi \sim 1.67\phi^*$), where well-formed gels are obtained. The shear rates $\dot{\gamma}$ considered in this part lie in the range between $10^{-4} \tau^{-1}$ and $4 \times 10^{-2} \tau^{-1}$. To facilitate comparison with other results, the shear rate can be expressed by the Weissenberg number with $\tau_z \approx 7.5 \times 10^3 \tau$ and consequently, the range of Weissenberg numbers covered goes from $Wi \sim 0.75$ to $Wi \sim 300$. Lastly, four independent runs for each considered set of parameters $\{\alpha = 0, 3, 0, 5, \lambda = 1, 1, f = 9, \phi, \dot{\gamma}\}$.

4.3 Equilibrium Properties

4.3.1 Network Structure and Pair Correlations

In the very dilute regime, where single SBCs cannot feel each other, these macromolecules have been found to self-assemble by bringing together the attractive part of the arm to form monomer aggregates that we call *patches*. The number and size of these aggregates depend on a few physical parameters such as the number of arms per star, the fraction of functionalized monomers, and the strength of the attractive interaction [23] i.e., f , α and λ . The number of patches increases with the functionality f of the star for a fixed value of the attraction strength λ . Since we aim to assemble polymer-based networks, it is wise to choose as building blocks SBCs that do not form one single patch at infinite dilution, the so-called *watermelon configuration* [85], since these

4 SEMIDILUTE AND CONCENTRATED REGIMES

stars are likely to only further assemble into micelles upon increasing the concentration [25, 86]. Even when these micelles open up and form inter-micellar connections as concentration increases [55], the resulting connected networks have the form of assemblies of wormlike micelles [87, 88] interconnected via individual polymeric arms [89, 90], as we also confirmed in the present work. Although the structure and rheology of such (interconnected) solutions of wormlike micelles are very interesting topics in their own right, and they have received considerable attention for *linear* block terpolymer-based solutions [89–95], these do not lie within the focus of the current work. Nevertheless, we have performed also simulations of low-functionality ($f = 4$) SBC-solutions to accompany our main results on the intermediate-functionality case studied here and provide a comparison to it, and we will discuss these differences later on.

We are also not interested in probing the regime of high functionality, in which the SBCs would behave like multi-patchy soft colloids. We, therefore, focus instead on SBCs with moderately high functionality, $f = 9$, having $N = 30$ monomers per arm which are, by considering that our monomers are equivalent to one Kuhn length, realistic in terms of possible experimental realizations such as polyisoprene/polystyrene block copolymers [96]. For this functionality, both off- and on-lattice simulations [24, 26, 97] have shown that homogeneous, extended networks form at sufficiently high concentrations. We find that, at functionalization fraction of $\alpha = 0.3$, the SBCs are, for low attraction strength ($\lambda < 1.25$), in an open star configuration, i.e., arms are not usually bound together, see Fig. 4.1(a). In this type of configuration, even if sometimes two arms bind through their attractive end-blocks, this patch is transient, being relatively fast disassembled and surviving only for $\approx 10\,000$ MD steps. In this regime, even if we are below the Θ -point corresponding to the chosen attractive potential [23] ($\lambda_\Theta = 0.92$), the thermal fluctuations are strong enough to overcome the gain in potential energy due to patch assembly. Compared to previously published data [23], where open stars have been observed for $\lambda \leq 1.0$, the increase in λ found here is due to the relative length of the arms: shorter arms (which is the case in the present study) make it harder for the attractive blocks to meet and bind, hence observation of open stars for higher λ . For $\lambda > 1.55$ we observe that the SBC self assembles into an aggregate that features two patches, see Fig. 4.1(c). Each of these patches, containing either 4 or 5 arms, is located at roughly the same distance from the anchor, on opposite sides of the latter. Due to its shape, we refer to this configuration as “dumbbell”. In the region $\lambda \in [1.25, 1.55]$, we find a transition regime between the two previously described configurations. The SBCs has typically a few arms assembled into one or more patches, while some arms remain free, as shown in Fig. 4.1(b). For the case of a longer attractive block, $\alpha = 0.5$, the trend is similar to the one of lower functionalization: below $\lambda = 1.05$ the stars are open; the transition regime can be found in between $\lambda = 1.05$ and $\lambda = 1.35$, while above this value we find the dumbbell configuration. As opposed to the $\alpha = 0.3$ case, we find, at the highest values considered for the attraction strength $\lambda = 1.75$, watermelon structures. The characterization of the SBC configurations was done based on the shape parameters and will be

4 SEMIDILUTE AND CONCENTRATED REGIMES

discussed later on.

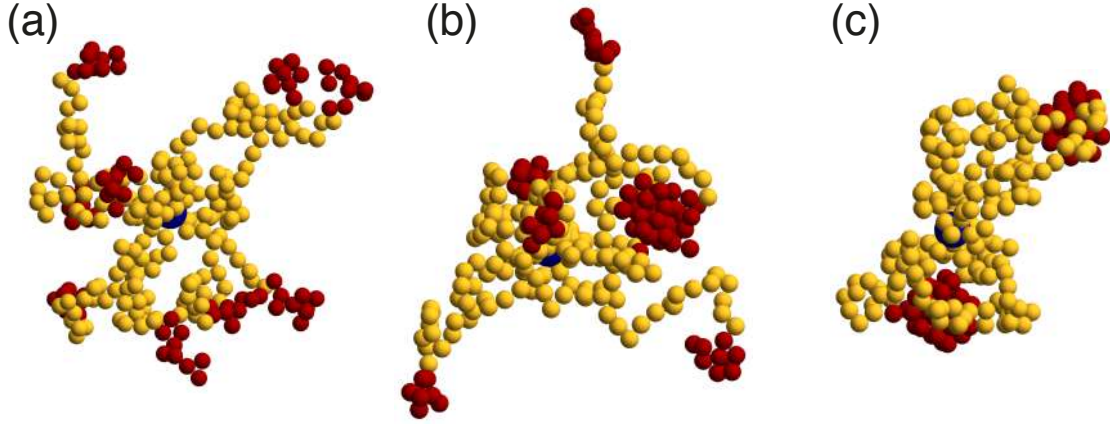


Figure 4.1. Single star configurations. Functionalized monomers are shown in red, non-attractive ones in yellow and anchors in dark blue. The strength of the attraction is: (a) $\lambda = 1.1$, (b) $\lambda = 1.35$, and (c) $\lambda = 1.6$. All shown results were obtained for a fraction $\alpha = 0.3$ of attractive monomers.

We define the volume fraction ϕ occupied by the monomers as $\phi = (N_s/V)v_0$, with $v_0 = \pi(fN\sigma^3 + \sigma_{anchor}^3)/6$, where N_s the number of stars and V the volume of the simulation box, whilst σ and σ_{anchor} are the diameters of the arm monomers and the anchoring point, respectively. Our systems need to be at a volume fraction of the same order of magnitude as the overlap value ϕ_* , defined as the monomer packing fraction in the interior of the star, $\phi_* = 3v_0/(4\pi R_g^3)$, with the gyration radius R_g of the molecule. For the remainder of this subsection, we focus on a monomer volume fraction $\phi = 0.06$ which corresponds to 65% of the overlap packing fraction ϕ_* , sufficiently high to bring about nontrivial inter-star associations.

Depending on the values of λ and the α , we observe three distinct morphologies of the networks. For low attraction strength, $\lambda \in [1.0, 1.2]$, and for both values of α considered, the attractive terminal blocks of the arms are in close proximity but do not appear to build stable, long-living aggregates, see Figs. 4.2(a) and 4.2(d). As λ is increased, we observe the formation of well-structured aggregates while at the same time, free arms are still present, as shown in Figs. 4.2(b) and 4.2(e). The size of the aggregates increases with λ and at the same time, the number of free arms decreases with attraction strength. At $\lambda = 1.5$ for $\alpha = 0.3$ and at $\lambda = 1.35$ for $\alpha = 0.5$ all arms are bound, i.e., they are attached through their functionalized part to an aggregate to which multiple arms contribute. For $\alpha = 0.5$, at the higher attraction strengths, the network formed opens up voids which are on the order of length of the simulated volume. For these parameters, the attraction strength and the number of functionalized monomers are so high that the network contracts, leaving part of the simulation volume unoccupied, as shown in Figs. 4.2(c) and 4.2(f). This is in agreement with lattice-model simulation results predicting a macroscopic, gas-liquid

4 SEMIDILUTE AND CONCENTRATED REGIMES

phase separation [26] for attractive monomer fractions $\alpha \geq 0.5$.

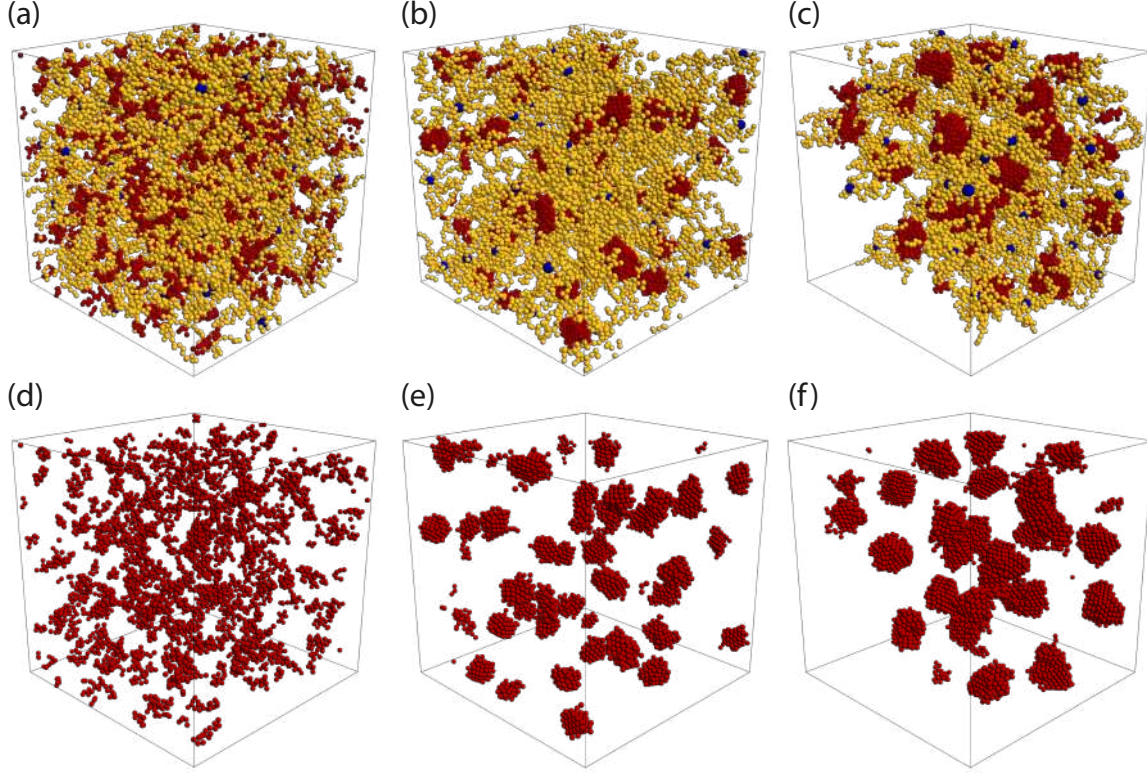


Figure 4.2. Network architecture types. The upper row shows snapshots of the three types of SBC networks observed. On the lower row, only the attractive part of the SBCs from the upper panels has been drawn, to highlight the structure of the attractive aggregates. Parameters for the three configurations are: (a) and (d): $\alpha = 0.3$ and $\lambda = 1.0$; (b) and (e): $\alpha = 0.3$ and $\lambda = 1.35$; (c) and (f): $\alpha = 0.5$ and $\lambda = 1.25$. Color code of the monomers is the same as in Fig. 4.1. Results obtained by MD simulations at $\phi = 0.06$.

To have a quantitative description for the pair structure of attractive aggregates observed, we first look, in similarity to the case of linear telechelic polymers [65], at the pair-correlation function between the attractive monomers, defined as:

$$g(r) = \frac{V}{N_a^2} \left\langle \sum_i \sum_{i \neq j} \delta(\mathbf{r} - \mathbf{r}_{ij}) \right\rangle, \quad (4.1)$$

where $N_a = (\alpha f N) N_s$ is total number of functionalized monomers in our system, r denotes the distance, and \mathbf{r}_{ij} is the position vector between monomers i and j [65, 98]. At low attraction strengths, such as $\lambda = 1$ and $\lambda = 1.1$, we find, as expected, a very pronounced peak at $r = \sigma$ corresponding to monomers adjacent to the one considered, see Fig. 4.3(a). Additionally, two weaker peaks at distance $r \cong 1.7\sigma$ and $r \cong 2\sigma$ exist, which are due to the second shell of close-

4 SEMIDILUTE AND CONCENTRATED REGIMES

packed monomers and the second-order neighbors along the chain, respectively. Peaks at higher values of r are too broad to be analyzed. As the attraction strength is increased, we find the development of multiple peaks at small values of r . The position of these peaks corresponds to a random hexagonal close-packed arrangement, which is in agreement with the organization of the attractive monomers in clusters, which can be seen by the eye in Fig 4.2. It was to be expected that a hexagonal close-packed arrangement occurs within the attractive aggregates since our attractive potential reaches its minimum when the functionalized monomers are in contact, and the most energetically favorable configuration would have each monomer surrounded by the maximum number possible neighbors which are twelve [99], achieved by the hexagonal close-packed arrangement [100]. For $r > 2\sigma$ the pair-correlation for $\lambda = 1.3$ attains higher values than its counterpart for $\lambda = 1.6$. This is because, for the former value, there tend to be more large clusters, brought about by the network's constant re-configuration. At $\lambda = 1.3$ arms continuously bind and unbind to each other allowing for arms to hop for one cluster to the other, eventually forming clusters with large populations. Conversely, for $\lambda = 1.6$, the unbinding of arms is less frequent due to the higher energy barrier, the larger clusters being the result of merging of smaller clusters, which makes it harder to form these large clusters. A detailed analysis of the reconfigurability of the network is presented in the next subsection. In the r -range between 5σ and 9σ (for $\alpha = 0.3$) or 7.5σ and 9σ (for $\alpha = 0.5$), a depletion of attractive monomers occurs, which is consistent with the arm length. Finally, at $r \cong 14\sigma$, a broad peak is observable, representing the inter-aggregate distance; this value is consistent with the diameter of the gyration of a star, $2R_g \cong 14\sigma$, which is to be expected.

To better quantify the long-range spatial correlations between the attractive aggregates, we make use of the structure factor $S(q)$, which can be obtained from the pair-correlation function via the following relation [65, 101]:

$$S(q) = 1 + \frac{N_a}{V} \int_0^{\infty} 4\pi r^2 [g(r) - 1] \frac{\sin(qr)}{qr} dr, \quad (4.2)$$

where q is the scattering wavenumber. The structure factor for both $\alpha = 0.3$ and $\alpha = 0.5$ at four representative values of λ , the same as those for the radial distribution function $g(r)$, is presented in Fig. 4.3(b). We observe that all the curves feature a peak at $q\sigma \approx 0.45$, confirming the existence of short-range liquid-like order in our system. The length scale $\ell \cong 2\pi/q \cong 14\sigma$ associated with this peak is of the order of the diameter of a star, and it expresses the typical inter-cluster separation obtained also with the function $g(r)$ above. For $\alpha = 0.5$, there is a second, longer-range length scale appearing marked by the peak at $q\sigma \approx 0.2$ for $\lambda = 1.3$. This peak signals the growth of larger-scale clusters through the merging of smaller ones at sufficiently strong attractions, and by increasing λ to 1.6, it moves to even lower $q\sigma$ which reaches the limit

4 SEMIDILUTE AND CONCENTRATED REGIMES

of what we can probe considering our chosen simulation volume. It can be considered for higher values of α as a precursor to macroscopic phase separation, $q \rightarrow 0$. At high values of q , we see a series of four peaks at $q\sigma \cong 7.5, 14, 19,$ and 22 show up, which also becomes more pronounced with an increase of λ . These peaks correspond to the close-packed structure of the attractive aggregates, i.e., they arise from the internal structure of the self-assembled clusters. Finally, the wavy structure that develops in the interval $q\sigma \in [0.6, 1.5]$ for the higher λ -values at $\alpha = 0.5$ comes from the scattering on the surface of the attractive aggregates. The slope of the decay of these oscillations is -4 , corresponding to Porod's Law for scattering from sharp (spherical) surfaces [102], whereas the locations of the oscillatory minima are consistent with the radius of the compact micelle-patches (i.e., 7σ for $\lambda = 1.3$ and 7.8σ for $\lambda = 1.6$). The structure is visible only on the curves with high λ -values and $\alpha = 0.5$, since only for this regime the patches are big enough to be approximately spherical. Above $q\sigma = 1.5$, the structures appearing have no physical significance, being just an artifact due to numerically performing the integration in Eq. (4.2). Overall, there is a striking similarity in both $g(r)$ and $S(q)$ with the corresponding results obtained for stiff, linear telechelic star polymers [65]. The pair correlation functions for $\phi = 0.1$ look very similar to the ones for $\phi = 0.06$, whereas at the very low concentration, $\phi = 0.01$, the individual chain structure of the SBC manifests itself in the distribution functions between the various types of monomers (not shown).

4.3.2 Patch and network characteristics

To gain more insight into the architecture of the networks, we look at the size distribution of the clusters in the network formed by the attractive parts of the arms, shown in Fig. 4.4. We define a cluster as the set of functionalized monomers that have to fulfill the criterion that any monomer in the cluster is placed at a maximum distance d from at least one other monomer in the cluster. Following this definition, all attractive monomers in an arm are part of the same cluster. Two monomers (and consequently two arms) do not need to have direct "contact" to be part of the same cluster but can be both at a distance lower than d to functionalized monomers of another arm or other arms that have contact to each other. We have chosen $d = 1.08\sigma$, which corresponds to approximately the distance where our attractive potential reaches half its minimum, for all the λ domain considered. Any choice of $d \in [r_c, r_{cut}]$ yields almost identical results.

The probability $P_{cs}(n_a)$ of finding a cluster containing n_a arms is calculated as $P_{cs}(n_a) = \mathcal{N}_{cs}(n_a)/\mathcal{N}_{cs}$, where $\mathcal{N}_{cs}(n_a)$ is the number of clusters containing n_a arms and $\mathcal{N}_{cs} = \sum_{n_a} \mathcal{N}_{cs}(n_a)$. Here we include also the case $n_a = 1$ in gathering statistics, to also account for single-arm clusters or *patches* formed by the self-association of terminal monomers of a single-arm without the participation of any other arm in the $n_a = 1$ -cluster.

For low attraction strengths, the distribution of cluster sizes is exponentially falling, most of

4 SEMIDILUTE AND CONCENTRATED REGIMES

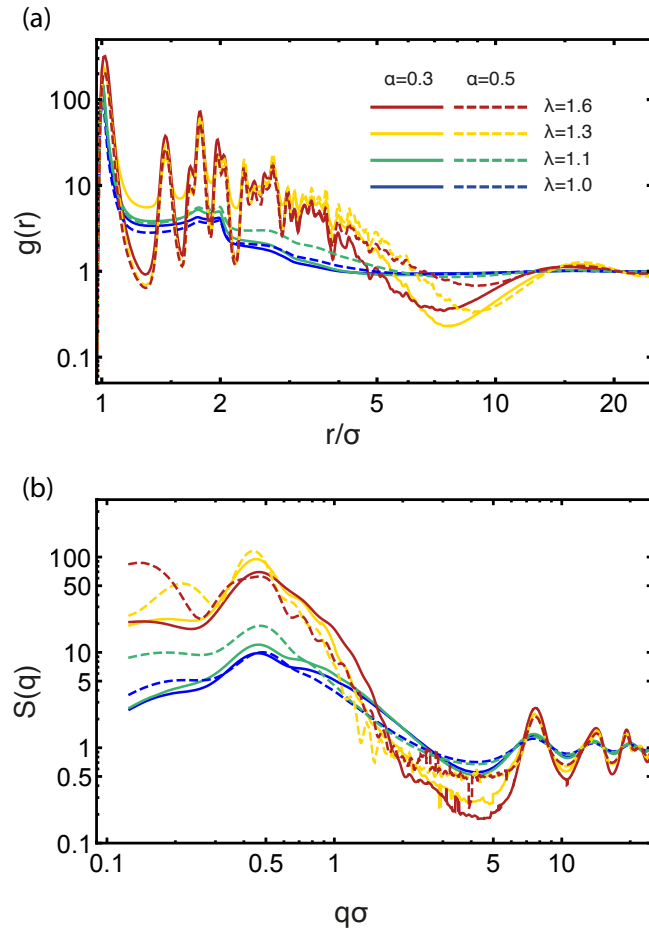


Figure 4.3. (a) Radial distribution function and (b) structure factor of the attractive monomers for different attraction strengths λ and attractive monomer fraction α . The color code for both plots is according to the legend in the panel (a). Data obtained by MD simulations at $\phi = 0.06$.

the arms being unbound, as seen in Fig. 4.4(a). By increasing either the attraction strength λ or the volume fraction ϕ , the average number of arms $\langle n_a \rangle$ contributing to a cluster also increases. The probability of occurrence of a cluster of a certain size starts to deviate from the exponential decay trend as λ and/or ϕ grow bigger.

Increasing the functionalization α has the same effect as increasing λ , i.e., more arms become bound and clusters grow bigger compared to systems with lower density. For values of λ that correspond to the transition regime from open star to dumbbells for the configurations of the single stars, we see the coexistence of free arms with clusters of various sizes, whereas for λ values for which dumbbells are fully assembled in isolation all arms are bound, see Fig. 4.4(c). In the

4 SEMIDILUTE AND CONCENTRATED REGIMES

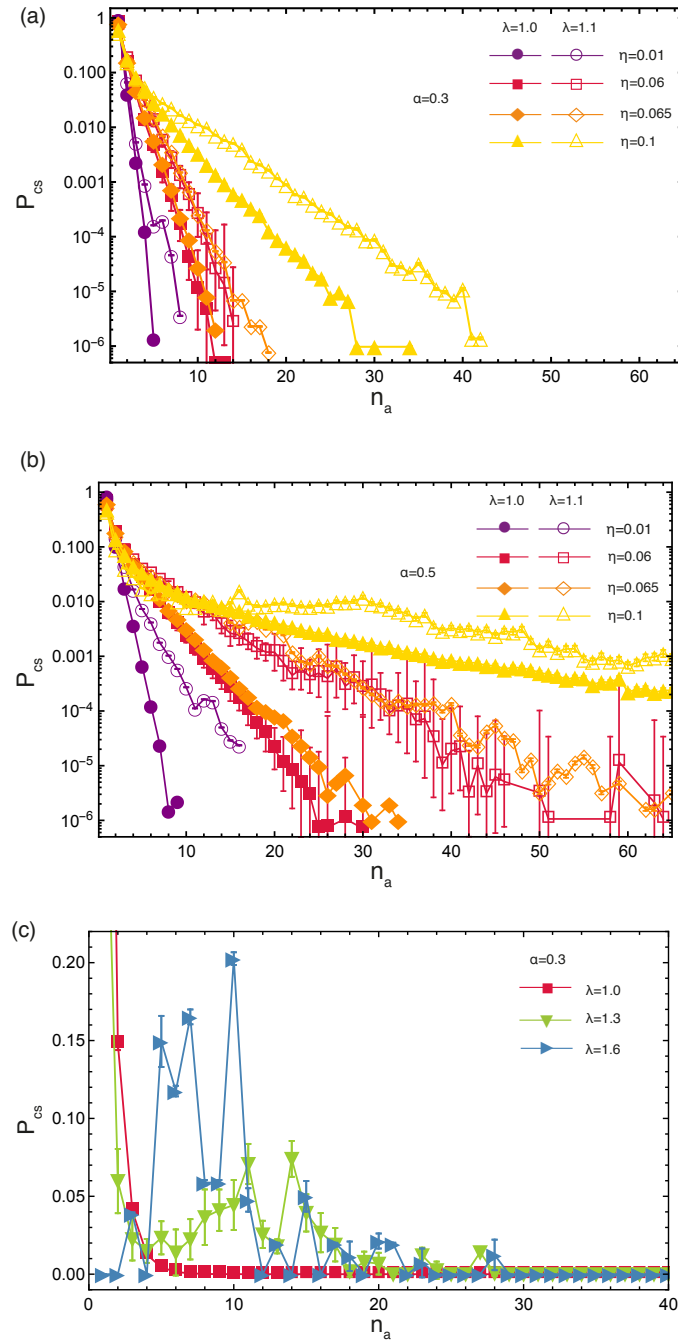


Figure 4.4. The patch size distribution $P_{cs}(n_a)$ as a function of the number of arms n_a that participate in each patch. Results for low attraction strength λ at different volume fractions, at $\alpha = 0.3$ [panel (a)] and $\alpha = 0.5$ for [panel (b)]. Data sets for $\phi = 0.06$ were obtained using MD whereas the other curves were obtained by hybrid MD-MPCD simulations. (c) Patch size distribution for $\phi = 0.06$ at different attraction strengths. The vertical axis has been cut to spotlight the peaks appearing for a high number of arms. Due to this truncation the points corresponding to $n_a = 1$ are not visible on two of the curves. The probability of these point is 0.79 ± 0.01 for $\lambda = 1.0$ and 0.4 ± 0.04 for $\lambda = 1.3$.

4 SEMIDILUTE AND CONCENTRATED REGIMES

latter regime, clusters containing $n_a \leq 10$ arms have higher occurrence probability than in the former one, where cluster with $n_a > 10$ arms are more frequent. This is due to the aforementioned possibility that arms detach from clusters and recombine into new ones, leading to the formation of big aggregates, which is present for $\lambda = 1.3$ but not for $\lambda = 1.6$ where the arms are tightly bound to their clusters and the barrier toward detachment and recombination are much higher.

We further draw the reader's attention to the fact that in the regime in which larger clusters start having non-negligible probabilities, such as the case of $(\alpha, \lambda) = (0.3, 1.3)$ shown in Fig. 4.4(c), the number of free arms or arms that participate in small clusters is much smaller than the ones in big clusters even if the probability of occurrence of these clusters is higher as a consequence of the chosen normalization. Finally, we point out that the results obtained using only Molecular Dynamics simulations and one obtained by the hybrid Molecular Dynamics-Multiparticle Collision Dynamics (MPCD) method, which explicitly takes into account the hydrodynamics of the solvent, is in excellent agreement with one another, as they should be for equilibrium properties. We therefore only focus, for the remainder of this section, on the intermediate volume fraction regime taking $\phi = 0.06$.

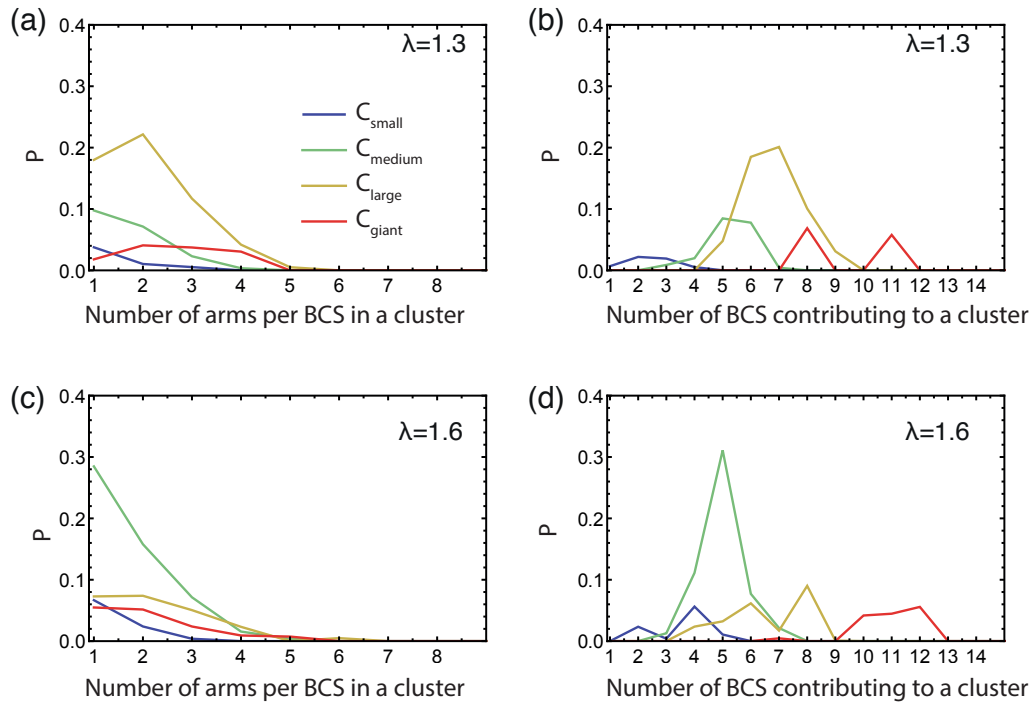


Figure 4.5. Normalized histograms of the number of arms that a SBC contributes to cluster [panels (a) and (c)] and of the number of SBCs contributing to a cluster [panels (b) and (d)]. All data presented are for $\alpha = 0.3$. For clarity, cluster sizes have been bundled into groups as follows: C_{small} for $2 \leq n_a \leq 5$; C_{medium} for $6 \leq n_a \leq 10$; C_{large} for $11 \leq n_a \leq 19$; and C_{giant} for $n_a \geq 20$.

4 SEMIDILUTE AND CONCENTRATED REGIMES

Contrary to hard, colloidal patchy particles [97] that carry a fixed pattern of attractive spots on their surface, block copolymer stars are soft and reconfigurable: the patchiness they feature as isolated particles at the infinite dilution limit, where only intra-star arm associations are possible, need not be the same as the one that results at finite concentrations where inter-star associations occur. For tetrahedrally-patched SBC, it has been found that the patchiness is robust concerning changes in the concentration [24, 54], but this is not too surprising since a tetrahedral patch arrangement has a sufficiently high degree of symmetry and it thus offers inter-star association possibilities also within an isotropic liquid. For self-assembling patchy particles that form dumbbells in isolation, as the SBC at hand, it is not *a priori* clear that the pattern of patchiness will be preserved also at finite concentrations. Accordingly, we need to determine whether the networks that we have let self-assemble are constructed having the single star configuration as building blocks or if there is a reconfiguration of these involved in the network construction. For this purpose, we count the number of arms that one star contributes to a cluster of a certain size as well as to the number of molecules that are contributing to a cluster for a particular size of clusters, all shown in Fig. 4.5. We normalize these histograms by the total number of arms and also choose to group the attractive aggregates by the number of arms participating in a cluster, into four size groups as follows: small clusters having $2 \leq n_a \leq 5$, medium clusters with $6 \leq n_a \leq 10$, large clusters $11 \leq n_a \leq 19$, and giant clusters of size $n_a \geq 20$.

We focus on the intermediate volume fraction regime taking $\phi = 0.06$. For low λ , since the vast majority of the clusters are very small, containing 2 or 3 arms, there are of course very few stars contributing to these aggregates, and, as expected, every SBC contributes with just one or at most two arms to an aggregate (data not shown). However, in the λ -region that corresponds to the transition from open stars to dumbbells for the isolated star, such as $\lambda = 1.3$ shown in Figs. 4.5(a) and 4.5(b), we find that the larger the clusters are, the more stars contribute to them. The number of arms a star puts into one cluster is always lower than 5, with the preferred size being 1 or 2 arms. By going to λ values at which dumbbells are formed in the very dilute regime, we would expect to find that each SBC contributes 4 or 5 arms to a cluster and consequently the number of SBCs contributing to such a cluster is 4 – 5 times lower than the cluster size. Surprisingly, we observe that, at $\lambda = 1.6$, the SBCs have an even stronger preference to contribute just 1 or 2 arms to a cluster, the 4 – 5-arm contributors being almost nonexistent, see Fig. 4.5(c). Furthermore, there is a significant number of stars per cluster, approximately 5, as seen in Fig. 4.5(d). These findings demonstrate that each star contributes with a low number of arms to multiple clusters, thus leading us to the conclusion that stars in the network must be geometrically/conformationally different than the isolated ones. This implies that there must be a significant reconfiguration of the SBCs forming the network compared to their one-star conformation. In particular, the stars assume an isotropic configuration akin to the non-functionalized molecules for $\lambda = 0$, reducing thereby the entropic penalty they would have to pay for having a dumbbell shape; the energetic gain from

4 SEMIDILUTE AND CONCENTRATED REGIMES

inter-arm associations is now offered by the neighboring stars present in the concentrated solution.

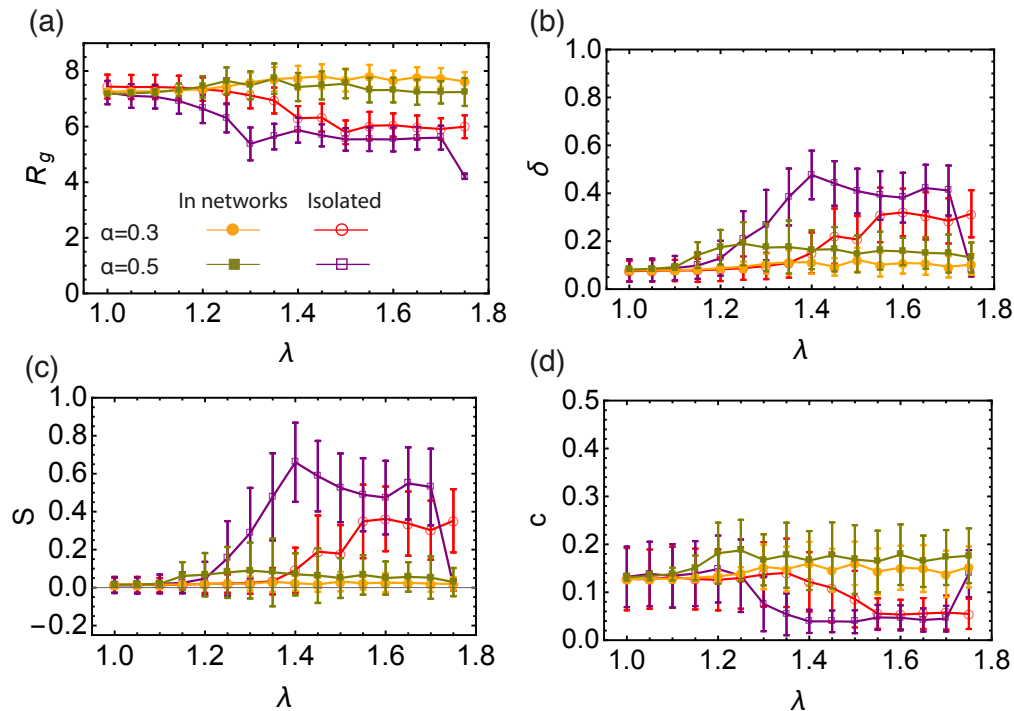


Figure 4.6. Size- and shape-characteristics of SBCs in isolation and in the networks and for different fractions of attractive monomers, as indicated in the legend. (a): gyration radius R_g ; (b): asphericity δ ; (c): prolateness S ; (d): acylindricity c .

Further corroboration for the reconfigurable nature of the SBC is offered by an analysis of the geometrical characteristics of the stars in isolation versus the ones that are part of a network. For this purpose, we employ shape parameters computed starting from the gyration tensor and the results are presented in Fig. 4.6. For isolated stars, we find that the gyration radius R_g , shown in Fig. 4.6(a), decreases in the transition region toward a dumbbell-shape compared to the open star configuration. This is consistent with some of the arms self-assembling into small clusters, hence reducing the size of the object. The star becomes also less spherical due to intra-star assembly, as can be seen from increased asphericity δ in Fig. 4.6(b). As dumbbell structures are formed, the radius of gyration further decreases, and the star assumes an increasingly prolate shape $S > 0$, shown in Fig. 4.6(c) as well as a decreased acylindricity, Fig. 4.6(d). For $\alpha = 0.5$ the trend is the same, two differences being worth noting: first, for $\lambda = 1.3$ we see a sharp decrease in R_g , the value being lower than the one for the dumbbells. For these parameters, the star assembles first into 3 patches, which accounts for this difference. For $\lambda = 1.75$, the attraction strength becomes strong enough to overcome the entropic contribution of the non-functionalized part of the arms, and the star assembles into a collapsed, watermelon structure [85], characterized by a small gyration

4 SEMIDILUTE AND CONCENTRATED REGIMES

radius and high sphericity. On the other hand, the shape of the stars that form the networks do not follow the isolated star trends. The SBCs in the network have a morphology similar to the open star configuration and their geometrical characteristics are essentially independent of λ . They are highly spherical and have a similar gyration radius as the open stars throughout the λ interval considered. The gyration radius is somewhat smaller for $\alpha = 0.5$ compared to $\alpha = 0.3$ since in the former case, more attractive beads are available to form clusters which are highly packed objects. Based on the measured gyration radius, we estimate the degree of swelling of stars in the network to be of the order 10. These findings, together with the detailed analysis of the attractive aggregates, show that SBCs in networks are not just self-assembled stars that are further bound together but rather each star contributes to multiple attractive aggregates homogeneously distributed around the star. SBCs are not pre-configured units that further self-assemble into larger structures as concentration grows but rather reconfigurable objects that organize themselves into homogeneous networks with well-dispersed inter-star association sites. The reconfiguration of these dumbbell-forming molecules in concentrated solutions is at odds with the behavior of higher-functionality telechelic stars, which form tetrahedrally coordinated soft patchy nanoparticles that are robust in their shape also at high concentrations, at least for temperatures as low as the Θ -temperature of the solvophobic end-blocks [24].

To explore the connectivity of the network, we now focus on the full SBC network, not only on the patches formed by the attractive part of the arms. We look at the number of components present in the network, defining a component as all-stars that are connected through a cluster formed by the attractive ends of the arms. To belong to a component, a star only needs to be bound to one other SBC in the same component. We count, at a given α and λ , the average number of components, shown in Fig. 4.7(a), the average number of stars that contributes to a component, Fig. 4.7(b), the average number of stars contributing to the biggest component in the system, Fig. 4.7(c), and the average number of free SBCs that have no connections at all (called free stars), Fig. 4.7(d). For most of the values of α and λ considered we find that (see Fig. 4.7) all-stars are connected among themselves: there is just one component in the network, the number of the star in this component is $N_s = 52$, which equals the total number of SBCs in the simulation volume, and there are no free stars. For the lowest values of λ considered (at $\alpha = 0.3$) the system appears to contain multiple components. However, by observing the size of the bigger component in the system and the number of free SBCs, we conclude that our systems consist of one very large component containing almost all the stars available in the simulation volume and a couple of free stars.

Related to the above considerations is the question of whether the networks that have assembled are still reconfigurable: can arms leave one aggregate and re-attach to another one allowing for configuration changes in the networks? Furthermore, it is pertinent to know whether the stars are still mobile, i.e., free to diffuse. To evaluate the mobility of the stars we compute the mean

4 SEMIDILUTE AND CONCENTRATED REGIMES

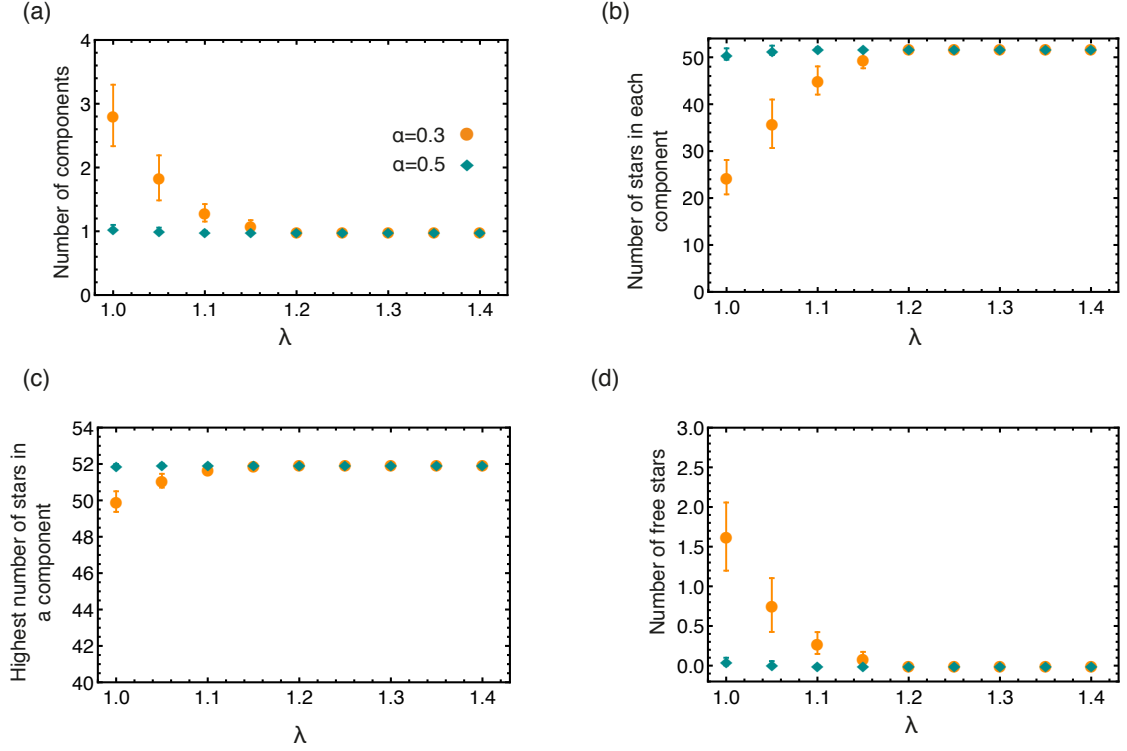


Figure 4.7. Characteristics of network connectivity. (a): the average number of components; (b): the average number of stars in each component; (c): the average number of SBCs forming the biggest component; and (d): the average number of free stars, as a function of the attraction strength λ for the two values of α considered.

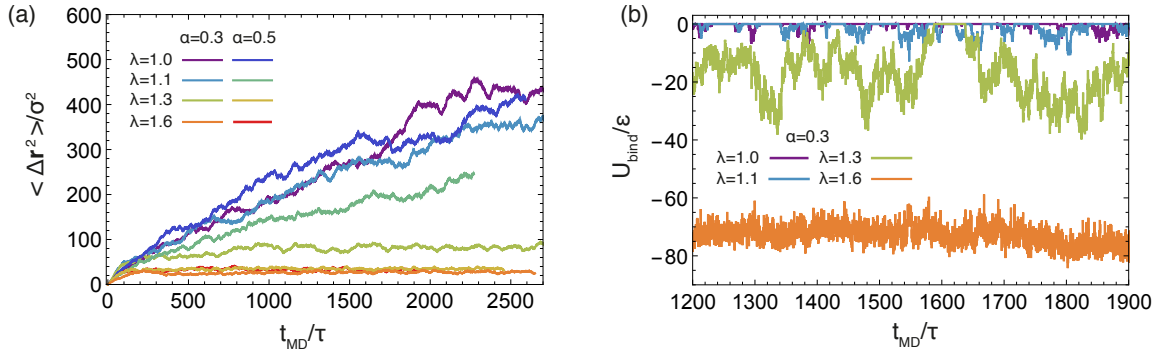


Figure 4.8. (a) The mean squared displacement of the star cores in the network for different values of α and λ , as indicated in the legend. (b) The binding energy per arm, U_{bind} , defined as the interaction energy of the terminal monomers of one star arm with terminal monomers of other arms for $\alpha = 0.3$ and λ -values as indicated in the legend. On the horizontal axis, the label t_{MD} denotes time, in Molecular Dynamics units $\tau = 500\Delta t$, where Δt is the MD time step (see Methods).

4 SEMIDILUTE AND CONCENTRATED REGIMES

squared displacement of the anchoring point (centers) of the stars as:

$$\langle \Delta \mathbf{r}^2(t) \rangle = \frac{1}{N_s} \left\langle \sum_{i=1}^{N_s} (\mathbf{r}_i(t) - \mathbf{r}_i(0))^2 \right\rangle, \quad (4.3)$$

where the sum runs over all the centers \mathbf{r}_i of the N_s stars in the system and t denotes time. For the lower values of λ ($\lambda = 1.0$ and $\lambda = 1.1$), for both α 's considered, the stars diffuse and explore the entire simulation volume, see Fig. 4.8(a), consistent with the finding in [56]. In other words, although they are all connected within a single component, as found above, the bindings of the arms to the associated sites are transient and thus each star frequently detaches and forms new connections, walking in this way across the entire system. The diffusivity decreases for a given α as λ grows as well as for a given λ as α grows. On the other hand, for the higher λ values, the SBCs are caged inside a small region, forming an arrested gel, and the mean-square displacement saturates at values below the size of an individual star, with the cage size shrinking at stronger attractions.

Our analysis up to now has been exclusively for the intermediate-functionality case, $f = 9$. To provide a brief comparison with the low-functionality case, we have performed simulations at the same star density, $\phi/\phi_* \cong 0.6$, and λ -values, for SBC of functionality $f = 4$ and fractions of attractive monomers $\alpha = 0.3$ and $\alpha = 0.5$; representative results are shown in Fig. 4.9. We found very different connectivity characteristics between the two functionalities for identical λ -conditions, which physically correspond to a fixed temperature. For small λ -values, the $f = 4$ -stars do not form any kind of network, a significant fraction of them being free of connections to other ones. The values of λ for which a percolating network is observed are much higher than for the case of $f = 9$. The two resulting networks have very different morphologies. For $f = 9$, we found a homogenous-looking network with patches connected by several arms, whereas for $f = 4$ we observe regions where patches and their contributing stars alternate with voids, as seen in Fig. 4.9(a). In other words, in the second case, we have micellar patches formed by many stars and a few arms of the latter connect the micelles, leaving at the same time large regions that are populated by stars that share their arms between different micelles. As these regions contain also lots of empty space, the cages that they form are larger than those of the $f = 9$ -stars. Concomitantly, in the resulting arrested networks, the size of the cage in which the anchor is trapped is approximately twice as big for $f = 4$ in comparison to $f = 9$. This can be clearly seen in Fig. 4.9(b) in comparing the height of the MSD-plateau, $\ell_\infty \equiv \sqrt{\langle \Delta \mathbf{r}^2(t \rightarrow \infty) \rangle}$, there, with the corresponding value for $f = 9$ from Fig. 4.8(a). Indeed, for $f = 4$, $\lambda = 1.6$ and $\alpha = 0.3$, we obtain $\ell_\infty^2 \cong 100$, whereas for $f = 9$ and identical λ - and α -values, a plateau-value of $\ell_\infty^2 \cong 25$ results, showing the much stronger confinement of the latter stars in their cages.

Recently, Metri et al. [81] investigated a system of network-forming telechelic star polymers that bears certain similarities, but also important differences, with the systems we examine here.

4 SEMIDILUTE AND CONCENTRATED REGIMES

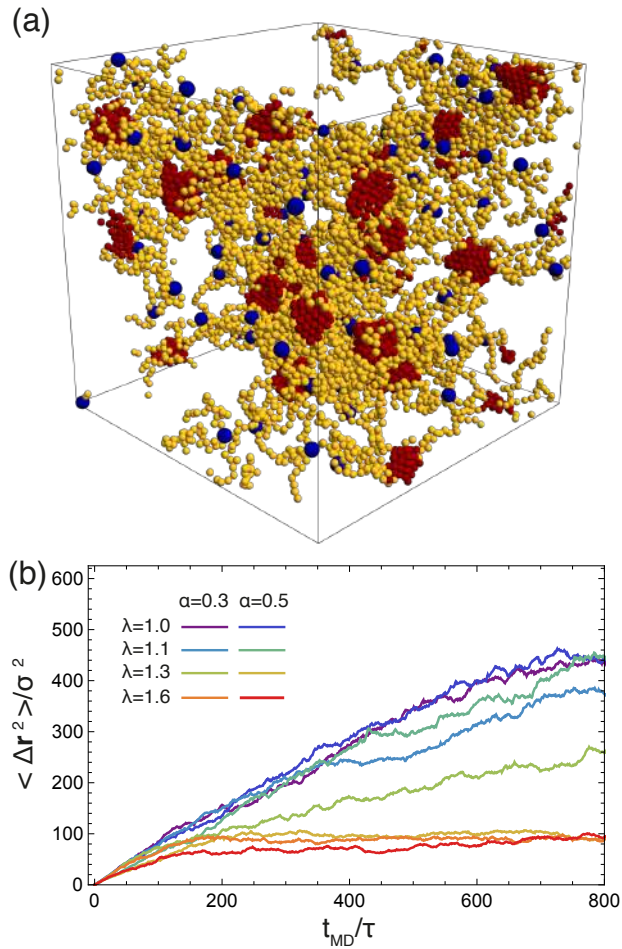


Figure 4.9. BSCs with lower functionality ($f = 4$): (a) Snapshot of network formed at $\alpha = 0.3$ and $\lambda = 1.35$. (b) The mean squared displacement of the star cores in the network for different values of α and λ , as indicated in the legend. For details about the quantities on the horizontal axis we refer to Fig. 4.8.

The experimental system consisted of a cross-linked glycol diacrylate core with an average of $f = 13$ attached arms made of poly(*n*-butyl acrylate); at the tip, each arm was functionalized with three bis(2-methacryloyloxyethyl) disulfide stickers, playing a role analogous to the terminal B-monomers of our system. Contrary to our solvophobic beads, however, the stickers can form a connection to other stickers only once but since each arm carries at its end a sticker with three ‘fingers’, intra- or inter-star association sites with more than two participating arms are still possible. On the other hand, the attractions for the system of Metri et al. [81] are so strong that the associations are considered to be irreversible. Accordingly, in the coarse-grained simulations employed there, a certain fraction of stickers, p_{ext} , is attached to external stickers from other stars in a quenched, i.e., pre-determined (albeit randomly selected) fashion. Also, the simulation technique

4 SEMIDILUTE AND CONCENTRATED REGIMES

employed there is a different, hybrid one, employing Rouse dynamics for the chains and effective potential for the cores [103], to accelerate the dynamics to cover a broad range of time scales, reach up to $\sim 10^5$ s. Despite these differences, striking similarities with the findings for the systems at hand arise: at a cross-linking fraction $p_{\text{ext}} \cong 0.25$ of stickers, the mean-square displacements of the cores show a plateau, which broadens further for higher values of this parameter, in full analogy with our findings in Fig. 4.8(a), where the role of the control parameter is now played by the attraction strength λ . This dynamical arrest is accompanied by a long-time plateau of the stress relaxation $G(t)$, signaling the presence of extremely long relaxation processes in the system and the transition to an amorphous rheological solid. Although we have not performed measurements of the stress relaxation (or the viscosity) in this chapter, and additional coarse-graining would be required also here to reach long-time scales, it is justified to expect that systems that are fully connected and the arms have very large and negative inter-star binding energies such as those shown in Fig. 4.8(b), will also have the typical rheological response of a solid.

Finally, to probe the fluctuations of the arms of the stars, we focus now on $\alpha = 0.3$ and look at the values of the sum of the attractive potentials of all the beads in an arm, U_{bind} , over the course of our simulations. We have excluded from U_{bind} the contribution arising from same-arm monomers, since we are interested in the interaction with other arms, and thus the participation in the formation of attractive aggregates, and not in the intra-arm self-assembly. The quantity computed in this way vanishes for free arms and takes negative values for an arm that is attached (bound) to at least one another arm. Results for different values of λ for one single representative arm are presented in Fig. 4.8(b). For $\lambda = 1.0$ and 1.1 , the arm frequently attaches and leaves an aggregate. For the case of $\lambda = 1.3$ arms tend to spend more time in a bounded state but they also unbind, allowing for reconfigurations, and the quantity U_{bind} features very strong fluctuations. At $\lambda = 1.6$, and consistently with the existence of an arrested network, the energy barrier to unbind becomes too high and the arms spend their entire time in a bound state, reconfiguration of the network is possible only by cluster merging.

4.4 Dynamical Properties

4.4.1 General behavior under shear

We begin our discussion by describing the behavior of our SBC system at different amphiphilicity α and volume fractions ϕ as a function of the shear rate $\dot{\gamma}$. At $\alpha = 0.3$, for the lowest monomer fraction ($\phi = 0.01$) and the lower shear rates considered ($\dot{\gamma} \tau \lesssim 0.001$), there are no effects of the flow observed (see the upper left panels of Fig. 4.10), neither at the level of the single stars (i.e., the shape of the stars appears, at least by eye, to be the same as in equilibrium), nor at the level of inter-star aggregates (i.e. the average number of SBCs that are connected does not seem

4 SEMIDILUTE AND CONCENTRATED REGIMES

to change, even if arms unbind and rebind continuously). At $\dot{\gamma}\tau = 0.001$, we start being able to distinguish stars flowing along the field. The stars still do not change shape appreciably and each inter-star cluster flows with constant velocity, keeping its equilibrium morphology. For $\dot{\gamma}\tau = 0.004$ ($Wi \approx 30$), we begin to observe elongations at the level of single stars along the flow direction, combined with the flattening of the star shape in the xz -plane that becomes more visible as $\dot{\gamma}$ increases. The star clusters also start to change shape, with their elongation also being in the flow direction. Above $\dot{\gamma}\tau = 0.02$ shear banding can be seen, as shown in the upper right panels of Fig. 4.10.

At the intermediate volume fraction $\phi = 0.06$, the percolating network that characterizes our system in equilibrium is, as in the case of the lower monomer fraction, largely undisturbed when low shear rates are applied (Fig. 4.10, middle row). As the shear rate increases, the size of the attractive aggregates built by different arms coming together starts to decline since arms are being pulled out from the aggregates by the flow. Similarly to the system at low density, for $\dot{\gamma}\tau \gtrsim 0.004$, we observe a stretching of the polymers, accompanied by an elongation of the attractive aggregates. The network appears to percolate for all $\dot{\gamma}$ values considered in this study. The most dense system analyzed ($\phi = 0.1$) shows a similar behavior than the one at $\phi = 0.06$, with the difference that here the attractive aggregates stretch already at a lower shear rate ($\dot{\gamma}\tau = 0.01$, compared to $\dot{\gamma}\tau = 0.02$), as shown in the top panels of Fig. 4.10.

For the case $\alpha = 0.5$, the behavior is similar to the corresponding system at lower α , with the particularity that here we observe ruptures of the network, i.e., our initially percolating systems ($\phi = 0.06$ and $\phi = 0.1$) break down into multiple disconnected sub-components. This phenomena is due to the topology of the network in equilibrium: the systems at this attractive monomer fraction has big free voids inside the network. Then, as shear is applied, the places of the network where the network is weaker, i.e., where the inter-star connections are minimal being formed by just one arm coming from each star, will break apart.

4.4.2 Geometrical properties

The first finding to point out regarding the shape parameters is that the volume fraction of monomers has an effect on the gyration radius (*chapter 2* in *sec. 2.3.1.a*) even for low shear rates: the SBCs that are part of denser systems increase by a larger proportion relative to their equilibrium configuration, see Fig. 4.11(a). This is a consequence of the fact that, for $\phi = 0.06$ and $\phi = 0.1$, the SBCs form a percolating network, and even a small deformation of system leads to extension of the individual stars. At $\phi = 0.01$, where the inter-star interaction is reduced, the relative size of the stars is around the same as for single star. At low shear rates, the asphericity δ is higher for stars with $\alpha = 0.5$ than for these with $\alpha = 0.3$ (data not shown), because the stars with more functionalized monomers form more asymmetric structures, i.e., a higher number of B-monomers

4 SEMIDILUTE AND CONCENTRATED REGIMES

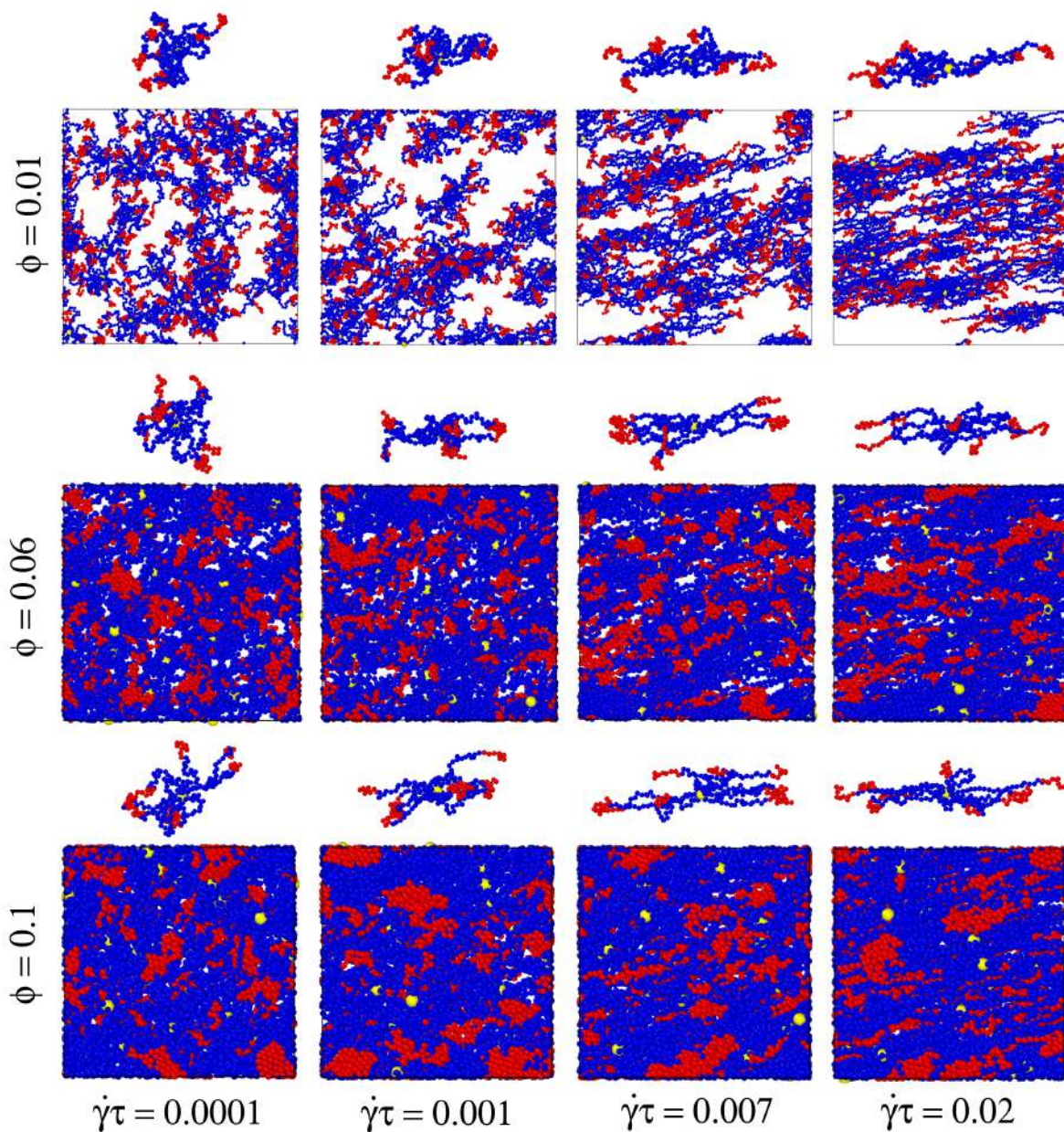


Figure 4.10. Snapshots from simulation for SBC solutions with $\alpha = 0.3$ at different volume fractions ϕ and shear rates. The solvophilic monomers are shown in blue, and the solvophobic monomers in red, and the anchors in yellow. Above each image, one star selected at random has been shown separately to make the typical shape of a SBC visible. The number of stars in all boxes is the same but the boxes have different sizes according to the density, therefore the stars at lower densities appear smaller in the snapshots. The snapshots of the single stars are all drawn at the same scale to facilitate shape and size comparisons.

are localized in the attractive aggregates. As the shear rate increases, the curves for both values of α collapse. This is an indication of the unfolding of the attractive aggregates. The prolateness

4 SEMIDILUTE AND CONCENTRATED REGIMES

S goes up with $\dot{\gamma}$ whereas the acylndricity c decreases, see Figures 4.11(b) and 4.11(c), which is consistent with the observation that the SBC stretch, having a more cigar-like shape as the system is sheared. Both of these shape parameters also display collapse of different α -systems at high $\dot{\gamma}$, consistent with a fully elongated polymeric star. The higher the density the more elongated the stars become due to the inter-star connections that have to be accommodated in addition to the flow.

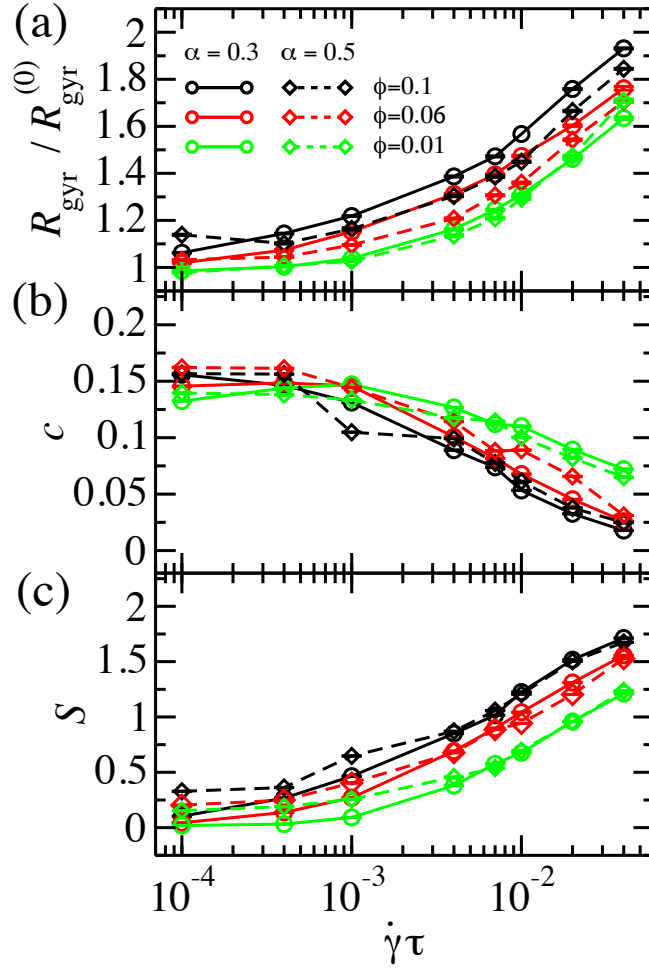


Figure 4.11. Global shape parameters of SBCs as a function shear rate for different concentrations and amphiphilicities: (a) normalized gyration radius $R_{\text{gyr}}/R_{\text{gyr}}^{(0)}$, (b) acylndricity c , and (c) prolateness S . The value $R_{\text{gyr}}^{(0)}$ denotes the gyration radius of an isolated SBC at equilibrium.

To obtain more information on the deformations of the SBCs with respect to the spatial directions, we analyze the diagonal components $G_{\mu\mu} = \langle G_{\mu\mu} \rangle$ of the gyration tensor (*chapter 2* in *sec. 2.3.1.a*) normalized to the value of isolated SBC at equilibrium, $G_{\mu\mu}^{(0)}$, as shown in Figures 4.12(a)-4.12(c). At $\phi = 0.01$ the system shows a behavior similar to that of isolated stars [83]: for low shear rates ($\dot{\gamma}\tau < 4 \times 10^{-4}$) no strong deformation appears; as $\dot{\gamma}$ increases, both

4 SEMIDILUTE AND CONCENTRATED REGIMES

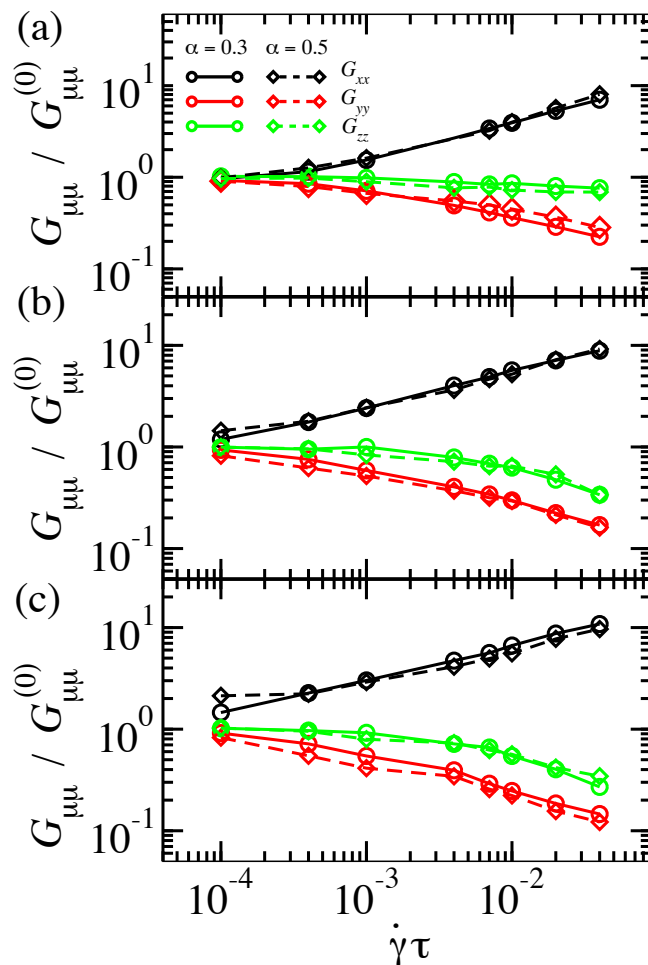


Figure 4.12. Normalized diagonal components of the gyration tensor $G_{\mu\mu}/G_{\mu\mu}^{(0)}$ as a function of the shear rate at different monomer volume fractions: (a) $\phi = 0.01$, (b) $\phi = 0.06$, and (c) $\phi = 0.1$. The quantities $G_{\mu\mu}^{(0)}$ are the averaged diagonal components of \mathbb{G} for an isolated SBC at equilibrium.

monotonically increasing G_{xx} and diminishing G_{yy} are found, reaching a difference of almost one order of magnitude with respect to $G_{\mu\mu}^{(0)}$ at the highest $\dot{\gamma}$ probed; meanwhile G_{zz} decreases only slightly. This indicates that the extension of the SBCs occurs along the flow direction (x -direction). While its size is drastically decreased in the the gradient direction (y -direction), the relative shrinkage in the vorticity direction is comparatively small, hinting at a flattened elliptical shape of the SBC located in the xy -plane. As mentioned above, for the higher concentrations, spatial inhomogeneities in the shape of the SBCs with respect to the isolated case are observed even at $\dot{\gamma}\tau = 10^{-4}$ and, at higher shear rate, even lower values for G_{yy} and G_{zz} are found, which points out to a more rod-like shape of the SBCs. It is to be noted that, for each density, the corresponding curves for $\alpha = 0.3$ and $\alpha = 0.5$ collapse at high shear rate.

Further insights on the positioning of the SBC with respect to the flow can be gained by con-

4 SEMIDILUTE AND CONCENTRATED REGIMES

Considering the orientational resistance m_G Eq. 3.1 This parameter measures the average alignment of the SBC induced by the flow. As displayed in Fig. 4.13(a), the orientation resistance increases with $\dot{\gamma}$. For the two higher densities, we observe a reasonably fair overlap of the curves, while the dilute system features a higher orientational resistance than the denser counterparts. This phenomenon can be again explained by the larger connectivity of the denser system. There, the alignment along the flow direction is further enhanced and also stabilized through the connection of attractive B-monomers at the end of each arm with abundant neighboring ones from the other SBCs.

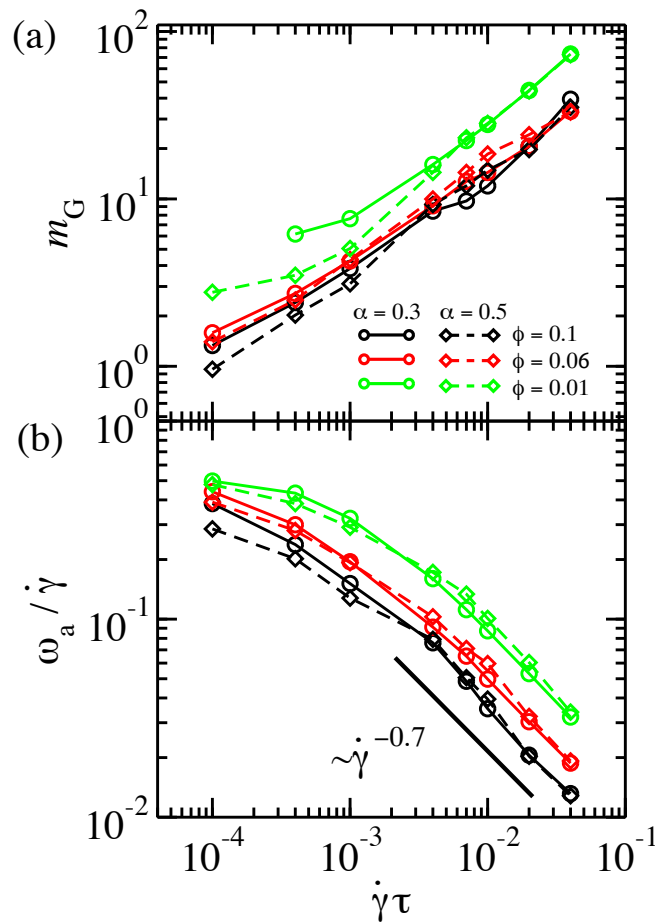


Figure 4.13. (a) Orientational resistance and (b) apparent angular velocity as a function of shear rate.

Furthermore, to understand the dynamics of the stars, we can make use of the angular velocity (see section 3.5.4) Eq. (3.25). For isolated SBC, it can be interpreted either as the tumbling frequency of a rigid body in the shear flow, which shape is similar to the average shape of the SBC, or as the frequency at which the individual arms rotate by tank-treading around the geometrical star center [67].

4 SEMIDILUTE AND CONCENTRATED REGIMES

As can be seen in Fig. 4.13(b), the ratio between the angular velocity and the shear rate ($\omega_a/\dot{\gamma}$) decreases as the latter increases, which is due to the flexibility of the SBC: for a rigid object we expect to have $\omega_a/\dot{\gamma}$ constant, whereas here clearly $\omega_a/\dot{\gamma} \propto \dot{\gamma}^{-a}$, with $a \simeq 0.7$ for the larger shear rate probed. Also, we observe that lower densities allow for higher ω_a since stars exhibit less steric hindrance from neighbors and also are less likely to break free from inter-star connection and tumble since they have fewer of these connections per star.

4.4.3 Radial correlation functions

In order to analyze the microscopic conformation of the system, we use radial pair-correlation functions for the different monomer species. In particular, it allows us to gain additional information about the structure of the attractive patches. The pair-correlation function $g_{IJ}(r)$, which assesses the probability of finding a monomer of species I at a distance r from a monomer of species J , is defined as

$$g_{IJ}(r) = \frac{V}{\hat{N}_I \hat{N}_J} \left\langle \sum_{i=1}^{\hat{N}_I} \sum_{j=1}^{\hat{N}_J} \delta(\mathbf{r} - \mathbf{r}_{ij}) \right\rangle, \quad (4.4)$$

where $r = |\mathbf{r}_{ij}|$ denotes the distance between the i -th and the j -th monomers [98, 104]. The sub-indexes I and J can take any of the values A for non-interacting monomers, B for functionalized ones, and C for anchors. For g_{II} the terms with $i = j$ are excluded from the sum. The normalization constants \hat{N}_A represent the total number of A monomers in the system ($\hat{N}_A = N_s f N_A$), \hat{N}_B is the number of functionalized monomers ($\hat{N}_B = N_s f N_B$), whereas $\hat{N}_C = N_s$ is the number of anchors.

We first turn our attention to the pair correlation function $g_{AA}(r)$ between the non-functionalized parts of the SBC as presented in Fig. 4.14. At $\alpha = 0.3$ and low share rates, we observe no significant difference to the equilibrium behavior for very dilute system ($\phi = 0.01$), i.e., the radial pair correlation function exhibits a first peak at $r/\sigma \simeq 1$ which corresponds to the first order neighbors along the chain, followed by a much less pronounced one at $r/\sigma \simeq 2$, see Fig. 4.14(a). By increasing the shear rate, an increase in these two peaks takes place. At $\dot{\gamma} \tau = 0.04$, we start seeing regular peaks at approximately integer values of r/σ . These are evidence of the stretching of the polymers along the flow, forming an ordered structure. The same stretching feature of the A-blocks of the arms is also observed in the g_{CA} correlation function (data not shown). Moreover, the depleted region observed at $r/\sigma \approx 14$ corresponds to the typical size of stars and disappears with the increase in $\dot{\gamma}$ due to the homogenization of the system. The higher density systems show the same features as the one at $\phi = 0.01$, with the peaks being more pronounced, which is consistent with the increase in the monomer local density. The systems with $\alpha = 0.5$ shows similar features, but the peaks of $g_{AA}(r)$ at short distance tend to have higher values since the SBC have better formed patches meaning that the arms are placed closer together. The regular structure at high $\dot{\gamma}$ vanishes at lower

4 SEMIDILUTE AND CONCENTRATED REGIMES

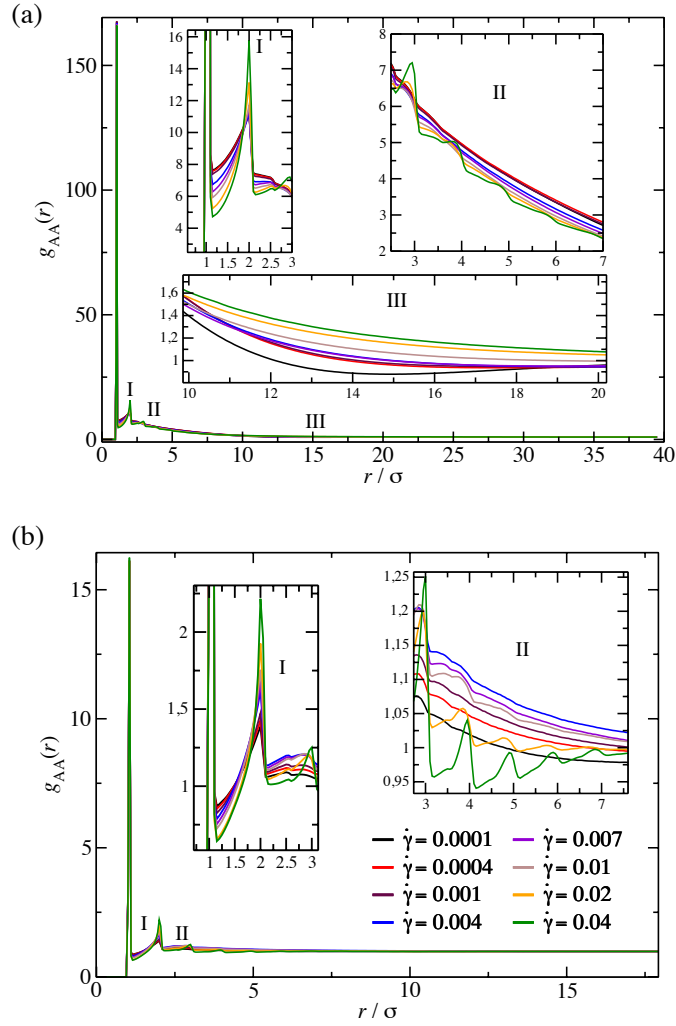


Figure 4.14. Radial correlation function of A-monomers for (a) $\phi = 0.01$ and (b) $\phi = 0.1$. Insets show enlarged zones of the curves for different radial distance. The data presented in both panels correspond to $\alpha = 0.3$.

r/σ since the non-interacting part of the arms is shorter at $\alpha = 0.5$.

On the other hand, the correlation function (g_{BB}) for the attractive monomers shows a much more structured profile as shown in Fig. 4.15(a). The locations of the correlation peaks are consistent with a random hexagonal close-packed structure. This arrangement has also been observed in equilibrium and is a direct consequence of the short-range attractive interaction between B-monomers. At low density, these peaks decrease in height significantly for $r/\sigma > 2$, which is concomitant with the average size of the observed clusters. For $\phi = 0.06$ and $\phi = 0.1$, the peaks are observable up to a distance $r \sim 8\sigma$ and decrease in size as the shear rate increases. At the highest shear rate analyzed, $\dot{\gamma}\tau = 0.04$, the peaks at $r/\sigma > 4$ and $r/\sigma > 7$ for $\alpha = 0.3$ and $\alpha = 0.5$,

4 SEMIDILUTE AND CONCENTRATED REGIMES

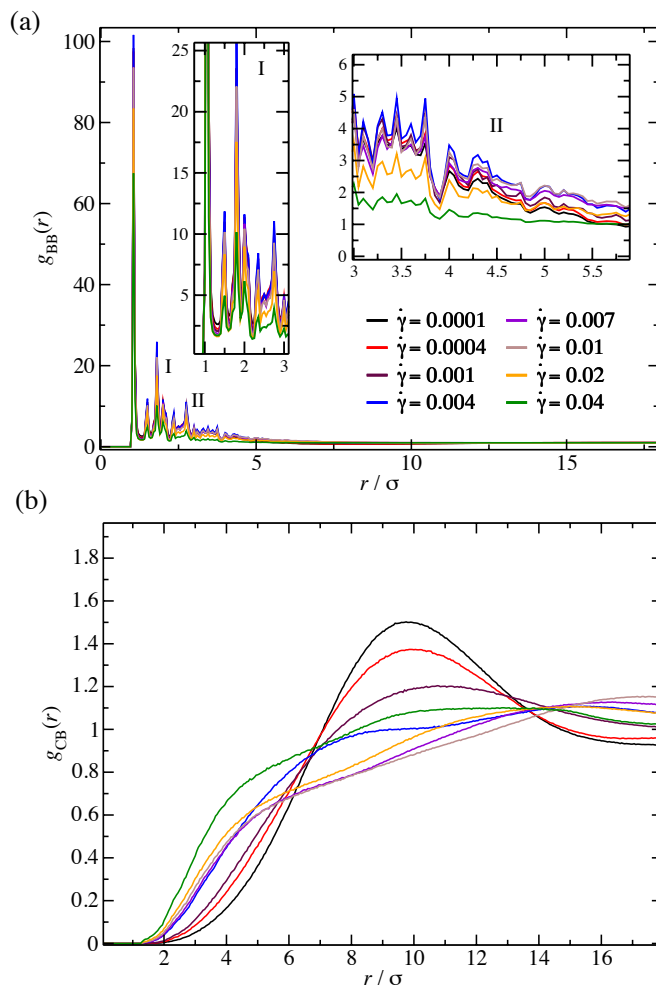


Figure 4.15. Radial correlation function for (a) B–B and (b) C–B monomer pairs. Insets in panel (a) show enlarged zones of the curves for different radial distance. For both panels $\alpha = 0.3$ and $\phi = 0.1$.

respectively, vanish. Similarly, as the shear rate increases, lower peaks are observed suggesting that the size of the attractive aggregates decreases as the system is sheared as consequence of the detachment from the cluster of some arms.

By looking at the pair-correlation function between non-interacting and functionalized monomers (g_{AB}), we notice significant peaks only at $r/\sigma \simeq 1$ and $r/\sigma \simeq 2$ at zero shear. At high shear rates, g_{AB} develops a profile with multiple peaks located at integer values of r/σ , this again being an indication of the chain stretching (data not shown).

The stretching is also supported by the anchor-functionalized monomers correlation function g_{CB} shown in Fig. 4.15(b). As can be seen there, the equilibrium g_{CB} shows a well defined peak around $r/\sigma \simeq 8$ to 10 depending on ϕ . This distribution flattens out as shear increases, leading

4 SEMIDILUTE AND CONCENTRATED REGIMES

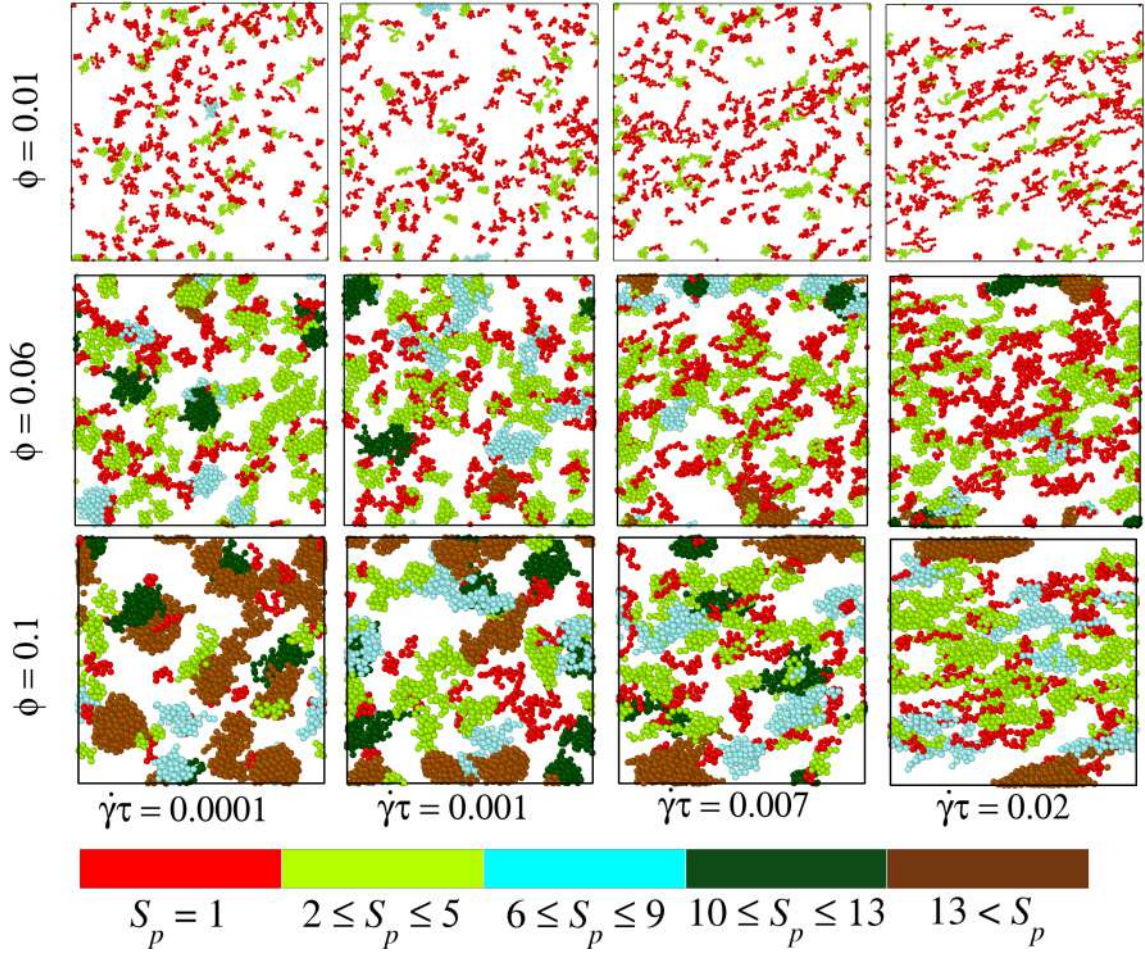


Figure 4.16. Graphical representation of the patch sizes behavior for $\alpha = 0.3$ and different density (ϕ) and shear rate. Here, only B-monomers are displayed. Each color categorize the size S_p of the patches: red is used for free arms ($S_p = 1$), green for $2 \leq S_p \leq 5$, light blue for $6 \leq S_p \leq 9$, dark green for $10 \leq S_p \leq 13$, and brown for $13 < S_p$.

to an increasing value at shorter r , because the induced elongation of the arms B-block. Since the SBCs align with the flow, new space is open which can be occupied by another stars. A similar phenomena is also seen in the anchor-anchor correlation function g_{CC} , where anchors are allowed to come closer as the shear increases.

4.4.4 Patches behavior

In the previous section, we presented results regarding the global conformation properties of the systems under consideration. Now, we turn our attention to the effect of shear on the features of the formed attractive aggregates (patches), in particular, to the number of patches in the system (N_p) and their size (S_p), i.e., the number of arms clustered in each patch.

At this point, it is important to note that the average configuration of isolated SBCs at equilib-

4 SEMIDILUTE AND CONCENTRATED REGIMES

rium that we found, features the coexistence of free arms and patches. This behavior is different from the fully self-assembled scenario, i.e., no presence of free arms, described in [23], for similar parameters (f , α and λ). This difference is a consequence of the large arm polymerization degrees employed there ($N > 120$) in comparison to the much shorter arms ($N = 30$) we consider here, which in turn leads to a higher steric penalty when forming patches. In fact, the SBCs considered here become fully self-assembled as λ increases

In this way, at low density a large fraction of the arms are free since potential binding partners are spatially far away whereas at higher densities more arms are bound, leading to the increase of the size S_p of the equilibrium clusters. Aiming to visualize the changes in cluster size due to different parameters, we divided the clusters into five size categories: free arm, small clusters involving 2–5 arms, medium clusters which are composed of 6 to 9 arms, large clusters with 10 to 13 arms, and giant clusters containing more than 13 arms. Each category is assigned a different color in Fig. 4.16.

For low density ($\phi = 0.01$) and $\dot{\gamma}\tau \leq 0.007$, the cluster size does not drastically change, the system has mostly free arm, a population of small clusters, and few medium-sized ones, whereas at $\dot{\gamma}\tau = 0.02$ the medium-sized clusters have vanished. For the other densities, the largest cluster size (large for $\phi = 0.06$ and giant for $\phi = 0.1$), persists at low $\dot{\gamma}$, but it vanishes at $\dot{\gamma}\tau = 0.007$. The further increase in $\dot{\gamma}$ leads to the disappearance of the next cluster-size population. It is also interesting to note how the clusters elongate as the system is sheared, as well as that free arm extend more than clusters since the energetic loss is smaller.

To have a quantitative measure of the change in cluster size with $\dot{\gamma}$ we show in Fig. 4.17 the average number of patches $\langle N_p \rangle$ as well as the average size $\langle S_p \rangle$. For $\phi = 0.01$ we find that the number of clusters fluctuates around an average values of 39 and the number of arms in a cluster is slightly higher than 2 regardless of $\dot{\gamma}$. These results seem to indicate that no or little changes in this respect occur in the dilute system when shear is applied. We will in short demonstrate that the constant average characteristics of the clusters are actually also almost conserved at cluster level. At $\phi = 0.1$, $\langle N_p \rangle$ increases with $\dot{\gamma}$ whereas $\langle S_p \rangle$ decreases. This result is consistent with our observation that larger clusters break down into smaller ones as the system is subjected to a higher shear rate. In the intermediate share regime ($\phi = 0.06$) we observe a constant number of clusters (largest than for the other values of ϕ), which goes a bit down for $\dot{\gamma}\tau \geq 0.01$. This decrease appears not to be accompanied by a increase in average cluster size.

From the previous analysis, two questions arise. The first one is whether the constant average values $\langle N_p \rangle$ and $\langle S_p \rangle$ for the dilute system results of effectively no changes induced by the shear, or of a subtle reorganization of the clusters resulting in the same average parameters. The second question that interests us concerns the change in cluster number and/or size observed for $\phi = 0.06$ and $\phi = 0.1$; are these the results of arms breaking free from the clusters or clusters breaking down into smaller ones? In order to answer these questions we proceed to plot the cluster size

4 SEMIDILUTE AND CONCENTRATED REGIMES

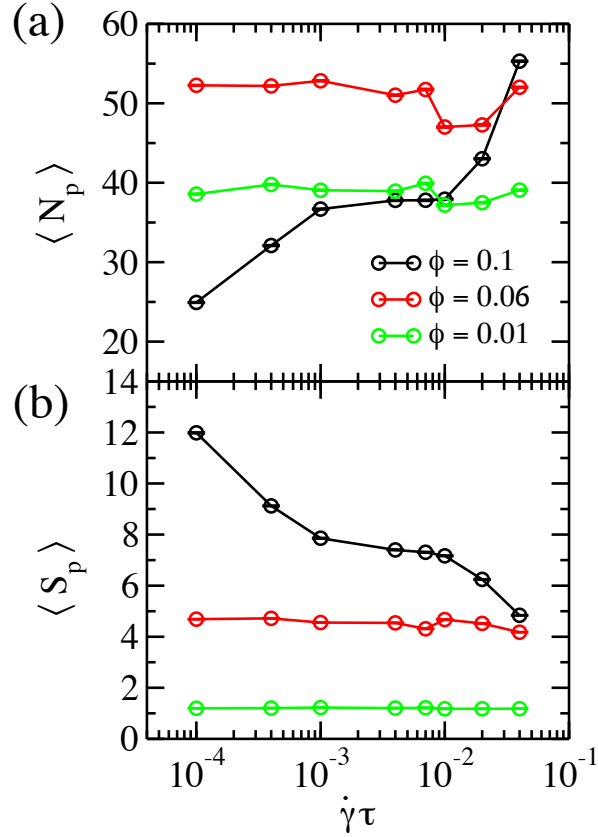


Figure 4.17. (a) Average number of patches $\langle N_p \rangle$ and (b) average number of arms clustered in a patch $\langle S_p \rangle$ for $\alpha = 0.3$ as functions of the shear rate for the three monomer packing fractions indicated in the legend.

distribution as function of the number of arms for selected $\dot{\gamma}$ (see Fig. 4.18). For $\phi = 0.01$ the free arms ($S_p = 1$) represent the vast majority of the distribution, followed by 2-arms clusters. The number of free arms appears to remain constant with shear, whereas the population of clusters with $S_p \geq 3$ declines slightly while cluster with $S_p = 2$ become more numerous (Fig. 4.18(a)).

The changes in the distributions only affect around 1% of the clusters and are therefore not visible in the average values. There are two mechanisms that could affect the distribution in this way: either bigger clusters break into clusters with $S_p = 2$ (which is unlikely since there are also clusters containing an odd S_p) or patches are first broken by shear and then they reform into two-arm aggregates which is probably the more realistic scenario.

For $\phi = 0.06$, as shear increases, we observe that the number of free arms increases at the expense of the bigger clusters ($S_p \geq 3$), the population of 2-arm ones increasing slightly. This is consistent with arms being pulled out from clusters by the flow. For $\phi = 0.1$, we also observe an increase with shear in the number of free arms though less important than for $\phi = 0.06$. However, at the same time population of small clusters ($2 \leq S_p \leq 6$) grows and the one of larger clusters go down. At this density the reorganization of the network seem to be the result of both arms

4 SEMIDILUTE AND CONCENTRATED REGIMES

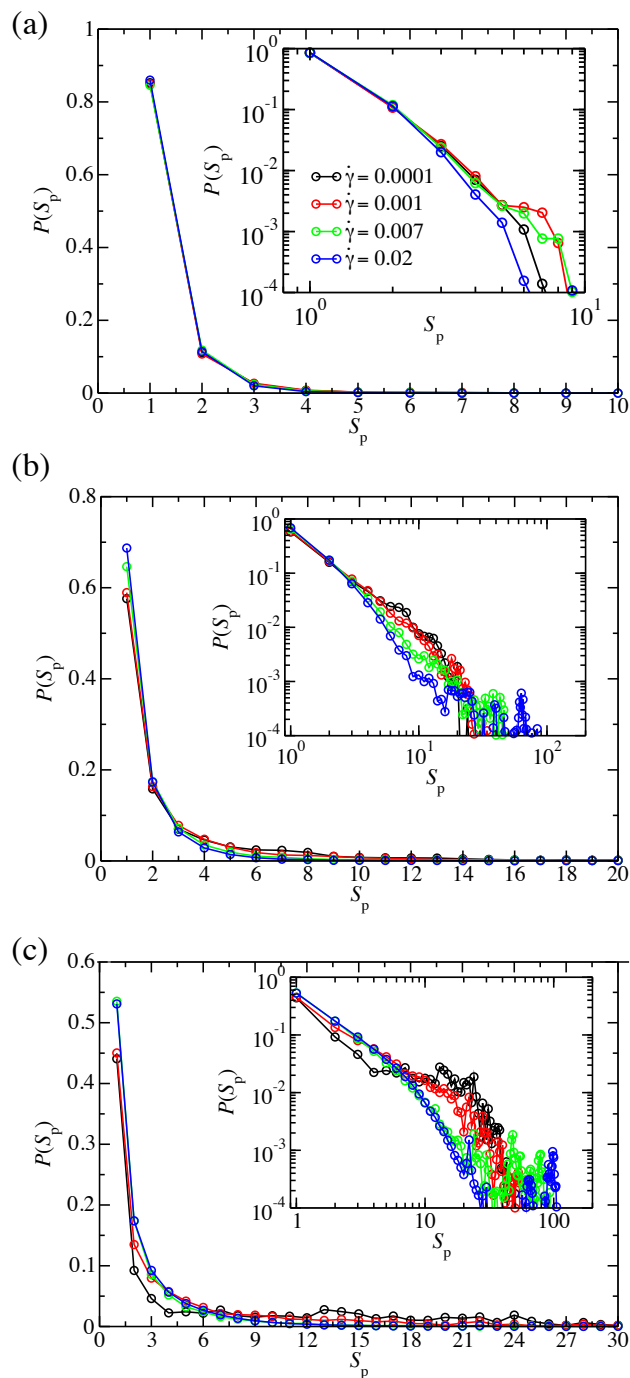


Figure 4.18. Patch size distribution $P(S_p)$ for $\alpha = 0.3$ and different values of the shear rate and monomer volume fraction: (a) $\phi = 0.01$, (b) $\phi = 0.06$, and (c) $\phi = 0.1$. The insets show a log-log representation of $P(S_p)$.

breaking free from the larger-sized cluster but also a result of fragmentation of these clusters.

4 SEMIDILUTE AND CONCENTRATED REGIMES

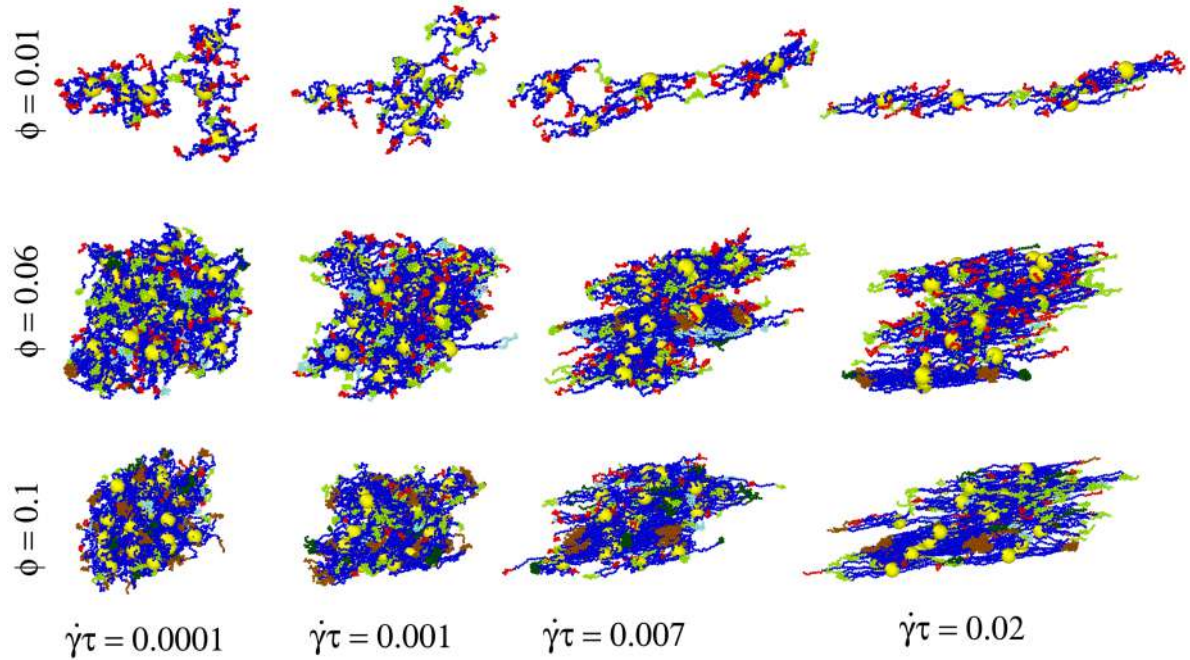


Figure 4.19. Snapshots of typical groups of connected SBCs for $\alpha = 0.3$ and different shear rate and volume fractions. The non-functionalized part of the star is colored in blue, whereas the functionalized blocks have been colored according to the size of the clusters they are part of using the same color code as in Fig. 4.16. To make individual stars easier to visualize, the anchors, which are depicted in yellow, have been drawn at a four times larger scale than their actual size.

4.4.4.a Connectivity

Another measure of the morphological changes occurring in our SBC systems when shear is applied, is related to the connectivity of the system. Groups of connected SBCs at different shear rates and densities are presented in Fig. 4.19. At the lowest density considered, the shape of the connected component as a whole changes when shear is applied, becoming more elongated. The elongation does not only come from the stretching of stars but also from re-organization of the inter-star connections. This allows the SBCs to align to the flow, facilitating the movement as a group, while as many inter-star connections as possible are kept. This behavior is consistent with the observed shear banding phenomena.

The number of stars per connected component decreases with shear rate since stars that become free at some point in time are carried away by the flow, making their re-attachment unlikely. At higher densities, the SBCs appear to form a percolating network which seems to survive shear. The most interesting phenomena found is that, when stars elongate under the effect of shear, a sort of stacked configuration is observed, meaning that the stars bring their anchor almost in contact forming a string-like or stack-like structure. The non-interacting part of the stars which are on either side of the anchor also stack, as well as the attractive parts. This organization was hinted at

4 SEMIDILUTE AND CONCENTRATED REGIMES

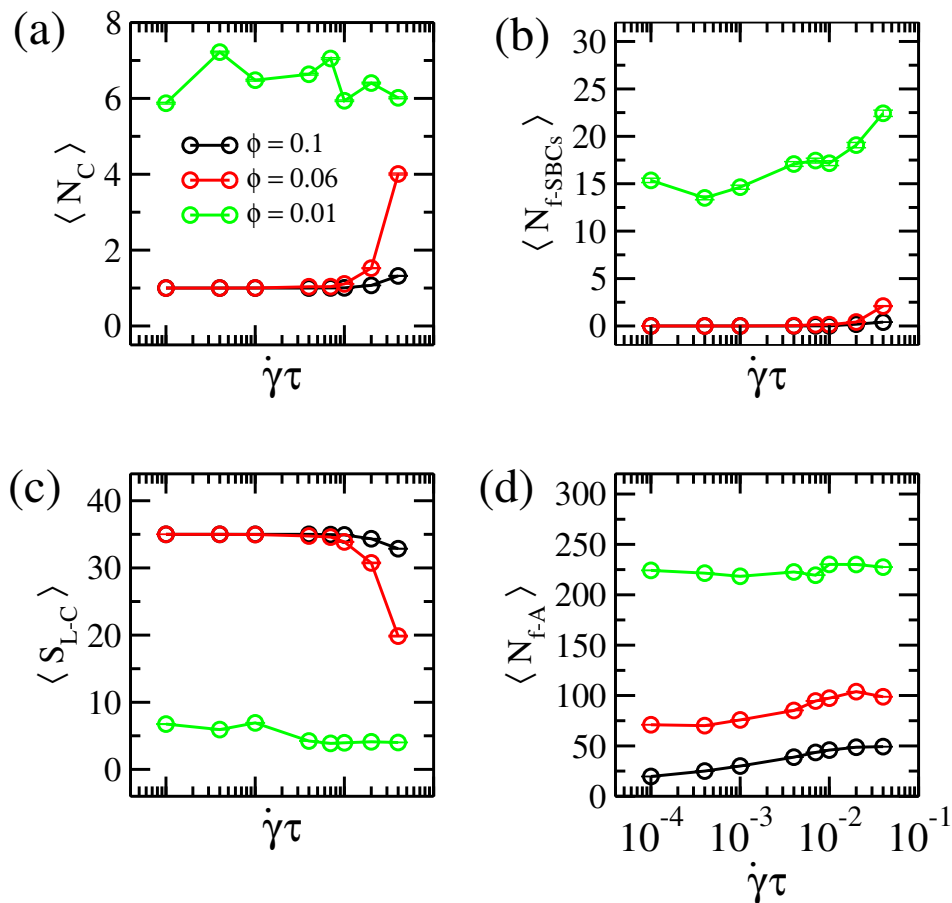


Figure 4.20. Connectivity parameters as a function of shear rate for $\alpha = 0.3$ and different concentrations: (a) average number of components, (b) average number of free stars, (c) average size of the largest component and (d) average number of free arms.

by the radial correlation functions.

To better understand the changes that shear generates in structure of the system, we look at the connectivity of the system by measuring the size of the connected components present (i.e., the number of connected stars). In Fig. 4.20 we show the average number of components, the average number of free stars, the average size of the largest component and the number of free arms for the whole system. We find that except in the dilute system ($\phi = 0.01$), where it is composed out of multiple components ($\approx 6 - 7$) regardless of the shear rate, the system is completely connected up to $\dot{\gamma}\tau = 0.01$. This single component contains all the stars in the system (the number of free stars being zero), meaning we have a percolating network as we had already hinted in the previous paragraph. At $\phi = 0.1$, for the higher shear rates a small number of single SBCs start to fragment from the percolating component, the rest of the stars remaining connected. In addition to the release of a few free stars, at $\phi = 0.06$, the network breaks for $\dot{\gamma}\tau = 0.04$ into a two big pieces ($\approx 10 - 20$ stars). The low density behavior is different: many stars are free (more that 40%) and

4 SEMIDILUTE AND CONCENTRATED REGIMES

this further increases with the shear rate. The size of the largest component in the system only contains 6–7 stars which decreases to ≈ 4 stars for high shear rates.

The number of free arms can offer further clarification on the connectivity. For $\phi = 0.01$ each star has, on average, 6 to 7 free arms which means that only 2 or 3 are bound. Considering that arms can bind within a star, not only creating inter-star connections, it is to be expected that the size of components is low and the number of free stars high. At $\phi = 0.06$, around 2 arms per star are free, whereas at $\phi = 0.1$ only one arm in each stars is unbound. These values increase with the shear rate up to ≈ 3 and respectively ≈ 1.5 free arm per star. With such a high number of attached arms, it is natural is that we obtain a percolating network.

4.4.5 Viscosity

A very important macroscopic property of non-Newtonian fluids in general and of (associating) polymer solutions in particular is the viscosity, which bears the signature of the polymer architecture and chemistry. Unlike the previously presented properties that can be challenging to address experimentally, the viscosity can be measured in rheological experiments. Determining this quantity provides thus an important link between microscopic organization of the BCSs and the macroscopic behavior of the material.

Here we calculate the polymer viscosity η_p , which is expected to dominate the total viscosity at sufficiently high concentrations, and which is also responsible for the non-Newtonian linear rheology of the system. To this effect, we calculate the stress tensor σ_p that involves kinetic and interaction contributions for the polymer beads, involving exclusively the forces exerted by other beads, and can be conveniently computed via the relation:

$$\sigma_p = \frac{1}{V} \left\langle \sum_{i=1}^{N_t} M \tilde{\mathbf{v}}_i \otimes \tilde{\mathbf{v}}_i + \frac{1}{2} \sum_{i=1, j \neq i}^{N_t} \mathbf{r}_{ij} \otimes \mathbf{F}_{ij} \right\rangle. \quad (4.5)$$

Here, $M = 5m$ is the monomer mass, $V = L_{\text{box}}^3$ is the volume of the simulation box, $N_t = N_s N_{\text{mon}}$ is the total number of monomers, $\tilde{\mathbf{v}}_i = \mathbf{v}_i - \dot{\gamma} y_i \hat{\mathbf{x}}$ is the peculiar velocity of the i -th monomer, $\mathbf{r}_{ij} = \mathbf{r}_i - \mathbf{r}_j$ and \mathbf{F}_{ij} is the pair monomer-monomer force, including both FENE and Lennard-Jones-like contributions.

In Fig. 4.21 we present the polymer viscosity $\eta_p = \sigma_{p,xy} / \dot{\gamma}$ as a function of the shear rate $\dot{\gamma}$ at both $\alpha = 0.3$ and $\alpha = 0.5$ for the three densities considered. As a general trend, we observe higher viscosity for more concentrated systems and also a shear thinning behavior, i.e., a decreasing viscosity as the shear rate increases, for all the systems studied. The two higher monomer fraction systems ($\phi = 0.1$ and $\phi = 0.06$) feature a very similar behavior. At low shear rates the systems with $\alpha = 0.5$ exhibit a stronger shear thinning. For $\dot{\gamma} \tau \geq 10^{-3}$, curves for both α -s collapse, the slopes being very similar (-0.56 respectively -0.57). For the dilute systems we also observed a

4 SEMIDILUTE AND CONCENTRATED REGIMES

collapse of the the two curves for high $\dot{\gamma}$, however the slope is only -0.43 . This last result is slightly higher than the values reported in the literature for semi-dilute solutions of stars with less than 50 arms [105].

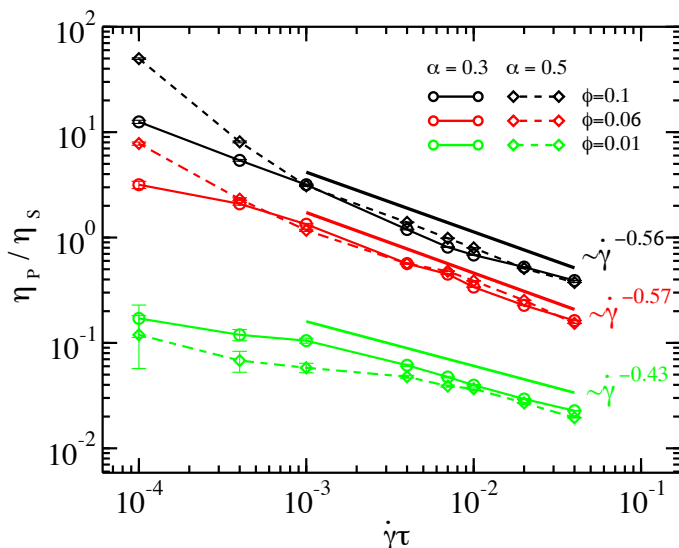


Figure 4.21. The polymer viscosity η_p , expressed in units of the solvent viscosity η_s , as a function of the shear rate for the systems under consideration.

4.5 Conclusions

We have carried out detailed, monomer-resolved, off-lattice simulations of associating, SBCs of moderate functionality to investigate the structure, equilibrium dynamics, and molecular conformations of the building blocks in the resulting macroscopic networks formed by the system at finite concentrations. Though still far away from the melt (and thus also from any considerations regarding entanglements between the chains), the system features the nontrivial characteristics of self-organized networks of associating polymers. The choice of the functionality and the fraction of attractive monomers drives the system into a network configuration rather than toward the formation of micelles. The network is homogeneous, i.e., there exist uniformly distributed physical association sites, which are not broadly polydisperse in size, and these are interconnected through the star arms that are anchored on their centers. We find characteristic spatial correlations and scattering spectra that feature short- and intermediate-range ordering at the monomer- and macromolecule-length scales, in close similarity with findings on telechelic linear chains [104], whereas the patches compactify and internally crystallize at strong attractions when the temperature drops well below the Θ -point of the terminal groups. A major finding of this work is that

4 SEMIDILUTE AND CONCENTRATED REGIMES

within the networks the stars reorganize and reconfigure to best take advantage of the anisotropic environment of potential association partners: the dumbbell-shape of infinite dilution is lost and the stars recover a spherical shape with their arms reaching out toward association partners in all spatial directions around their cores. In stark contrast to usual stars, this conformational change upon an increase of concentration is accompanied by a *growth* of the overall size, since the stars abandon the relatively compact dumbbell-shape to assume an open, radially-symmetric configuration. The model we adopted is monomer-based but still considerably coarse-grained: in particular, no possible differences in size, Kuhn lengths, or rigidities between the A- and B-blocks have been considered and no particular chemistry has been employed. Still, we believe that the approach contains the salient physical characteristics to capture the main mechanisms and properties of network formation.

In the final part of this chapter, we analyzed the global structure, patchiness, and viscosity of suspensions of SBC under shear flow. Following recent studies on the self-assembly and networks formation in low-functionality SBC systems, we explored their non-equilibrium behavior from semi-dilute ($\phi/\phi^* \sim 0.2$) to concentrated ($\phi/\phi^* \sim 1.7$) regimes. As previously described, the chosen parameters, i.e., functionality, amphiphilicity, and attraction strength between solvophobic segments, lead the system to the formation of homogeneous percolating networks, whose patchiness, morphology and connectivity are significantly reorganized by the shear rate. As the latter increases, the SBCs in the network elongate in the shear direction and shrink in the other two, compelling the larger clusters of B-monomers (patches) to break up into smaller ones. This effect becomes more important as the concentration increases (see Figure 4.17), leading to the rising of the number of patches but of a smaller size. As well as, a stacked configuration of SBCs is observed, which allows the star cores to align in stack-like structure, which is reminiscent of the scaffold-like structures observed in rigid, linear telechelic polymers [66].

Regarding the viscosity of the system, the more inter-star association takes place as the concentration increases leading to an increasing zero-shear viscosity [34]. As shear enters into play, the breaking of patches plus the SBC re-orientation results in thixotropic behavior (shear thinning) with the thinning exponent growing in magnitude with the concentration of the solution. The stars reorganize significantly during shear and change morphology. This could be interesting for the experimental application perspective since anchors could be functionalized in such a way that they have an extra linking possibility to reinforce the network.

5 | MPCD for a coarse-grained model of soft colloids

The growing interest in the dynamical properties of colloidal suspensions, both in equilibrium and under an external drive such as shear or pressure flow, requires the development of accurate methods to correctly include hydrodynamic effects due to the suspension in a solvent. In the present work, we generalize Multi-Particle Collision Dynamics (MPCD) to be able to deal with soft, polymeric colloids. Our methods builds on the knowledge of the monomer density profile that can be obtained from monomer-resolved simulations without hydrodynamics or from theoretical arguments. We hereby propose two different approaches. The first one simply extends the MPCD method by including in the simulations effective monomers with a given density profile, thus neglecting monomer-monomer interactions. The second one considers the macromolecule as a single penetrable soft colloid (PSC), which is surrounded by an inhomogeneous distribution of solvent particles. By defining an appropriate set of rules to control the collision events between the solvent and the soft colloid, both linear and angular momenta are exchanged. We apply these methods to the case of linear chains and star polymers for varying monomer lengths and arm number, respectively, and compare the results for the dynamical properties with those obtained within monomer-resolved simulations. We find that the effective monomer method works well for linear chains, while the PSC method provides very good results for stars. These methods pave the way to extend MPCD treatments to complex macromolecular objects such as microgels or dendrimers and to work with soft colloids at finite concentrations.

5.1 Introduction

Thanks to the increased computational capacities and to the development of better algorithms, computer simulations are nowadays well established tools to predict and analyse the properties of soft matter systems, such as polymer and colloid dispersions. For these systems, a major challenge is to adequately treat phenomena taking place at different length- and time scales and to improve our understanding of how structure and dynamics at the microscale determine both the functional behavior and performance of the system at the macroscale. For the specific case of polymer solutions, the characteristic timescales span from the typical time of molecular motion of the solvent particles ($\sim 10^{-12}$ s) up the relaxation time of the polymers ($10^{-6} - 10^2$ s). In addition, the lengthscales extend from 1 nm all the way to 1 μm , or even larger, in case that supramolecular structures spontaneously form.

To tackle these problems, we evidently cannot rely on molecular dynamics (MD) simulations which retain all the microscopic degrees of freedom, but we need to adopt the use of coarse-grained models. Applying these ideas to suspensions leads to a simplified, mesoscopic description of the solvent, in which embedded solutes are treated by conventional molecular dynamics simulations [46]. For example, as a first approximation the solvent can be implicitly taken into account through Brownian dynamics (BD) simulations, which assume that collisions between solutes and solvent particles lead to random displacement of the former while thermalizing them. In a similar fashion, Stokesian Dynamics (SD) considers the relative motion of the solute with respect to the solvent by introducing hydrodynamic interactions (HI) among solute particles, which can be decomposed into long-range mobility interactions and short-range lubrication effects [106].

More explicit mesoscopic models for the solvent include a number of discrete algorithms, whose main ingredients are reflected in local conservation laws (mass, momentum, energy) at adequate selected scales, which allow to recover the Navier-Stokes equation in the continuum limit. Among these approaches, one can find Dissipative Particle Dynamics, Lattice-Boltzmann method, Direct Simulation Monte Carlo, and Multi-Particle Collision Dynamics (MPCD). The MPCD method [7, 50, 107] assumes that the solvent is composed by non-interacting, point-like particles, whose dynamics proceed in two steps: a streaming step and a collision step. In the former, solvent particles move ballistically while in the latter they exchange linear momentum among themselves and with solute particles through the use of virtual, cubic cells in which they are sorted. Although such dynamics is a strongly simplified representation of real dynamics, it conserves mass, momentum, and energy, while preserving phase space volume. Consequently, it retains many of the basic characteristics of classical Newtonian dynamics [107].

MPCD allows to incorporate in the simulations HI as well as Brownian fluctuations, both being necessary for a correct description of the characteristic density- and thermal fluctuations of soft matter systems. Thus, a hybrid MD-MPCD method has proven to be successful for the simulation

5 MPCD FOR A COARSE-GRAINED MODEL OF SOFT COLLOIDS

of the dynamics of colloids, dendrimers, polymers, vesicles, and red blood cells both in equilibrium and under flow conditions [47, 57, 108–113].

An important point when dealing with colloid and polymer suspensions is how to couple the suspended particles with the solvent. In the simplest standard method, each colloidal particle or monomer of a polymer is considered as a point-like particle which participates in the momentum exchange during the collision step. In this situation, it is assumed that only one particle (i.e., monomer or colloid) is embedded in the cell and that the average total mass of the solvent particles in the cell is of the same order as that of the particle [46, 50]. A more elaborate method takes into account the reflection that (MPCD) solvent particles undergo when they collide with the surface of a hard solute, which allows to couple the former with the latter through the exchange of both linear and angular momentum during the streaming step [114, 115].

The computational simplicity of the streaming and collision steps allows for highly efficient MPCD implementations, which exploit the massively parallel computational capabilities of graphics processing units (GPUs) [116, 117]. In spite of these advantages, the treatment of semi-dilute and dense suspensions of polymers with complex architecture, such as dendrimers, micelles, microgels or star polymers, still suffers from a number of limitations from the computational point of view, due to the fact that these objects are typically composed of a large number of monomers, whose interactions are described by force-fields that require a large amount of more computational resources. This becomes even more important as the concentration and/or branching and polymerization degree increase. Indeed, this requires the inclusion of the necessary number of (MPCD) solvent particles, making the simulation of large systems quite demanding. Therefore, despite a number of works on the topic that include the study of semidilute solutions, [47, 65, 80, 118–122] the study of polymer suspensions within this framework has been limited up to now by the very high computational demand of treating the polymers in a detailed, monomer-resolved fashion while in parallel keeping track of the MPCD-solvent degrees of freedom. In this respect, a suitable combination of the MPCD efficiency with a simplified model for the polymeric objects could provide a boost to the understanding of the dynamics and of the rheology of semi-dilute and dense suspensions.

Polymer systems are good examples for the application of a hierarchical coarse-graining procedure: at the first level, the monomers constituting the polymers can be identified by their centres of mass only, giving rise to a monomer-resolved description. Then, the number of degrees of freedom can be further lowered by considering polymeric chains as composed of several blobs, each containing a certain number of monomers, which still keep the main features of the polymer such as size scaling, chain connectivity and uncrossability of different chains. Finally, one can go as far as describing the whole polymer as a single penetrable, soft sphere centered on the polymer center of mass, which size is of the order of the polymer radius of gyration [4, 123]. In the last case, the interaction between two polymers can be described via soft, effective potentials, which

5 MPCD FOR A COARSE-GRAINED MODEL OF SOFT COLLOIDS

are realized by, for example, micelles, star polymers, dendrimers or microgel particles [103, 124, 125].

We propose two new approaches to MD-MPCD simulations of macromolecular systems suspended in a solvent. Both methods build on the use of the average (radial) distribution of monomers $\rho_{\text{mon}}(r)$ around the center-of-mass of the macromolecule, which embodies its global conformation. The latter observable can be readily obtained from numerical approaches in the absence of HI and/or from theoretical arguments. In the first method, we propose a simple generalization of the MD-MPCD standard algorithm, where the monomer-resolved model is replaced by a rigid, effective polymer, which is built up following $\rho_{\text{mon}}(r)$. The interactions between effective monomers are neglected, and hence, the (diffusive) dynamics of the macromolecule is determined by the exchange of linear momenta during the collision step between the effective monomers and MPCD solvent particles, which are homogeneously distributed in the simulation box. The second method goes one step further by modelling the macromolecule as a single, spherical penetrable colloid (PSC). In this case, the monomer density profile is employed to determine the probability of the solvent particles to penetrate inside the soft colloid. This penetrability condition implies the definition of a new set of collision rules, different with respect to those for hard colloids [114, 115], which couple PSC and solvent particles through the exchange of both linear and angular momenta during the collision step.

We apply both approaches to the case of an isolated linear polymer chain with varying degree of polymerization and to a star polymer with different number of arms immersed in a good solvent. We focus on the long-time dynamics of the center-of-mass (COM), in particular, its (long-time) diffusion coefficient, comparing the results of the two types of MD-MPCD simulations with the monomer-resolved description. We find that the first method captures quite well the dynamical behavior of a polymer chain, while it does not reproduce well enough the dynamics of star polymers. This result shows that the monomer-solvent and monomer-monomer coupling need to be taken into account to describe complex polymeric objects. On the other hand, the penetrable sphere model turns out to be very good to describe the dynamics of macromolecules with an isotropic density profile such as stars, while its performance for linear chains, that are instantaneously more anisotropic, is rather poor. Hence our work offers insights to appropriately calibrate the most suitable MD-MPCD method to the macromolecule of interest.

The rest of the chapter is organized as follows. In *Sec. 5.2*, we describe the simulation models, i.e., effective monomers and soft-colloid ones as well as the fundamental concepts needed for the present study of polymeric objects. Next, we describe the two methods and we extensively discuss and test the collision rules used in the second approach to achieve the coupling between the solvent and the soft colloid. In *Sec. 5.3*, we compare the outcomes of the two MD-MPCD methods with monomer-resolved ones. Finally, we summarize our findings in *Sec. 5.4* and discuss the perspectives of this work.

5.2 Methods

5.2.1 Multi-Particle Collision Dynamics

Molecular dynamics simulations were performed for isolated linear polymers with degree of polymerization $N_{\text{pol}} = \{50, 100, 200\}$ and star polymers with arm number (or functionality) $f = \{5, 10, 15, 20\}$ and $N_{\text{pol}} = 30$ in a cubic box of size $L = 45\sigma$ featuring periodic boundary conditions. Two sets of simulations were employed: (i) Langevin Dynamics simulations were used to evaluate static properties of the polymers such as the monomer density profiles around the center of mass $\rho_{\text{mon}}(r)$, the gyration radius R_{gyr} and the inertia moment I , which were calculated by averaging over $\sim 10^5$ independent configurations; (ii) MD-MPCD runs were performed for each set of parameters to evaluate dynamic properties. The results were averaged over fourteen independent runs where each run consisted of 10^4 and 10^6 MPCD steps for equilibration and production stages, respectively. The temperature of the system was controlled by means of a cell-level Maxwell–Boltzmann scaling [49], for the solvent particles. During the production run, 4×10^4 configurations were saved to measure the mean square displacement $\langle \Delta r^2 \rangle$ of the polymers center-of-mass as well as the corresponding (long-time) diffusion coefficient D^H and hydrodynamic radius R_{hyd} .

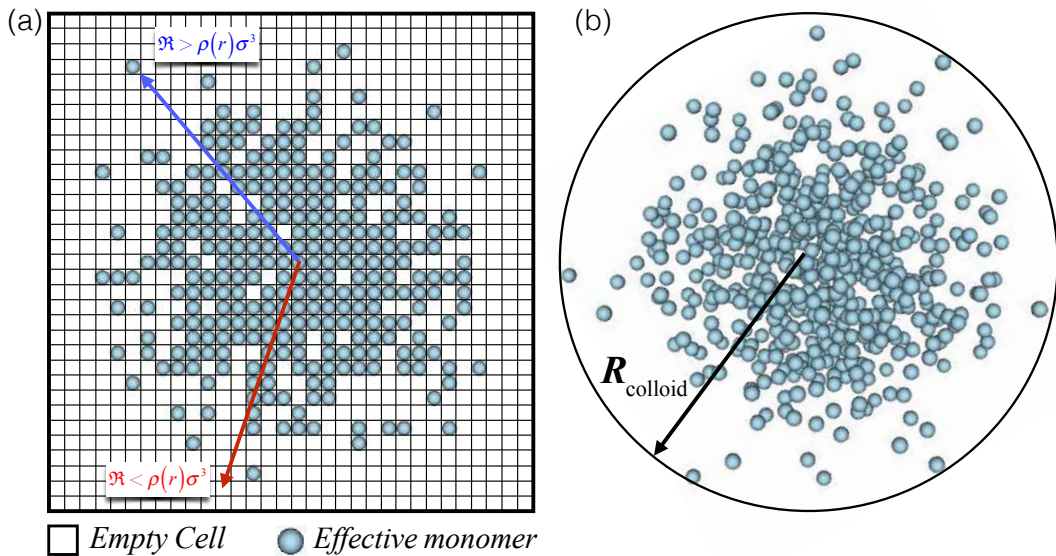


Figure 5.1. (a) Schematic representation of the effective monomers model: in the simulation box, each square represents a collision cell used in MPCD simulations. The blue arrow indicates the case in which an effective monomer is placed in the collision cell, while the red arrow refers to the opposite situation. More details are explained in the main text. (b) A representation of star polymer in the EMM approach, where R_{colloid} is the radius of the sphere enclosing all monomers.

5.2.2 Effective monomer model (EMM)

In this approach, we consider the average monomer density profile $\rho_{\text{mon}}(r)$ calculated via the MRM simulations discussed in the earlier section and randomly assign the positions of N_{eff} “effective” monomers within the simulation box following such distribution. To this aim, first the simulation box is divided into collision cells, and then, we put a sphere in the center of the box whose radius R_{colloid} satisfies the condition $\rho_{\text{mon}}(R_{\text{colloid}})\sigma^3 < 10^{-3}$. Afterwards, for each cell inside such a sphere, we extract a uniform random number, $\mathcal{R} \in (0, 1)$ and if $\mathcal{R} \leq \rho_{\text{mon}}(r)\sigma^3$, we insert a monomer with mass M and diameter σ in the center of the cell, as shown in Fig 5.1(a). This process is repeated for all the cells inside the sphere until all effective monomers are placed. We thus obtain a fictitious topology representing the macromolecule of interest, which is kept fixed throughout the simulation run. In Fig 5.1(b) we illustrate an example of effective configuration for a star polymer obtained using the EMM model.

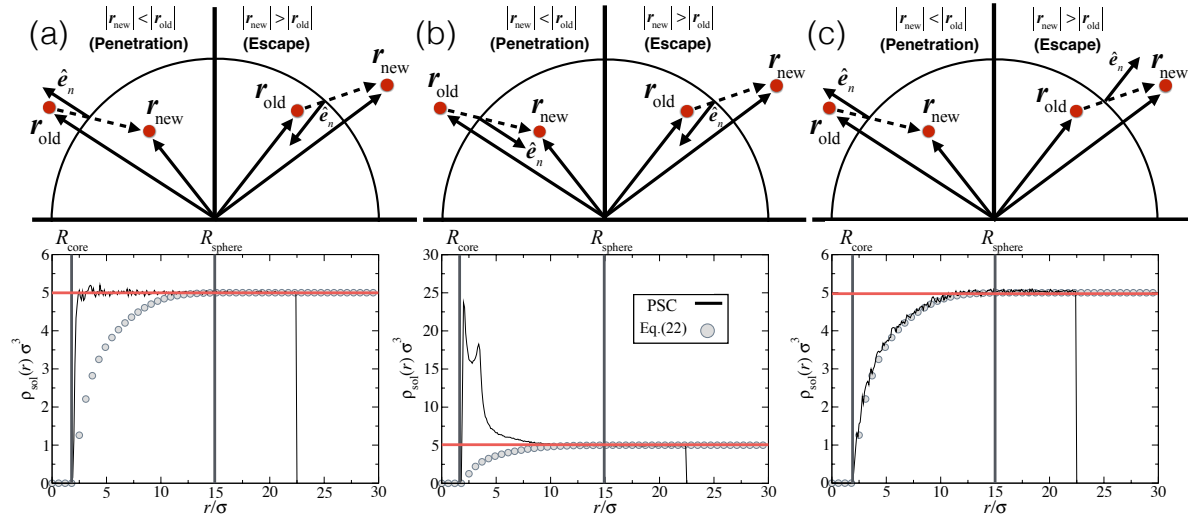


Figure 5.2. Influence of the choice of the direction of the normal velocity component \hat{e}_n of the solvent, illustrated on the top panel, after a collision with the PSC on the generated solvent density profile, reported in the bottom panel. Three different choices of the direction of \hat{e}_n are possible: (a) symmetric rules which give rise to a homogeneous solvent profile; (b) in-going direction of \hat{e}_n which originates the accumulation of solvent particles around the core of the PSC; (c) out-going direction of \hat{e}_n yielding the desired solvent density profile. In all cases, simulations refer to a star polymer with $f = 5$. The colloidal size R_{colloid} and the core radius R_{core} are indicated by the vertical black lines, whereas the horizontal red line represents the solvent density $\rho_{\text{sol,bulk}}$ in the bulk. In the bottom panels, the solid black line is the solvent profile obtained by the PSC simulations, while filled symbols indicate the theoretical curve obtained by Eq. (5.16).

We treat the set of effective monomers as a rigid body; hence, at each collision step, the velocity of each effective monomer $\mathbf{V}_j(t)$ is equal to that of the COM of the polymeric object $\mathbf{V}_{\text{pol}}(t)$. Then, as in the MD-MPCD standard algorithm, the dynamical coupling between solvent particles and monomers is described by Eq. (2.13), yielding the new velocity $\mathbf{V}_j(t+h)$ for each monomer. To

5 MPCD FOR A COARSE-GRAINED MODEL OF SOFT COLLOIDS

calculate the velocity of the COM of the macromolecule, we have

$$\mathbf{V}_{\text{pol}}(t+h) = \frac{\sum_j^{N_{\text{eff}}} \mathbf{V}_j(t+h)}{N_{\text{eff}}}, \quad (5.1)$$

that is used to determine the evolution of the polymeric object through MD simulations. We repeat this procedure for ten independent topologies, whose average gives us an effective macromolecule with number of effective monomers $N_{\text{mon}} = \langle N_{\text{eff}} \rangle$.

5.2.3 Soft colloid MD-MPCD simulations

In a more advanced model, the polymer chain or star polymer are described as a single penetrable soft colloid (PSC), which retains some information regarding its average conformation through the average monomer density profile $\rho_{\text{mon}}(r)$. In this case, the coupling between the solvent particles and the PSC is based on the consideration that monomers exclude solvent particles from their interior and therefore, the solvent density profile $\rho_{\text{sol}}(r)$ around the PSC center-of-mass can be written as

$$\frac{\rho_{\text{sol}}(r)}{\rho_{\text{sol,bulk}}} = 1 - \eta_{\text{mon}}(r) = 1 - \frac{\pi}{6} \rho_{\text{mon}}(r) \sigma^3, \quad (5.2)$$

where $\rho_{\text{sol,bulk}}$ and $\eta_{\text{mon}}(r)$ denote, respectively, the solvent bulk density and the (radial) monomer volume fraction. Besides, the monomer density profile $\rho_{\text{mon}}(r)$ satisfies the condition:

$$4\pi \int_0^{R_{\text{colloid}}} r^2 \rho_{\text{mon}}(r) dr = N_{\text{mon}}, \quad (5.3)$$

where $N_{\text{mon}} = N_{\text{pol}}$ for linear polymers and $N_{\text{mon}} = f N_{\text{pol}}$ for star polymers, and R_{colloid} is a measure of the PSC size.

For a star polymer, $\rho_{\text{mon}}(r)$ can attain values larger than $6/(\pi\sigma^3)$ close to its center, so that $\rho_{\text{sol}}(r)$ can become negative. To guarantee that $0 \leq \rho_{\text{sol}}(r) \leq \rho_{\text{sol,bulk}}$, the corresponding PSC model is considered equivalent to a core-shell particle, with a core radius R_{core} defined such as the scaling-law $\rho_{\text{mon}}(r > R_{\text{core}}) \sim r^{-4/3}$ holds. R_{core} can be thought as the limit of the melt region around the COM of the star, so that no solvent can penetrate inside this region, i.e. $\rho_{\text{sol}}(r < R_{\text{core}}) = 0$. According to scaling theory, $R_{\text{core}} \sim f^{1/2}\sigma$ and the monomer density at this distance must have the same value for all stars [123], i.e. $\rho_{\text{mon}}(r < R_{\text{core}}) = \rho_{\text{core}}$. As schematically represented in Fig. 5.2, once the distribution of the (MPCD) solvent particles around the macromolecule COM is established, the next step is to introduce a set of collision rules which govern the dynamical coupling between the solvent and the PSC.

5.2.3.a Coupling between solvent and colloids

While standard MPCD is not able to capture the angular momentum exchange during the collision step, first Inoue *et al.* [114] and later Nikoubashmann *et al.* [115] have successfully proposed a rule for coupling the solvent to hard colloids through the exchange of both linear and angular momenta during the collision step. In this framework, the i -th solvent particle collides at a point \mathbf{s}_i on the surface of a rigid sphere, which can be roughly estimated as

$$\mathbf{s}_i = \mathbf{R}(t) + \frac{\sigma_{hs}}{2} \frac{\mathbf{r}_i(t) - \mathbf{R}(t)}{|\mathbf{r}_i(t) - \mathbf{R}(t)|} = \mathbf{R}(t) + \frac{\sigma_{hs}}{2} \mathbf{e}_n \quad (5.4)$$

where σ_{hs} is the diameter of the rigid particle, \mathbf{e}_n is the unit vector normal to the collision surface, and $\mathbf{r}_i(t)$ and $\mathbf{R}(t)$ are the position of the i -th solvent particle and the hard-sphere center at time t , respectively. Then, as the solvent particle is scattered after the collision, both its normal v_n and tangential v_t relative speeds are randomly selected from the distributions [115]

$$p(v_n) = m\beta v_n \exp\left(-\frac{1}{2}m\beta v_n^2\right) \quad (5.5)$$

and

$$p(v_t) = \sqrt{\frac{m\beta}{2\pi}} \exp\left(-\frac{1}{2}m\beta v_t^2\right), \quad (5.6)$$

$\beta = (k_B T)^{-1}$ being the inverse temperature. Thus, linear and angular momenta are exchanged between the solvent particles and the rigid particle as

$$\mathbf{v}_i(t+h) = \mathbf{V}(t) + \mathbf{L}(t) \times [\mathbf{s}_i - \mathbf{R}(t)] + v_n \mathbf{e}_n + v_t \mathbf{e}_t \quad (5.7)$$

$$\mathbf{V}(t+h) = \mathbf{V}(t) + \frac{m}{M} [\mathbf{V} - \mathbf{v}_i(t+h)] \quad (5.8)$$

$$\mathbf{L}(t+h) = \mathbf{L}(t) + \frac{m}{I} [\mathbf{s}_i - \mathbf{R}(t)] \times [\mathbf{v}_i(t) - \mathbf{v}_i(t+h)], \quad (5.9)$$

where $\mathbf{V}(t)$ and $\mathbf{L}(t)$ are the linear and angular velocity of the hard colloid, respectively, I its moment of inertia, and \mathbf{e}_t is the tangential unit vector. Once the collision occurs, the solvent particle is displaced half the time step from the initial position $\mathbf{r}_i(t)$ with the updated velocity \mathbf{v}_i following Eq. (5.7).

In contrast to hard colloids, soft ones do not have a well-defined surface, implying the presence of the solvent well inside its outer edge. Unlike previous works, [114, 115] where only solvent-hard particle collisions were implemented, here we consider a different situation for the solvent-soft colloid collisions. These are modelled taking into account two different trial movements, which

5 MPCD FOR A COARSE-GRAINED MODEL OF SOFT COLLOIDS

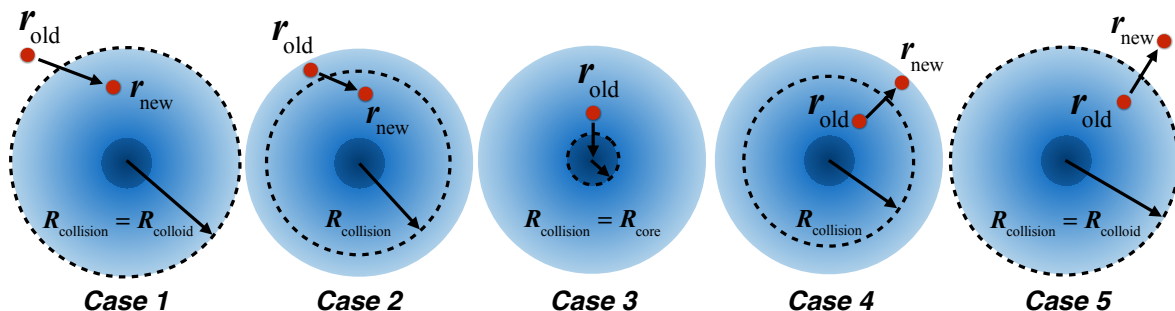


Figure 5.3. Schematic representation of the density profiles of monomer $\rho_{\text{mon}}(r)$ and solvent $\rho_{\text{sol}}(r)$ particles and the adopted collision rules for a generic soft penetrable colloid with a core radius R_{core} and a total radius R_{colloid} . The red point represents a solvent particle, whereas \mathbf{r}_{old} and \mathbf{r}_{new} are the positions at time t and $t+h$, respectively. For *Case 1* and *Case 4*, the solvent particle collides on the surface of the soft colloid; for *Case 2* and *Case 5* the collision takes place inside the colloid, with the effective collision radius being $R_{\text{collision}} < R_{\text{colloid}}$. Finally, the *Case 3* illustrates the collision with the core, and hence, $R_{\text{collision}} = R_{\text{core}}$.

correspond to penetration or escape of the solvent particles with respect to the soft colloid. In order to regulate the number of collisions, we use Eq. (5.2), aiming to maintain the correct solvent density profile around the PSC.

To do this, we build on the well-known Metropolis algorithm and consider a trial displacement of the i -th solvent particle from $\mathbf{r}_i(t)$ to $\mathbf{r}_i(t+h)$. We define the probability $P_{\text{old} \rightarrow \text{new}}$ for a solvent particle to go from the old position $r_{\text{old}} = |\mathbf{r}_i(t)|$ to the new one $r_{\text{new}} = |\mathbf{r}_i(t+h)|$, as

$$P_{\text{old} \rightarrow \text{new}} = \begin{cases} \min \left\{ 1, \frac{\rho_{\text{sol}}(r_{\text{old}})}{\rho_{\text{sol}}(r_{\text{new}})} \right\} & r_{\text{new}} < r_{\text{old}} \\ \min \left\{ 1, \frac{\rho_{\text{sol}}(r_{\text{new}})}{\rho_{\text{sol}}(r_{\text{old}})} \right\} & r_{\text{old}} < r_{\text{new}} \end{cases} \quad (5.10)$$

Then, the trial move is accepted if $P_{\text{old} \rightarrow \text{new}}$ is larger than a random number $\mathcal{R} \in (0, 1)$, and hence, the solvent particle propagates ballistically. On the other hand, if the trial move is rejected, a “solvent-PSC collision” takes place. In this case, the solvent particle is reflected using an “effective hard-sphere radius” $R_{\text{collision}}$ that defines an “effective impact point” via Eq. (5.4). Both linear and angular momenta are exchanged during this event.

In order to reproduce the appropriate dynamics of a PSC, we need to control the distribution of solvent around it which is physically prescribed by Eq. 5.2. This is achieved by adjusting the number of penetrating and escaping collisions in each step. To this end, the definition of transition probability shown in Eq. (5.10) must be complemented by an appropriate choice of a privileged direction for the normal solvent velocity component $\hat{\mathbf{e}}_n$ once the collision has occurred. In this way, we are able to adequately regulate the distribution of the solvent in the system.

In Fig. 5.2, we show how the density profile of the solvent is affected by the choice of the direction of $\hat{\mathbf{e}}_n$ in the cases where a collision happens during penetration and escape events. A

5 MPCD FOR A COARSE-GRAINED MODEL OF SOFT COLLOIDS

general case is considered where the velocity direction $\hat{\mathbf{e}}_n$ points outwards for penetration and pointing inwards for the escape events. In this way, we always reproduce a realistic rebound of the solvent particles, which provides a homogeneous solvent profile, as shown in Fig. 5.2(a). These conditions satisfy detailed balance, since that the transition probabilities described in Eq. (5.10) are symmetric. To break this symmetry, and hence, to reproduce an inhomogeneous density profile, we have to choose the same direction of $\hat{\mathbf{e}}_n$ for both events. Thus, if we always consider $\hat{\mathbf{e}}_n$ pointing inwards, we enforce a penetration to the inside of the solvent particles, as represented in Fig. 5.2(b), where an accumulation of solvent is detected around the core. On the other hand, if we consider the opposite case, where $\hat{\mathbf{e}}_n$ always points outwards, an escape to the outside is guaranteed. Thus, we always consider the last set of rules with outgoing $\hat{\mathbf{e}}_n$, which guarantees us a correct assessment of the solvent density profile within the PSC, as we show in Fig. 5.2(c).

To summarize this section, here we report the complete set of collision rules controlling the solvent-PSC coupling in our simulations, which are illustrated in Fig. 5.3:

- Case 1. From the bulk to the PSC shell ($r_{\text{old}} > R_{\text{colloid}} > r_{\text{new}} > R_{\text{core}}$): if the move is rejected, then a collision takes place at $R_{\text{collision}} = R_{\text{colloid}}$;
- Case 2. From the outer PSC shell to the inner PSC shell ($R_{\text{colloid}} > r_{\text{old}} > r_{\text{new}} > R_{\text{core}}$): if the move is rejected, then a collision takes place at $R_{\text{collision}} = (r_{\text{new}} + r_{\text{old}})/2$;
- Case 3. From the star corona PSC shell to the core ($R_{\text{colloid}} > r_{\text{old}} > R_{\text{core}} > r_{\text{new}}$): the move is rejected, then a collision takes place at $R_{\text{collision}} = R_{\text{core}}$;
- Case 4. From the inner PSC shell to the outer PSC shell ($R_{\text{colloid}} > r_{\text{new}} > r_{\text{old}} > R_{\text{core}}$): if the move is rejected, then a collision takes place at $R_{\text{collision}} = (r_{\text{new}} + r_{\text{old}})/2$;
- Case 5. From the PSC shell to the bulk ($r_{\text{new}} > R_{\text{colloid}} > r_{\text{old}} > R_{\text{core}}$): if the move is rejected, then a collision takes place at $R_{\text{collision}} = (r_{\text{new}} + r_{\text{old}})/2$.

Note that for the case of a linear polymer $R_{\text{core}} = 0$, and therefore, Case 3 is not considered. In all cases where the collision occurs, linear and angular momentum exchanges take place according to Eqs. (5.7)–(5.9). In this case, the position of the solvent particles after the collision will not be described by the ballistic motion represented in Eq. (2.9), but rather by:

$$\mathbf{r}_i(t+h) = \mathbf{r}_i(t) + \frac{h}{2} \mathbf{v}_i(t+h). \quad (5.11)$$

On the other hand, during the displacement of the soft colloid, it is possible that solvent particles remain inside the core. To avoid this, before applying the collision step, we displace the solvent particle by means of:

$$\mathbf{r}_i(t) = \mathbf{R}(t) + \mathcal{R}\lambda + R_{\text{core}} \quad (5.12)$$

where λ is the mean free path of a solvent particle, defined as $\lambda \sim h\sqrt{T}$.

5.3 Results

5.3.1 Monomer and solvent density profiles

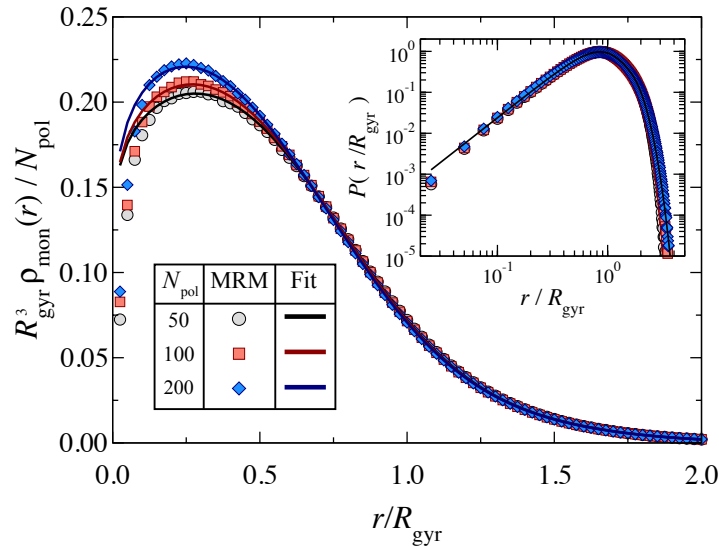


Figure 5.4. Monomer density profile $\rho_{\text{mon}}(r)$ around the center of mass of a linear polymer. Fits are performed with Eq. (5.14). *Inset:* Corresponding monomer probability density distribution. Only the fitting curve for $N_{\text{pol}} = 50$ is shown.

First, we report results for the monomer density profiles for linear and star polymers, obtained from the monomer-resolved simulations, which are shown in Figs. 5.4 and 5.5. These are the key observables that are needed to implement our MD-MPCD framework for soft colloids and it is important to provide an analytic description for them, which can then be employed in the PSC model. To this end, we fit them using a combination of appropriate functions, that are based on known properties of polymers with excluded volume interactions immersed in a good solvent, and which take into account the normalization condition in Eq. (5.3).

For linear chains we consider that

$$\rho_{\text{mon}}^{(\text{chain})}(r) = \frac{N_{\text{pol}}}{R_{\text{gyr}}^3} \cdot \frac{P(r/R_{\text{gyr}})}{4\pi(r/R_{\text{gyr}})^2}, \quad (5.13)$$

where R_{gyr} is the polymer radius of gyration (see Appendix 5.5) and $P(x)$ is the probability distribution to find one monomer of the polymer chain to be located at a scaled distance $x = r/R_{\text{gyr}}$ from its center of mass. Following the analysis of the end-to-end distribution length for a chain with excluded-volume [126, 127], we consider the probability distribution to be given by the expression,

$$\begin{aligned}
 P(x) = & a_0 x^{a_1} \exp\left[-\left(\frac{x}{a_2}\right)^{a_3}\right] f_b(x, x_b) \\
 & + a_4 [1 - f_b(x, x_b)] \exp\left[-\left(\frac{x}{a_5}\right)^2\right].
 \end{aligned}
 \tag{5.14}$$

Here the bridge function

$$f_b(x, x_b) = \exp\left[-\left(\frac{x}{x_b}\right)^4\right],
 \tag{5.15}$$

has been chosen to take into account both the short- and the long-distance behaviour of $P(x)$. The set of parameters $\{a_i, x_b\}$ ($i = 0, \dots, 5$) is then obtained from a non-linear fitting procedure and is reported in Table 5.1.

Table 5.1. Fit parameters to Eq. (5.14) for different polymerization degrees of linear chains.

N_{pol}	a_0	a_1	a_2	a_3	a_4	a_5	x_b
50	3.0806	2.1109	0.8562	2.4880	5.1575	1.0177	1.5508
100	3.2537	2.1225	0.8512	2.3594	3.6011	1.0659	1.4585
200	3.5738	2.1377	0.8210	2.1591	3.0437	1.0940	1.4360

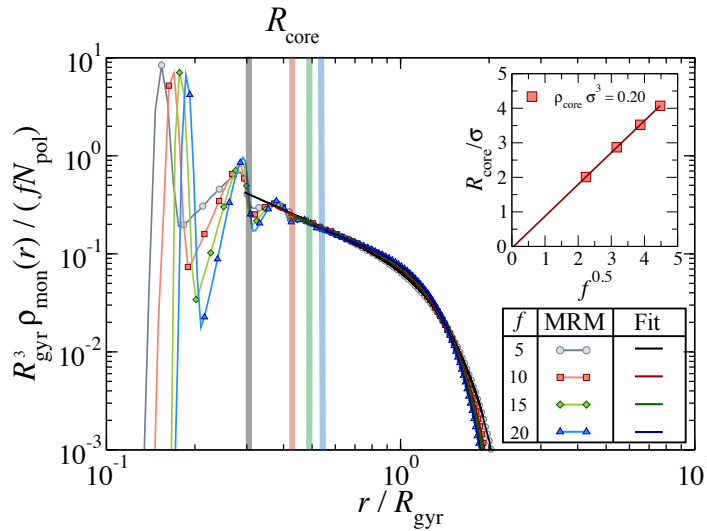


Figure 5.5. Monomer density profile around the center of a star polymer of different functionality f are calculated from simulations (symbols) and compared to fits (lines) based on Eq. (5.16) for $r > R_{\text{core}}$. Vertical lines identify the radius of the core, R_{core} , for each value of f . Inset: R_{core} as a function of $f^{1/2}$ for $\rho_{\text{core}} \sigma^3 = 0.2$.

On the other hand, Fig. 5.5 displays the monomer density profiles obtained for star polymers, for which the fitting procedure is performed as follows. According to the Daoud-Cotton model, the monomer concentration around the center of the star scales as $r^{-4/3}$ at intermediate distances

5 MPCD FOR A COARSE-GRAINED MODEL OF SOFT COLLOIDS

Table 5.2. Fit parameters to Eq. (5.16) for star polymers with different functionality f .

f	A_1	A_2	x_1	x_2	x_b
5	0.0810	0.7975	0.0540	0.4087	1.4276
10	0.0785	0.7400	0.0003	0.5815	1.4054
15	0.7742	0.7342	0.0184	0.6193	1.3845
20	0.0763	0.6350	0.0307	0.6607	1.3380

(swollen regime) [123]. Beyond this scaling regime, there always exists a diffuse layer of polymer which we consider to follow Gaussian decay [128]. Under these assumptions, the monomer density profiles obtained from the MRM simulations are fitted to the expression

$$\rho_{\text{mon}}^{(\text{star})}(r) = \frac{f N_{\text{pol}}}{R_{\text{gyr}}^3} \left(A_1 x^{-4/3} f_b(x, x_b) + A_2 [1 - f_b(x, x_b)] \exp \left[- \left(\frac{x - x_1}{x_2} \right)^2 \right] \right), \quad (5.16)$$

with $x = r/R_{\text{gyr}}$ and $f_b(x, x_b)$ the bridge function defined in Eq. (5.15).

We evaluate the set of parameters $\{A_i, x_i, x_b\}$ ($i = 1, 2$) by fitting only the region $R_{\text{min}} < r < R_{\text{colloid}}$, where R_{colloid} is defined from the condition $\rho_{\text{mon}}^{(\text{star})}(r > R_{\text{max}}) \sigma^3 < 10^{-3}$, while R_{min} is chosen to discard the profile oscillations close to the star center that are indicative of the core region.

Once the parameters defining Eq. (5.16) are obtained for a particular value of f , we impose the scaling $R_{\text{core}} \sim f^{1/2} \sigma$ and the constant density condition inside the core for all other stars to determine the value of R_{core} in all cases, as shown in the inset in Fig. 5.5. We thus extend the fitting curve, Eq. (5.16), also for $R_{\text{core}} < r < R_{\text{min}}$ and set it to zero for $r < R_{\text{core}}$. In the present study we consider $\rho_{\text{core}} \sigma^3 = 0.2$, while we present a discussion on the influence of the core size on the dynamical behavior in Sec. 5.3.4. The final fit parameters used for $\rho_{\text{mon}}^{(\text{star})}(r)$ are reported in Table 5.2.

Using the monomer density profiles as input, we must check that the solvent density profiles obtained with the MPCD-PSC approach are the same as expected. This is illustrated in Fig. 5.6(a) for linear chains and in Fig. 5.6(b) for star polymers. We find that, for all studied cases, $\rho_{\text{sol}}(r)$ are well reproduced by the PSC description. Only we notice that, for star polymers, small deviations appear at large distances with respect to the theoretical predictions of Eq. (5.2), that are more evident for increasing f . These are due to finite size effects, since our simulation box is fixed, while the size of the colloid increases with f .

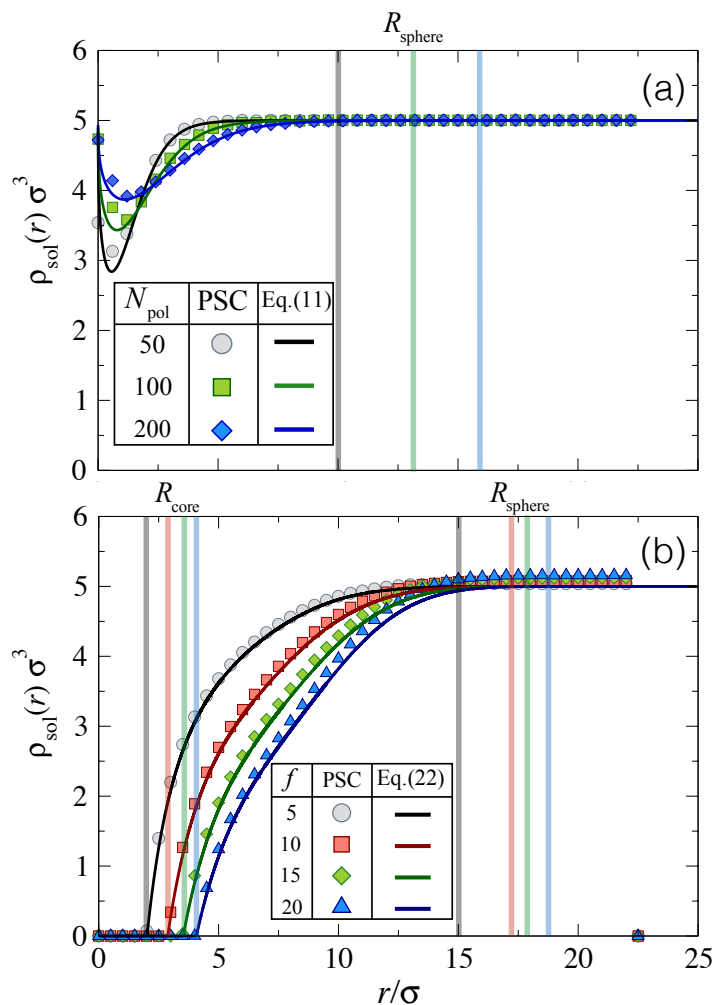


Figure 5.6. Solvent density profile $\rho_{\text{sol}}(r)$ obtained by PSC simulations for (a) linear chains and (b) star polymers.

5.3.2 Results for linear chains

In Appendix 5.5, the corresponding average size, mass, and moment of inertia for both linear and star polymers are presented. Using these quantities along with the fitted monomer density profiles, it is now possible to compare the mean-square displacement and the long-time diffusivity obtained from the two methods for MPCD of soft colloids with those calculated with monomer-resolved simulations (MRM). Here we stress that for all three methods, the properties of the MPDC solvent are identical, i.e., same m , $\langle N_c \rangle$, h , a , and χ . We start by reporting results for linear polymers.

The mean square displacement (MSD) of the polymer center of mass (COM) was evaluated for

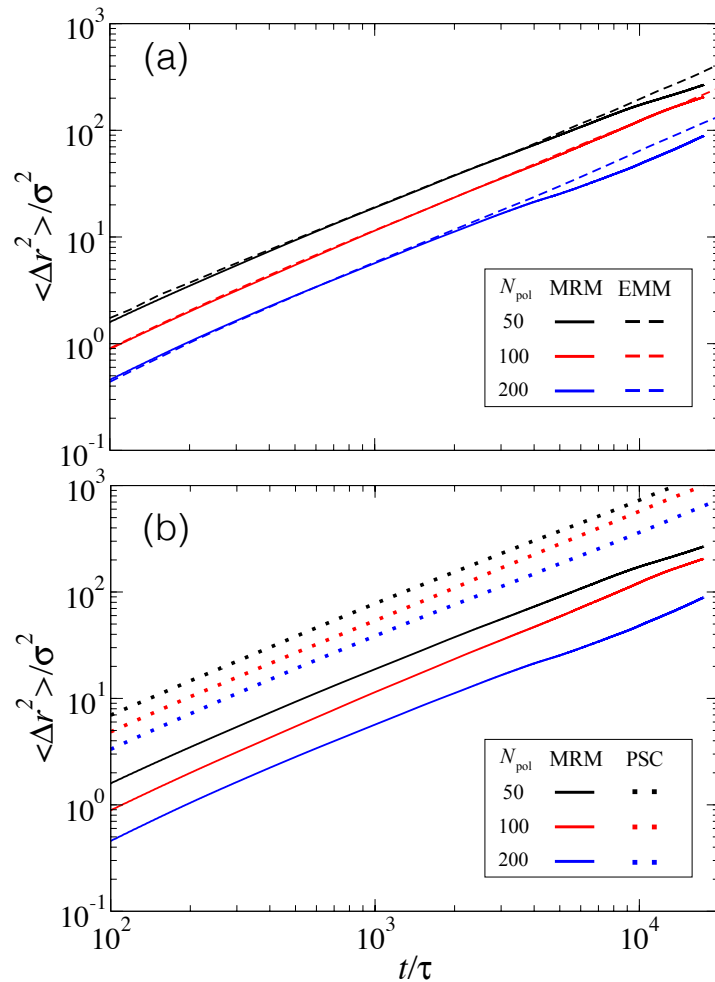


Figure 5.7. Mean-square displacement for linear chains. Results obtained by the MRM model are compared with (a) the description of effective monomers (EMM) and (b) the PSC model.

both types of simulations as

$$\langle \Delta r^2 \rangle = \langle [\mathbf{R}_{\text{com}}(t) - \mathbf{R}_{\text{com}}(0)]^2 \rangle, \quad (5.17)$$

where $\mathbf{R}_{\text{com}}(t)$ is the position of the polymer center-of-mass. The MSD for linear chains is reported in Fig. 5.7 for the effective monomers model and for the PSC model at all studied values of the degree of polymerization. They are compared with the results of MRM simulations. We can clearly see how the effective monomer description is able to reproduce well the MSD obtained by MRM model at all times, while the PSC model is found to always overestimate the diffusion for all values of N_{pol} .

Following Einstein's relation, at sufficiently long times the MSD curves reach a diffusive regime, from which we can compute the finite-size diffusion coefficient $D_L^H \sim \langle \Delta r^2 \rangle / 6t$, where L denotes

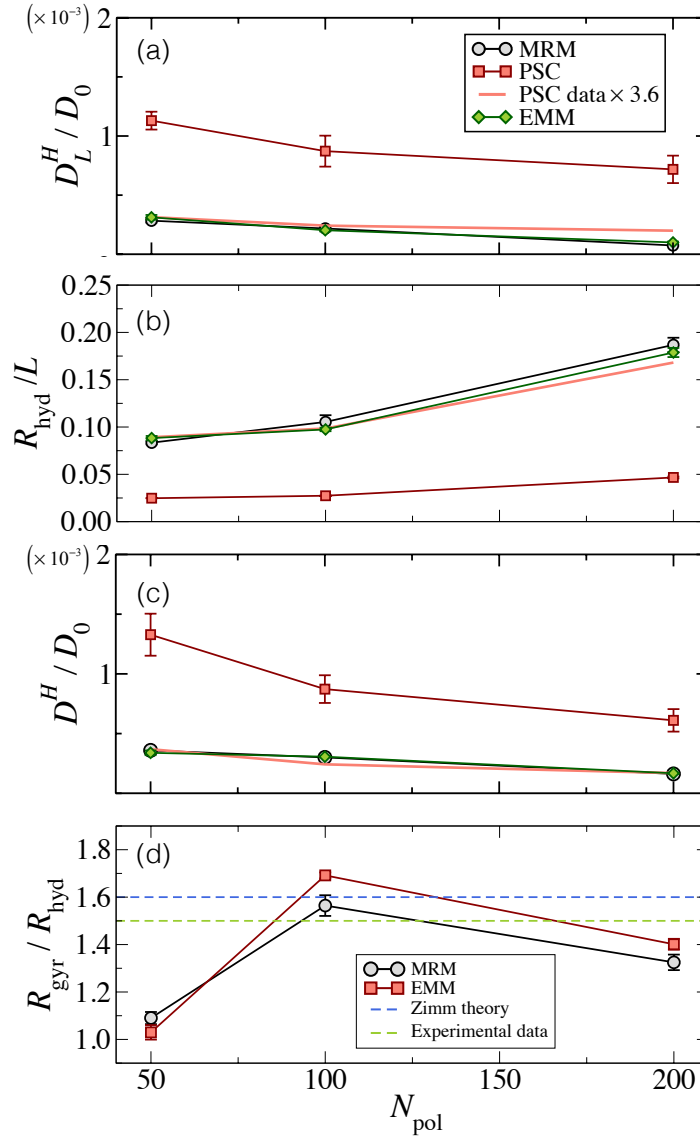


Figure 5.8. Results for linear chains as a function of N_{pol} . (a) Finite-system size D_L^H diffusion coefficient, (b) hydrodynamic radius computed by Eq. (5.18) and (c) infinite-system-size D^H diffusion coefficient. (d) Relationship between the hydrodynamic radius R_{gyr} and the radius of gyration R_{hyd} . The Zimm predictions and experimental values are taken from [96] and refer to linear chains in good solvent conditions. In panels (b-d) the PSC have also been multiplied by the arbitrary factor 3.6, which yields results comparable to those obtained by MRM and EMM simulations.

the size of the simulation box. The corresponding results are reported in Fig. 5.8(a) for chains as a function of degree of polymerization, again comparing the results from the three sets of simulations. There $D_0 = \sqrt{k_B T \sigma^2 / m}$ defines the unit of the diffusion coefficient. Once the finite-system-size diffusion coefficient is known, the hydrodynamic radius R_{hyd} of the soft colloid can be evaluated

5 MPCD FOR A COARSE-GRAINED MODEL OF SOFT COLLOIDS

by inverting the following relationship, as shown by [singh2014hydrodynamic](#):

$$D_L^H = \frac{k_B T}{6\pi \eta_{\text{sol}} R_{\text{hyd}}} \left[1 - \frac{R_{\text{hyd}}}{L} \left(2.837 - \frac{4\pi R_{\text{hyd}}^2}{3 L^2} \right) \right], \quad (5.18)$$

The obtained values of R_{hyd} using this method are reported in Fig. 5.8(b). With these values, we can finally calculate the infinite-system-size diffusion coefficients D_H from the Stokes-Einstein relationship as:

$$D^H = \frac{k_B T}{6\pi \eta_{\text{sol}} R_{\text{hyd}}}. \quad (5.19)$$

The corresponding results for D_H are reported in Fig. 5.8(c). As expected, we find that chains slow down with increasing N_{pol} for all employed simulation methods. However, while the effective monomers simulations seem to reproduce quite well the behavior of the MRM ones for D_L^H and consequently also for R_{hyd} and D^H , the PSC simulations show quantitative deviations. In particular, both diffusion coefficients are significantly overestimated. This results in a smaller value of R_{hyd} , as shown in Figs. 5.8(b). This quantitative discrepancy may be due to the fact that we assume a spherically-symmetric monomer distribution in the model, which is not very accurate for linear chains. However, we notice that a multiplication of the data by the arbitrary factor 3.6 gives results in agreement with the MRM simulations also for the PSC model.

In Fig 5.8(d) we report the ratio $R_{\text{gyr}}/R_{\text{hyd}}$ using the data from MRM simulations and effective monomers model and we compare our findings to the theoretical value predicted by the Zimm model and to available experimental data in good solvent conditions [96]. We observe a similar behavior for both models, with a larger deviation from the expected values for short chains. On the hand, the long chains are seen to be quite close to the theoretical and experimental values.

5.3.3 Results for star polymers

We report the MSD of the star polymers centers of mass in Fig. 5.9 for the effective monomers model (a) and for the PSC model (b) at all studied values of the functionality. The results are compared with those obtained from MRM simulations. We find that the dynamics of the stars in the MRM is more complex than that of the two coarse-grained models, showing clear deviations at short time-scales due to the additional monomeric degrees of freedom, that are absent in both EMM and PSC descriptions. However, at sufficiently long times, when the MRM model reaches the diffusive regime the results become comparable to the coarse-grained approaches. We find that, oppositely to the case of linear chains, the MSD obtained with the PSC model agrees rather well with the MRM description, while the effective monomer model is found to underestimate diffusion for all values of f .

From the long-time diffusive regime, we obtain D_L^H , R_{hyd} and D^H for stars, which are reported

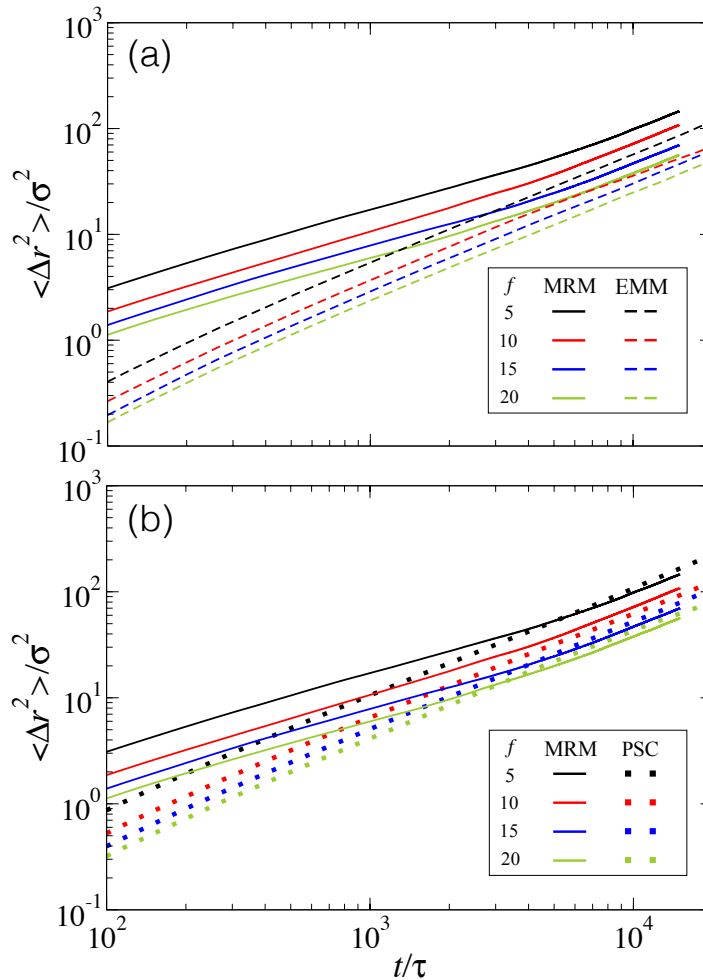


Figure 5.9. Mean-squared displacements for star polymers. Results obtained by MRM model are compared with (a) the description of effective monomers and (b) the PSC model.

in Fig. 5.10. As anticipated from the behavior of the MSD, we now find an opposite behavior of the coarse-grained models with respect to the linear chains simulations. Indeed, for stars we have that the PSC model reproduces quite well the (long-time) trends observed in the MRM simulations with an almost quantitative agreement, while the effective monomer model yields less satisfactory results. This quantitative discrepancy may be due to the fact that we assume a spherically-symmetric monomer distribution in the model, which is not very accurate for linear chains. Instead, the approximation of a spherical density profile for star polymers is a more realistic assumption, particularly with increasing f , for which fluctuations around the spherical density profile are reduced, and hence, it is expected that in the limit of $f \rightarrow \infty$ the PSC should get closer and closer to the MRM results. Indeed, the instantaneous configurations of linear polymer chains are much more akin to ellipsoids with three very dissimilar semiaxes, a feature that has, e.g., been

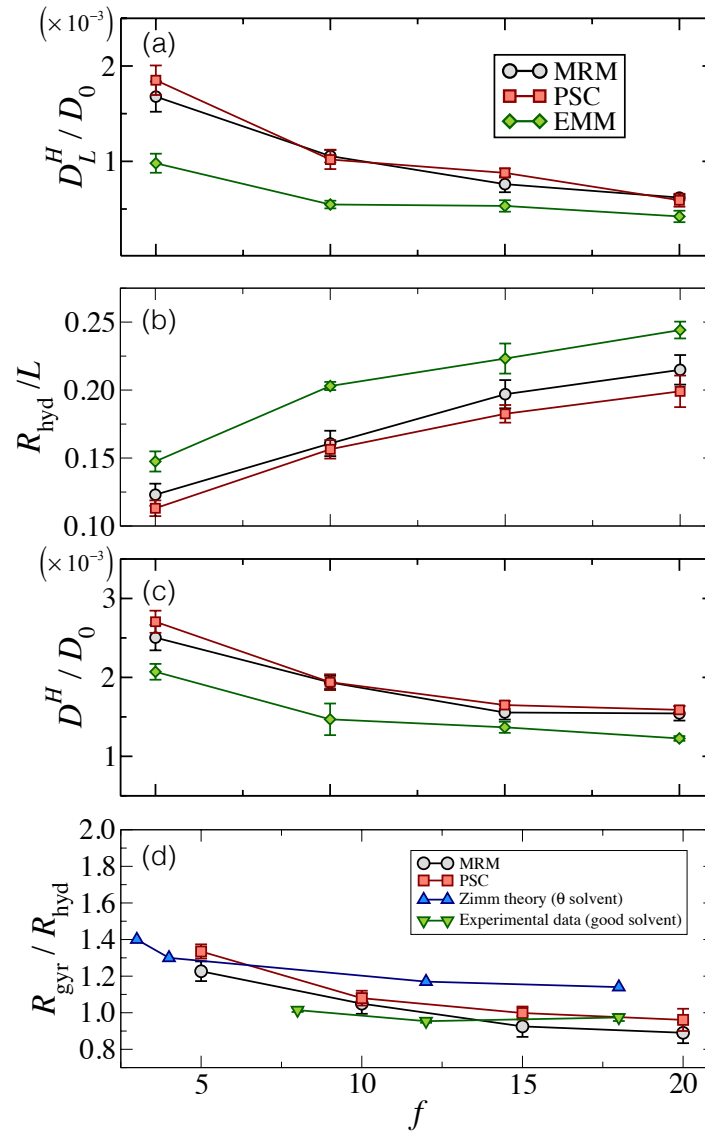


Figure 5.10. Results for star polymers as a function of f . (a) Finite-system size D_L^H diffusion coefficient, (b) hydrodynamic radius calculated via Eq. (5.18) and (c) infinite-system-size D^H diffusion coefficient. (d) Relationship between the hydrodynamic radius R_{gyr} and the radius of gyration R_{hyd} . The Zimm predictions in θ solvent conditions are taken from [96], whereas experimental values are taken from [129] and refer to star polymers in good solvent conditions.

recently exploited to investigate polymer anisotropy effects of the depletion potential they induce on nonadsorbing colloidal particles [130].

As for the case of linear chains, we also report the ratio $R_{\text{gyr}}/R_{\text{hyd}}$ using the data from MRM simulations and effective monomers model in Fig. 5.10(d). The data are compared to the Zimm theory for θ solvent conditions [96], as well as to experimental results for low-arm stars in good solvent [129]. We find a good agreement between the values obtained with both types of simulations and those found in the literature.

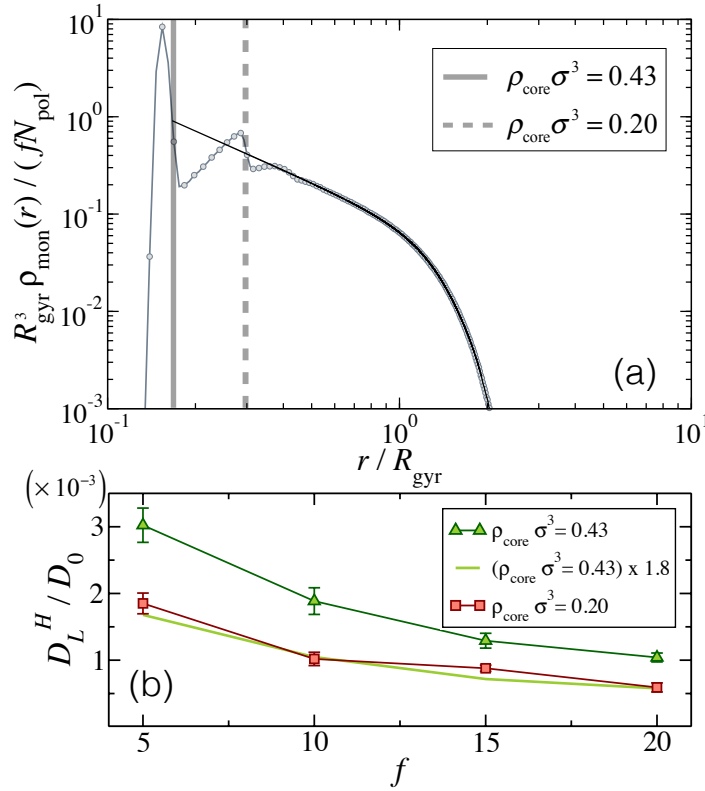


Figure 5.11. (a) Monomer density profile around the central monomer of a star polymer with $f = 5$. Symbols represent data obtained by MRM simulations, whereas solid line indicates the fitting with Eq. (5.16). (b) Finite-system size D_L^H diffusion coefficient as a function of f for two different values of ρ_{core} . The green line refers to the data obtained for a core density $\rho_{\text{core}}\sigma^3 = 0.43$ arbitrarily multiplied by a factor 1.8.

5.3.4 Effects of core on the dynamics of the penetrable soft colloid model for star polymers

We finally describe the influence of the core size on the dynamics of the penetrable soft colloid model. Starting from the fits already discussed in Section 5.3.1, we now consider the effect of extending the validity of the functional form given by Eq. (5.16) into the region where oscillations of the density profile are observed. This is illustrated in Fig. 5.11(a), where we consider stars with $\rho_{\text{core}}\sigma^3 = 0.43$ amounting to a smaller value of R_{core} with respect to the case previously considered in Fig. 5.5 (where $\rho_{\text{core}}\sigma^3 = 0.20$). Having chosen this value of ρ_{core} , we then impose that the core density has the correct scaling with respect to the number of arms ($\sim f^{1/2}$).

In Fig. 5.11(b), we thus compare the values of the finite-system size D_L^H diffusion coefficient for both values of ρ_{core} . We find, as expected, that a decrease in the core radius has the effect to speed up the diffusion of the soft colloid. However, we notice that this is just a quantitative effect. Indeed, we can reconcile both behaviors through a simple multiplication of the data obtained for $\rho_{\text{core}}\sigma^3 = 0.43$ by a factor 1.8, which yields results in good agreement with the previous case. Thus,

an optimal choice of R_{core} is needed for a correct description of the hydrodynamic interactions in our MPCD PSC simulations but its exact value only has qualitative effects.

5.4 Conclusions

With respect to previous works where hydrodynamic interactions of hard sphere particles have been studied using MD-MPCD simulations, in this paper we treat the case of penetrable soft colloids, focusing on linear and star polymers. To this aim, we complement simulations where the polymeric object is treated with a monomer-resolved model, with two novel approaches.

In the first one, we reproduce the structure of the linear chains and star polymers by placing monomers at random in the simulation box using the average monomer density profile and considering this set of monomers as a rigid body. Thus, monomer-monomer interactions are neglected and the dynamics of the polymeric objects are only controlled by the MPCD collision step. On the other hand, in the second model, we adopt a coarse-grained strategy where we use the average monomer density profile of the particle to define it as a penetrable soft colloid surrounded by an inhomogeneously distributed solvent. To capture the hydrodynamic interactions of the penetrable soft colloid, we built on a previous model for MPCD of hard colloids to couple the dynamics of solvent to that of the soft colloid. Differently, from the standard MD-MPCD approach where only an exchange of linear momentum is considered, we now need to control the distribution of solvent with respect to the penetrable sphere. Assuming the form of the solvent density profile, we define the probability rules of the solvent particles displacements. Thus, in all cases where a solvent particle cannot displace, it collides with an inner layer/with the shell of the colloid exchanging both linear and angular momenta.

We find that the hydrodynamic interactions of linear chains are well captured by a fictitious rigid topology, while the approximation of a spherically-symmetric monomer distribution in the PSC approach provides an unsatisfactory description of the data. However, in the case of star polymers, we have the reverse situation: the PSC model with a radial monomer distribution works well, while the representation of the structure by effective monomers does not reproduce the long-time hydrodynamic behavior. This result indicates that macromolecules with a complex internal structure exhibit a more sophisticated solvent-monomer dynamics coupling and that monomer-monomer interactions need to be included at some level in the coarse-grained description. In this respect, the newly-defined collision rules which provide the correct inhomogeneous density profile for solvent particles inside the colloid are able to realistically represent the flow of solvent particles from the interior of the PSC to the bulk, and hence, by the exchange of both linear and angular momenta, to correctly reproduce hydrodynamic interactions. In the case of star polymers, we also find that the definition of the core size can be further tuned to determine the correct long-time dynamics of the penetrable soft colloid.

5 MPCD FOR A COARSE-GRAINED MODEL OF SOFT COLLOIDS

It is now important to comment on the computational efficiency of the new methods that we have proposed. To this aim we perform the simulation of 1000 time steps for a star with $f = 20$ with all three approaches on a 2.9 GHz i5 processor. For the MRM model, such simulation required 5 minutes. On the other hand, for the effective monomers approach it was completed in 3.3 minutes, while the PSC description needed 4 minutes. Hence, both approaches are much more efficient than the MRM model, as expected. This confirms that the numerical techniques that we have introduced in this work could be a first step to investigate the hydrodynamics of complex macromolecules that cannot be attained with MRM simulations. It is our intention to apply this approach to the study of other polymeric systems, such as microgels [131, 132], for which accurate monomer density profiles have recently been calculated at different solvophobic conditions [133]. Furthermore, this method opens up the possibility to go beyond single-particle studies and to address the dynamics of polymeric objects at finite concentrations. One straightforward extension would be to study star polymers with a large number of arms and to address their phase behavior. In this case, two such PSCs would interact by well-established effective star polymer interactions [103], while solvent particles would collide with the soft spheres as described in this work to correctly capture hydrodynamic interactions. Finally, it would be interesting to apply the PSC description to the sedimentation of ultrasoft colloids [134] or star polymers under shear flow [83], where external forces deform the monomeric density profile.

5.5 Appendix 5A: Radius of gyration and moment of inertia

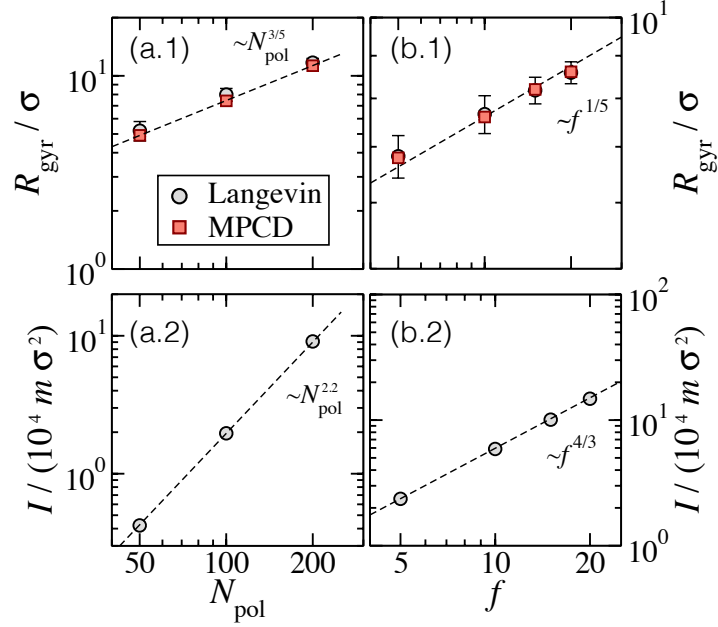


Figure 5.12. (a.1) Radius of gyration R_{gyr} , and (a.2) inertia moment I for linear polymers. (b.1) Radius of gyration R_{gyr} and (b.2) inertia moment I . Numerical results are obtained from MD simulations combined with implicit (Langevin) and explicit (MPCD) solvent.

Here we report results for observables that quantify the polymer conformation, calculated with MRM, that are useful to compare with the PSC simulations. In particular, we focus on the radius of gyration

$$R_{\text{gyr}} = \left\langle \frac{1}{N_{\text{mon}}} \sum_{i=1}^{N_{\text{mon}}} (\mathbf{r}_i - \mathbf{R}_{\text{com}})^2 \right\rangle^{1/2} \quad (5.20)$$

and on the inertia moment around the center of mass

$$I_{zz} = \left\langle M \sum_{i=1}^{N_{\text{mon}}} (x_i^2 + y_i^2) \right\rangle. \quad (5.21)$$

The average values of R_{gyr} and $I = \langle I_{\mu\mu} \rangle = (I_{xx} + I_{yy} + I_{zz})/3$ for linear and star polymers are reported in Tables 5.3 and 5.4, respectively. We also estimate the ‘colloidal’ radius of each macromolecule, named R_{colloid} , as the largest average distance from the COM at which a monomer can be found; it can thus be considered as the size of the penetrable soft colloid model describing the polymer. For the inertia moment, data are normalized by $I_0 = \frac{2}{3} M_{\text{colloid}} R_{\text{gyr}}^2$ with $M_{\text{colloid}} = M N_{\text{mon}}$, which corresponds to the inertia moment of a uniform sphere of mass M_{colloid} and radius

5 MPCD FOR A COARSE-GRAINED MODEL OF SOFT COLLOIDS

$R = \sqrt{5/3}R_{\text{gyr}}$, i.e., both the polymer and the uniform sphere are considered to have the same mass and gyration radius and therefore the same inertia moment. Figure 5.12 shows that R_{gyr} and $\langle I_{\mu\mu} \rangle$ follow the expected scaling laws with respect to the polymerization degree for linear polymers.

Table 5.3. Average sizes and inertia moments of linear polymers. R_{colloid} is chosen such as $P(R_{\text{colloid}}/R_{\text{gyr}}) \leq 10^{-5}$ (see Fig. 5.4).

N_{pol}	R_{gyr}/σ	$R_{\text{colloid}}/R_{\text{gyr}}$	$I_0/(10^4 m\sigma^2)$	$\langle I_{\mu\mu} \rangle/I_0$	$\langle I_{\mu\nu} \rangle/I_0$
050	5.25	3.32	0.4507	0.9352	-0.00055
100	8.00	3.50	2.1280	0.9224	-0.00302
200	11.70	3.61	9.1103	0.9991	-0.00820

Table 5.4. Average sizes and inertia moments of star polymers. R_{colloid} is chosen such as $\rho_{\text{mon}}(r > R_{\text{colloid}}) \leq 10^{-3}$ (see Fig. 5.5).

f	N_{pol}	R_{gyr}/σ	$R_{\text{colloid}}/R_{\text{gyr}}$	$I_0/(10^4 m\sigma^2)$	$\langle I_{\mu\mu} \rangle/I_0$	$\langle I_{\mu\nu} \rangle/I_0$
5	30	6.82	2.68	2.3257	1.0145	-0.00134
10	30	7.66	2.50	5.8675	1.0048	-0.00446
15	30	8.18	2.45	10.036	1.0042	0.00413
20	30	8.59	2.37	14.758	1.0027	-0.00023

Similarly, Fig. 5.12 reports the same quantities for star polymers, showing that they follow the expected scaling laws with respect to the functionality. In both cases, simulations performed with implicit (MD+Langevin) and with explicit (MD+MPCD) solvent yield the same results.

6 | Conclusion and Outlook

This Dissertation presents a detailed study of the properties, both in equilibrium and under the influence of a shear flow, of Star Block Copolymer (SBC) suspensions, considering the latter as versatile representatives of "self-associative polymers". It has been demonstrated that SBCs present both intramolecular and intermolecular association phenomena. SBCs behave as soft particles with self-associative clusters. The number of clusters and their extension can be modified by means of SBC parameters, namely functionality, temperature, solvent quality, and the fraction of the solvophobic monomer. By employing computational modeling that allows covering a wide range of physical-chemical parameters characteristic of these systems, the Dissertation starts with the analysis of the behavior of an isolated SBC under different conditions and then extends the study to polymer concentrations in diluted and concentrated regimes.

For the case of the isolated polymer, studied in *chapter 3*, its conformational characteristics were analyzed in detail. We found great variety in the global geometric distribution of the polymer shape, which in equilibrium is determined by the number of patches that can be formed by self-association in the SBC, which is in turn determined by the ratio of sizes of copolymer subunits in each arm of the SBC, the quality of the solvent and/or the temperature. A global recurrent form is that possessing spherical symmetry, which is linked to stars capable of forming a number of clusters greater than 3 or with a behavior close to that of purely repulsive stars (athermal star polymers). On the other hand, for the SBC that tends to form 2 patches, a cylindrical symmetry associated to a configuration similar to a Cuban cigar prevails, with its tips being occupied by solvophobic groupings. Once having these characteristics established in equilibrium, we proceeded to study the change in the global geometric conformation of SBC as a function of the deformation rate (shear rate) of the solvent. In these conditions the SBC deforms as a function of the shear rate, elongating in the direction of flow, contracting around the direction of the gradient and without significant deformation in the direction of vorticity, behavior that is shared with other "super-soft particles", such as linear polymers, ring polymers.

From the dynamic point of view, we carried out a detailed study of the polymer rotational dynamics under the influence of the shear flow, choosing for this purpose three representative systems in equilibrium, namely, (i) SBCs with a behavior similar to that of purely repulsive stars, (ii) SBCs with a mixed behavior, in which some arms are self-associated while others remain free, and finally, (iii) SBCs characterized by the formation of two groupings without free arms. We carried out the study comparing rotational energy and rotation frequency resulting from four different theoretical approaches. The first is the one known as the laboratory approach in which rigid body formalism is used; the second corresponds to the geometric approach, which considers that the velocity of the monomers is determined solely by the velocity profile of the solvent and that the elements outside the diagonal of the moment of inertia tensor are associated with the

6 CONCLUSION AND OUTLOOK

vibrational movement; thirdly, Eckart's approximation was used, which allows differentiating pure rotational movement from pure vibrational movement, finally, we propose a fourth Hybrid frame approximation, in which a symmetrical turn tensor is used in Eckart's approximation. For each one of the formalisms used we calculate the rotational energy and the rotation frequency, with which we find that the rotation frequency of Eckart's formalism is the highest of all, followed by the geometric, Hybrid frame, and laboratory approximations. Our results show that for all cases the rotation frequency is limited from below by the rotation frequency obtained in the laboratory. For the third significant case, our results show that the rotation frequency corresponds mainly to the shear-flow induced tumbling motion of the SBC. For case two, the rotation frequency results from the average of the tank-treading motion and the clustering and breaking of the patches, and case one shows the same behavior as that of athermal stars.

The last aspect considered in the study of isolated SBC is related to the behavior of the patches as a function of the shear flow. Under certain conditions, such as low values of the solvophobic monomer fraction, the shear flow helps to create a larger number of clusters than those found in equilibrium conditions. On the other hand, for high values of the solvophobic monomer fraction, the shear flow leads to a reduction of the number of clusters, special case for when the SBC has two clusters without free arms we found that the shear flow makes the SBC go from 2 clusters to 1, a fusion of 2 clusters to 1 for high values of the shear flow.

For diluted and concentrated SBC systems, we explore the main properties in equilibrium varying the monomeric density, and the SBC parameters, we find that for high values of the solvophobic monomer fraction a phase separation takes place, whereas for small values the system remains homogeneous. In concentrated systems, the SBCs are reconfigured for the association with other SBC where they recover the spherical form, radially symmetric. Our main result was the study of the connection between stars. The choice of functionality and the fraction of solvophobic monomers leads the system to a network configuration instead of the formation of micelles. Moreover, we found that the systems of SBCs have non-trivial characteristics of self-organized networks, and a variety of the size of the clusters for concentrated systems, where for intermediate values of the fraction of solvophobic monomers we found the effect of homogeneous percolation. The patches are compacted and crystallized for low values of the solvent quality.

When we apply shear flow, we find that the morphology and connectivity of the system are significantly reorganized by the shear rate. When applying the shear flow, each SBC suffers an elongation in the direction of flow while in the other two directions the SBC shrinks, so the patches are divided into smaller clusters, generating more patches but with fewer constituent arms. By increasing the concentration, connectivity between SBC is increased which implies an increase in viscosity. When applying the shear flow, we find shear thinning, is generated by the reorganization of the SBC and the breakage of both the patches and the connections between the SBCs.

Finally, the last part of this research focused on the development of two new numerical al-

6 CONCLUSION AND OUTLOOK

gorithms for the implementation of the hybrid method, i.e., MD molecular dynamics algorithm for polymers/colloids, Multi-Particle Collision Dynamics MPCD for solvent modeling. This hybrid method consists of coupling the polymer/colloid with the solvent employing collision parameters in the MPCD program, applied to the study of polymer suspensions with architectures that can be described through a model of soft colloid spheres. Using as input information the density profile around the center of mass of the monomers that make up the polymer, we propose two new models for the interaction between the soft colloid and the solvent particles within the MPCD technique.

The first model considers a "rigid colloid" constituted by a collection of monomers located randomly following the real distribution of polymer monomers. On the other hand, the second model considers a non-homogeneous distribution of the solvent particles around the polymer, which is defined by the actual monomer profile of the polymer monomers. In the first case, satisfactory results are obtained for the diffusive behavior of linear polymers, while with the second model we find a good description of this behavior for purely repulsive stars when the results of the proposed models are compared with simulations made at the detail level of the monomers.

The study could be extended having several considerations exposed here: (i) a more detailed study of the fluid behavior could be made, calculating velocity and pressure fields, and how these change according to the presence of isolated SBC and systems in semi-dilute and concentrated regimes. As well an explicit calculation of the hydrodynamic force as a consequence of the interaction between the solvent and the SBC in the collision step of the MPCD algorithm. (ii) To better understand the dynamics of the patches, arms detachment and reattachment in a patch, both in equilibrium and when the shear flow is applied, where the lifetime in average of the patches could be calculated. In the same way, the calculation of the minimum energy for a stable cluster could be achieved. Establish a more detailed description concerning the statistics of the typical times between the events detachment and reattachment. (iii) The protocol for the initial configuration could be changed for the diluted, semi-diluted, and concentrated regimes. In the first part of the protocol, it would be to use the algorithm for the SBC, generating an isolated system of SBC with well-defined patches with implicit solvent. In the second part of the protocol, the reduction of the simulation box is sought until arriving at the appropriate density to have an interacting system of SBCs, in the last part of the protocol, the implicit solvent is introduced, and it is sought if the system persists some organized structure. (iv) Calculation of other properties of the SBC systems in shear flow, such as the elastic and viscous modulus, as well as complementing the study in the semi-diluted and concentrated regimes with the calculation of the first and second normal stress differences in steady shear flow.

Bibliography

- [1] DAVID ANDELMAN W.C.K. POON. *Introduction: Coarse graining in biological soft matter*. Boca Raton: CRC Press, 2006.
- [2] DIMITRIS VLASSOPOULOS and GEORGE FYTAS. In: *From Polymers to Colloids: Engineering the Dynamic Properties of Hairy Particles*. vol. 236, 1–54. Springer, Berlin, Heidelberg, 2010.
- [3] MASAO DOI. *Soft Matter Physics*. OUP Oxford, 2013.
- [4] RONALD BLAAK, BARBARA CAPONE, CHRISTOS N LIKOS and LORENZO ROVIGATTI. In: *Accurate coarse-grained potentials for soft matter systems*. vol. 28, 209–258. Forschungszentrum Jülich, 2015.
- [5] B. LONETTI, M. CAMARGO, J. STELLBRINK, C.N. LIKOS, E. ZACCARELLI, L. WILLNER, P. LINDNER and D. RICHTER. *Physical review letters*, **106**, 228301, (2011).
- [6] DOMINIC A LENZ, RONALD BLAAK and CHRISTOS N LIKOS. *Journal of Physics: Condensed Matter*, **24**, 284119, (2012).
- [7] A. MALEVANETS and R. KAPRAL. *J. Chem. Phys.*, **110**, 8605–8613, (1999).
- [8] A. MALEVANETS and R. KAPRAL. *J. Chem. Phys.*, **112**, 7260–7269, (2000).
- [9] ARTURO NARROS, ANGEL J. MORENO and CHRISTOS N. LIKOS. *Soft Matter*, **6**, 2435, (2010).
- [10] P. POIER, CHRISTOS N. LIKOS, MORENO ANGEL J. and BLAAK RONALD. *Macromolecules*, **14**, 4983, (2015).
- [11] J. STELLBRINK, B. ABBAS, J. ALLGAIER, M. MONKENBUSCH, D. RICHTER, C. N. LIKOS, H. LÖWEN and M. WATZLAWEK. ‘Structure and dynamics of star polymers’ in: *Trends in Colloid and Interface Science XII*. ed. by G. J. M. KOPER, D. BEDEAUX, C. CAVACO and W. F. C. SAGER Darmstadt: Steinkopff, 1998. 25–28
- [12] SEBASTIAN HUISSMANN, RONALD BLAAK and CHRISTOS N. LIKOS. *Macromolecules*, **42**, 2806–2816, (2009).
- [13] ABHIRUP MANDAL, ROHIT BISHT, ILVA D. RUPENTHAL and ASHIM K. MITRA. *Journal of Controlled Release*, **248**, 96–116, (2017).
- [14] BENOIT LOPPINET, GEORGE FYTAS, DIMITRIS VLASSOPOULOS, CHRISTOS N. LIKOS, GERD MEIER and GUO JUN LIU. *Macromolecular Chemistry and Physics*, **206**, 163–172, (2005).

BIBLIOGRAPHY

- [15] MATTHIAS BALLAUFF and CHRISTOS N. LIKOS. *Angewandte Chemie International Edition*, **43**, 2998–3020, (2004).
- [16] C. N. LIKOS, S. ROSENFELDT, N. DINGENOUTS, M. BALLAUFF, P. LINDNER, N. WERNER and F. VÖGTLE. *The Journal of Chemical Physics*, **117**, 1869–1877, (2002).
- [17] ZHENLI ZHANG and SHARON C. GLOTZER. *Nano Letters*, **4**, 1407–1413, (2004).
- [18] ÉTIENNE DUGUET, CÉLINE HUBERT, CYRIL CHOMETTE, ADELIN PERRO and SERGE RAVAINÉ. *Comptes Rendus Chimie*, **19** Emerging Chemistry in France, 173–182, (2016).
- [19] E. BIANCHI, R. BLAAK and C. N. LIKOS. *Phys. Chem. Chem. Phys.*, **13**, 6397–6410, (2011).
- [20] IVAN COLUZZA, PETER D. J. VAN OOSTRUM, BARBARA CAPONE, ERIK REIMHULT and CHRISTOPH DELLAGO. *Soft Matter*, **9**, 938–944, (2013).
- [21] YU-CHUEH HUNG, TING-YU LIN, WEI-TING HSU, YI-WEN CHIU, YU-SHENG WANG and LJILJANA FRUK. *Optical Materials*, **34**, 1208–1213, (2012).
- [22] FAHIMA OUCHEN, GREGORY A. SOTZING, TRISHA L. MILLER, KRISTI M. SINGH, BRIAN A. TELEK, ALYSSA C. LESKO, ROBERTO AGA, EMILY M. FEHRMAN-CORY, PERRY P. YANEY, JAMES G. GROTE, CARRIE M. BARTSCH and EMILY M. HECKMAN. *Applied Physics Letters*, **101**, 153702, 153702, (2012).
- [23] L. ROVIGATTI, B. CAPONE and C. N. LIKOS. *Nanoscale*, **8**, 3288–3295, (2016).
- [24] B. CAPONE, I. COLUZZA, R. BLAAK, F. LO VERSO and C. N. LIKOS. *New J. Phys.*, **15**, 095002, (2013).
- [25] FEDERICA LO VERSO, ATHANASSIOS Z. PANAGIOTOPOULOS and CHRISTOS N. LIKOS. *Phys. Rev. E*, **79**, 010401(R), (2009).
- [26] CHRISTIAN KOCH, CHRISTOS N LIKOS, ATHANASSIOS Z PANAGIOTOPOULOS and FEDERICA LO VERSO. *Mol. Phys.*, **109**, 3049–3060, (2011).
- [27] CHRISTIAN KOCH, ATHANASSIOS Z. PANAGIOTOPOULOS, FEDERICA LO VERSO and CHRISTOS N. LIKOS. *Soft Matter*, **9**, 7424, (2013).
- [28] ESMAEEL MOGHIMI, IURII CHUBAK, ANTONIA STATT, MICHAEL P. HOWARD, DIMITRA FOUNTA, GEORGE POLYMERPOULOS, KONSTANTINOS NTETSIKAS, NIKOS HADJICHRISTIDIS, ATHANASSIOS Z. PANAGIOTOPOULOS, CHRISTOS N. LIKOS and DIMITRIS VLASSOPOULOS. *ACS Macro Letters*, **8**, 766–772, (2019).

BIBLIOGRAPHY

- [29] P. COUSSOT. 'Introduction to the rheology of complex fluids' in: *Understanding the Rheology of Concrete* ed. by NICOLAS ROUSSEL. Woodhead Publishing Series in Civil and Structural Engineering Woodhead Publishing, 2012. 3–22
- [30] T A WAIGH. *Reports on Progress in Physics*, **68**, 685–742, (2005).
- [31] JAN MEWIS and NORMAN J. WAGNER. *Colloidal Suspension Rheology*. Cambridge Series in Chemical Engineering Cambridge University Press, 2011.
- [32] D. VLASSOPOULOS and M. CLOITRE. *Curr. Opin. Colloid Interface Sci.*, **19**, 561–574, (2014).
- [33] MICHAEL RUBINSTEIN and ANDREY V DOBRYNIN. *Trends in Polymer Science*, **5**, 181–186, (1997).
- [34] CHRISTOPHE CHASSENIEUX, TACO NICOLAI and LAZHAR BENYAHIA. *Current Opinion in Colloid & Interface Science*, **16**, 18–26, (2011).
- [35] JING M. REN, THOMAS G. MCKENZIE, QIANG FU, EDGAR H. H. WONG, JIANGTAO XU, ZESHENG AN, SIVAPRAKASH SHANMUGAM, THOMAS P. DAVIS, CYRILLE BOYER and GREG G. QIAO. *Chemical Reviews*, **116** PMID: 27299693, 6743–6836, (2016).
- [36] KEVIN LETCHFORD and HELEN BURT. *European Journal of Pharmaceutics and Biopharmaceutics*, **65** Drug delivery: a Canadian perspective, 259–269, (2007).
- [37] XIAO LI, JAMES IOCOZZIA, YIHUANG CHEN, SHIQIANG ZHAO, XUN CUI, WEI WANG, HAIFENG YU, SHAOLIANG LIN and ZHIQUN LIN. *Angewandte Chemie International Edition*, **57**, 2046–2070, (2018).
- [38] PRASHANT DOGRA, JOE BUTNER, JAVIER RUIZ-RAMÍREZ, YAO-LI CHUANG, ACHRAF NOUREDDINE, CHARLES BRINKER, VITTORIO CRISTINI and ZHIHUI WANG. *Computational and Structural Biotechnology Journal*, **18**, 518–531, (2020).
- [39] YUDI DENG, XUDONG ZHANG, HAIBIN SHEN, QIANGNAN HE, ZIJIAN WU, WENZHEN LIAO and MIAOMIAO YUAN. *Frontiers in Bioengineering and Biotechnology*, **7**, 489, (2020).
- [40] JIFU TAN, ANTONY THOMAS and YALING LIU. *Soft Matter*, **8**, 1934–1946, (2012).
- [41] D. FRENKEL and B. SMIT. *Understanding Molecular Simulation: From Algorithms to Applications*. Academic Press, 2001.
- [42] A. STUKOWSKI. *Modelling Simul. Mater. Sci. Eng.*, **18**, 015012, (2010).
- [43] MARTIN OLIVER STEINHAUSER. *J. Chem. Phys.*, **122**, 094901, (2005).

BIBLIOGRAPHY

- [44] GERHARD ZIFFERER and WERNER PREUSSER. *Macromolecular Theory and Simulations*, **10**, 397–407, (2001).
- [45] DOROS N THEODOROU and ULRICH W SUTER. *Macromolecules*, **18**, 1467–1478, (1985).
- [46] G GOMPPER, T IHLE, DM KROLL and RG WINKLER. ‘Multi-particle collision dynamics: A particle-based mesoscale simulation approach to the hydrodynamics of complex fluids’ in: *Advanced Computer Simulation Approaches for Soft Matter Sciences III*. Springer, 2009. 1–87
- [47] M. RIPOLL, R. G. WINKLER and G. GOMPPER. *Phys. Rev. Lett.*, **96**, 188302, (2006).
- [48] T IHLE and DM KROLL. *Phys. Rev. E*, **63**, 020201, (2001).
- [49] C. C. HUANG, A. CHATTERJI, G. SUTMANN, G. GOMPPER and R. G. WINKLER. *J. Comput. Phys.*, **229**, 168–177, (2010).
- [50] A MALEVANETS and JM YEOMANS. *EPL (Europhysics Letters)*, **52**, 231, (2000).
- [51] K MUSSAWISADE, M RIPOLL, RG WINKLER and G GOMPPER. *J. Chem. Phys.*, **123**, 144905, (2005).
- [52] M. DOI and S. F. EDWARDS. *The Theory of Polymer Dynamics*. Oxford University Press, 1986.
- [53] F. LO VERSO, C. N. LIKOS and H. LÖWEN. *J. Phys. Chem. C*, **111**, 15803–15810, (2007).
- [54] B. CAPONE, I. COLUZZA, F. LO VERSO, C. N. LIKOS and R. BLAAK. *Phys. Rev. Lett.*, **109**, 238301, (2012).
- [55] C. KOCH, A. Z. PANAGIOTOPOULOS, F. LO VERSO and C. N. LIKOS. *Soft Matter*, **11**, 3530–3535, (2015).
- [56] I. WADGAONKAR and A. CHATTERJI. *J. Chem. Phys.*, **146**, 084906, (2017).
- [57] R. G. WINKLER, D. A. FEDOSOV and G. GOMPPER. *Curr. Opin. Colloid Interface Sci.*, **19**, 594–610, (2014).
- [58] I. S. DALAL, A. ALBAUGH, N. HODA and R. G. LARSON. *Macromolecules*, **45**, 9493–9499, (2012).
- [59] I. S. DALAL, N. HODA and R. G. LARSON. *J. Rheol.*, **56**, 305–332, (2012).
- [60] W. CHEN, J. CHEN, L. LIU, X. XU and L. AN. *Macromolecules*, **46**, 7542–7549, (2013).
- [61] W. CHEN, Y. LI, H. ZHAO, L. LIU, J. CHEN and L. AN. *Polymer*, **64**, 93–99, (2015).
- [62] M. RIPOLL, R. G. WINKLER and G. GOMPPER. *Eur. Phys. J. E*, **23**, 349–354, (2007).

BIBLIOGRAPHY

- [63] T. YAMAMOTO and N. MASAOKA. *Rheologica Acta*, **54**, 139–147, (2015).
- [64] A. NIKOUBASHMAN and C. N. LIKOS. *Macromolecules*, **43**, 1610–1620, (2010).
- [65] J. S. MYUNG, F. TASLIMI, R. G. WINKLER and G. GOMPPER. *Macromolecules*, **47**, 4118–4125, (2014).
- [66] F. TASLIMI, G. GOMPPER and R. G. WINKLER. *Macromolecules*, **47**, 6946–6954, (2014).
- [67] J. SABLIC, M. PRAPROTNIK and R. DELGADO-BUSCALIONI. *Soft Matter*, **13**, 4971–4987, (2017).
- [68] J. SABLIC, R. DELGADO-BUSCALIONI and M. PRAPROTNIK. *Soft Matter*, **13**, 6988–7000, (2017).
- [69] S. A. EGOROV, J. PATUREJ, C. N. LIKOS and A. MILCHEV. *Macromolecules*, **46**, 3648–3653, (2013).
- [70] G. S. GREST, K. KREMER and T. A. WITTEN. *Macromolecules*, **20**, 1376–1383, (1987).
- [71] S.T. PARK, J.H. MOON and M.S. KIM. *J. Che. Phys.*, **107**, 9899–9906, (1997).
- [72] Y.M. RHEE and M.S. KIM. *J. Chem. Phys.*, **107**, 1394–1402, (1997).
- [73] C. ECKART. *Phys. Rev.*, **47**, 552, (1935).
- [74] J.D. LOUCK and H.W. GALBRAITH. *Rev. Mod. Phys.*, **48**, 69, (1976).
- [75] D. JANEŠIČ, M. PRAPROTNIK and F. MERZEL. *J. Chem. Phys.*, **122**, 174101, (2005).
- [76] M. PRAPROTNIK and D. JANEŠIČ. *J. Chem. Phys.*, **122**, 174102, (2005).
- [77] M. PRAPROTNIK and D. JANEŠIČ. *J. Chem. Phys.*, **122**, 174103, (2005).
- [78] M. PRAPROTNIK and D. JANEŠIČ. *J. Chem. Inf. Model*, **45**, 1571–1579, (2005).
- [79] C. AUST, S. HESS and M. KRÖGER. *Macromolecules*, **35**, 8621–8630, (2002).
- [80] S.P. SINGH, D.A. FEDOSOV, A. CHATTERJI, R.G. WINKLER and G. GOMPPER. *J. Phys.: Condens. Matter*, **24**, 464103, (2012).
- [81] V. METRI, A. LOUHICHI, J. YAN, G. P. BAEZA, K. MATYJAZEWSKI, D. VLASSOPOULOS and W. J. BRIELS. *Macromolecules*, **51**, 2872–2886, (2018).
- [82] JIN SUK MYUNG, ROLAND G WINKLER and GERHARD GOMPPER. *Journal of Chemical Physics*, **143**, 243117, (2015).
- [83] DIEGO JARAMILLO-CANO, MAUD FORMANEK, CHRISTOS N LIKOS and MANUEL CAMARGO. *The Journal of Physical Chemistry B*, **122**, 4149–4158, (2018).

BIBLIOGRAPHY

- [84] SAMI HIETALA, SATU STRANDMAN, PAULA JARVI, MIKA TORKKELI, KATJA JANKOVA, SØREN HVILSTED and HEIKKI TENHU. *Macromolecules*, **42**, 1726–1732, (2009).
- [85] FEDERICA LO VERSO, CHRISTOS N. LIKOS, CHRISTIAN MAYER and HARTMUT LÖWEN. *Phys. Rev. Lett.*, **96**, 187802, (2006).
- [86] I. C. GÂRLEA, E. BIANCHI, B. CAPONE, L. ROVIGATTI and C. N. LIKOS. *Curr. Opin. Colloid Interface Sci.*, **30**, 1–7, (2017).
- [87] J. T. PADDING, E. S. BOEK and W. J. BRIELS. *J. Phys.: Condens. Matter*, **17**, S3347, (2005).
- [88] J. T. PADDING, W. J. BRIELS, M. R. STUKAN and E. S. BOEK. *Soft Matter*, **5**, 4367, (2009).
- [89] L. RAMOS and C. LIGOURE. *Macromolecules*, **40**, 1248, (2007).
- [90] K. NAKAYA-YAEGASHI, L. RAMOS, H. TABUTEAU and C. LIGOURE. *J. Rheol.*, **52**, 359, (2008).
- [91] C. QUELLET, H.-F. EICKE and W. MEIER. *Macromolecules*, **23**, 3347, (1990).
- [92] M. ODENWALD, H.-F. EICKE and W. MEIER. *Macromolecules*, **28**, 5069, (1995).
- [93] H. BAGGER-JØRGENSEN, L. COPPOLA, K. THURESSON, U. OLSSON and K. MORTENSEN. *Langmuir*, **13**, 4204, (1997).
- [94] JACQUELINE APPELL, GRÉGOIRE PORTE and MICHEL RAWISO. *Langmuir*, **14**, 4409, (1998).
- [95] W. MEIER, J. HOTZ and S. GÜNTHER-AUSBORN. *Langmuir*, **12**, 5028, (1996).
- [96] M. RUBINSTEIN and R. H. COLBY. *Polymer Physics*. Oxford: Oxford University Press, 2003. 53
- [97] EMANUELA BIANCHI, BARBARA CAPONE, GERHARD KAHL and CHRISTOS N. LIKOS. *Faraday Discuss.*, **181**, 123–138, (2015).
- [98] M.P. ALLEN and D.J. TILDESLEY. *Computer Simulation of Liquids*. Oxford Science Publications Clarendon Press, 1987.
- [99] JOHN HORTON CONWAY and NEIL JAMES ALEXANDER SLOANE. *Sphere packings, lattices and groups*. vol. 290 Springer Science & Business Media, 2013.
- [100] N.W. ASHCROFT and N.D. MERMIN. *Solid State Physics*. HRW international editions Holt, Rinehart and Winston, 1976.
- [101] J.K.G. DHONT. *An Introduction to Dynamics of Colloids*. Studies in Interface Science Elsevier Science, 1996. 46

BIBLIOGRAPHY

- [102] CM SORENSEN. *Aerosol Science & Technology*, **35**, 648–687, (2001).
- [103] C. N. LIKOS, H. LÖWEN, M. WATZLAWEK, B. ABBAS, O. JUCKNISCHKE, J. ALLGAIER and D. RICHTER. *Phys. Rev. Lett.*, **80**, 4450, (1998).
- [104] J. S. MYUNG, F. TASLIMI, R. G. WINKLER and G. GOMPPER. *Macromolecules*, **47**, 4118–4125, (2014).
- [105] SUNIL P SINGH, APRATIM CHATTERJI, GERHARD GOMPPER and ROLAND G WINKLER. *Macromolecules*, **46**, 8026–8036, (2013).
- [106] JOHN F BRADY and GEORGES BOSSIS. *Annu. Rev. Fluid Mech.*, **20**, 111–157, (1988).
- [107] RAYMOND KAPRAL. *Adv. Chem. Phys.*, **140**, 89–146, (2008).
- [108] HIROSHI NOGUCHI and GERHARD GOMPPER. *Proc. Nat. Acad. Sci. U.S.A.*, **102**, 14159–14164, (2005).
- [109] HIROSHI NOGUCHI and GERHARD GOMPPER. *Phys. Rev. Lett.*, **93**, 258102, (2004).
- [110] ARASH NIKOUBASHMAN and CHRISTOS N LIKOS. *J. Chem. Phys.*, **133**, 074901, (2010).
- [111] LISA B WEISS, MATTIA MARENDA, CRISTIAN MICHELETTI and CHRISTOS N LIKOS. *Macromolecules*, (2019).
- [112] LISA B. WEISS, ARASH NIKOUBASHMAN and CHRISTOS N. LIKOS. *ACS Macro Lett.*, **6**, 1426–2431, (2017).
- [113] MAXIMILIAN LIEBETREU, MARISOL RIPOLL and CHRISTOS N. LIKOS. *ACS Macro Lett.*, **7**, 447–452, (2018).
- [114] YASUHIRO INOUE, YU CHEN and HIROTADA OHASHI. *J. Stat. Phys.*, **107**, 85–100, (2002).
- [115] ARASH NIKOUBASHMAN, CHRISTOS N LIKOS and GERHARD KAHL. *Soft Matter*, **9**, 2603–2613, (2013).
- [116] E WESTPHAL, SUNIL P SINGH, C-C HUANG, GERHARD GOMPPER and ROLAND G WINKLER. *Comput. Phys. Commun.*, **185**, 495–503, (2014).
- [117] MICHAEL P. HOWARD, ATHANASSIOS Z. PANAGIOTOPOULOS and ARASH NIKOUBASHMAN. *Comput. Phys. Commun.*, **230**, 10–20, (2018).
- [118] C. C. HUANG, R.G. WINKLER, G. SUTMANN and G. GOMPPER. *Macromolecules*, **43**, 10107–10116, (2010).
- [119] C. C. HUANG, G. SUTMANN, G. GOMPPER and R.G. WINKLER. *EPL (Europhysics Letters)*, **93**, 54004, (2011).

BIBLIOGRAPHY

- [120] D. A. FEDOSOV, S. P. SINGH, A. CHATTERJI, R.G. WINKLER and G. GOMPPER. *Soft Matter*, **8**, 4109–4120, (2012).
- [121] DIEGO JARAMILLO-CANO, CHRISTOS N LIKOS and MANUEL CAMARGO. *Polymers*, **10**, 860, (2018).
- [122] IOANA C. GÂRLEA, DIEGO JARAMILLO-CANO and CHRISTOS N. LIKOS. *Soft Matter*, **15**, 3527–3540, (2019).
- [123] CHRISTOS N LIKOS. *Soft Matter*, **2**, 478–498, (2006).
- [124] PRITI S MOHANTY, DIVYA PALOLI, JÉRÔME J CRASSOUS, EMANUELA ZACCARELLI and PETER SCHURTENBERGER. *J. Chem. Phys.*, **140**, 094901, (2014).
- [125] MAXIME J BERGMAN, NICOLETTA GNAN, MARC OBIOLS-RABASA, JANNE-MIEKE MEIJER, LORENZO ROVIGATTI, EMANUELA ZACCARELLI and PETER SCHURTENBERGER. *Nat. Commun.*, **9**, 5039, (2018).
- [126] S REDNER. *J. Phys. A: Math. Gen.*, **13**, 3525, (1980).
- [127] JOHN P VALLEAU. *J. Chem. Phys.*, **104**, 3071–3074, (1996).
- [128] CHRISTIAN MAYER and CHRISTOS N LIKOS. *Macromolecules*, **40**, 1196–1206, (2007).
- [129] BARRY J BAUER, LEWIS J FETTERS, WILLIAM W GRAESSLEY, NIKOS HADJICHRISTIDIS and GUENTHER F QUACK. *Macromolecules*, **22**, 2337–2347, (1989).
- [130] W. K. LIM and A. R. DENTON. *Soft Matter*, **12**, 2247–2252, (2016).
- [131] ALI GHAVAMI, HIDEKI KOBAYASHI and ROLAND G WINKLER. *J. Chem. Phys.*, **145**, 244902, (2016).
- [132] NICOLETTA GNAN, LORENZO ROVIGATTI, MAXIME BERGMAN and EMANUELA ZACCARELLI. *Macromolecules*, **50**, 8777–8786, (2017).
- [133] ANDREA NINARELLO, JÉRÔME J CRASSOUS, DIVYA PALOLI, FABRIZIO CAMERIN, NICOLETTA GNAN, LORENZO ROVIGATTI, PETER SCHURTENBERGER and EMANUELA ZACCARELLI. *arXiv preprint arXiv:1901.11495*, (2019).
- [134] SUNIL P SINGH, GERHARD GOMPPER and ROLAND G WINKLER. *J. Chem. Phys.*, **148**, 084901, (2018).

Curriculum vitae

Personal data:

Nationality: Colombian

Residence : Vienna

Birthdate: January 26, 1981

Email: diefejaca@hotmail.com

Tel: 004367761585187

Address: Pantzergasse 4/10, 1190, Vienna.

Diego Felipe Jaramillo – Cano.

Ph.D Student in Physics, Computational and Soft Matter Physics.
University of Vienna.

Academic formation:

Ph.D in Physics, Expected November 2020.

Computational and Soft Matter Physics, University of Vienna.

Thesis: Self-associating hybrid polymers under shear.

Advisor: Univ.-Prof. Dipl.-Ing. Dr. Christos N. Likos

Magister in Science-Physics. 2012.

Physics Department, Universidad de los Andes, Bogota, Colombia.

Thesis: Calculation of the distribution of wide terrace and the interaction potential of the TSK model from an equivalent system of classical particles.

Advisor: Dr. Gabriel Tellez, Dr. Diego Luis Gonzalez Cabrera.

Bachelor Degree in Physics, 2008.

Physics Degree Coordination, Universidad Distrital Francisco Jose de Caldas, Bogotá, Colombia.

Thesis: Chaos in classic systems: chaotic swinging toy.

Advisor: Dr. Luis Quiroga Puello.

Publications:

Diego Jaramillo-Cano, Manuel Camargo, Christos N. Likos, and Ioana C. Gârlea, *Dynamical properties of concentrated suspensions of block copolymer stars in shear flow*, submitted to publication, 2020.

José Ruiz-Franco, Diego Jaramillo-Cano, Manuel Camargo, Christos N. Likos, Emanuela Zaccarelli, *Multi-Particle Collision Dynamics for a coarse-grained model of soft colloids*, J. Chem. Phys. 151, 2019.

Ioana C Gârlea, Diego Jaramillo-Cano, Christos N Likos, *Self-organization of gel networks formed by block copolymer stars*, Soft Matter, 15(17), 2019.

Diego Jaramillo-Cano, Maud Formanek, Christos N. Likos, and Manuel Camargo, *Star Block-Copolymers in Shear Flow*, J. Phys. Chem. B, 122, 14, 2018.

Diego Jaramillo-Cano, Christos N. Likos, Manuel Camargo, *Rotation Dynamics of Star Block Copolymers under Shear Flow*, Polymers 10, 860, 2018.

Robert Paul Salazar, Gabriel Tellez, Diego Jaramillo-Cano, Diego Luis Gonzalez, *Chaos in the Diamond-Shaped Billiard with Rounded Crown*, Rev. Acad. Colomb. Cienc. Ex. Fis. Nat. 39(151), 2015.

Diego Jaramillo-Cano, Gabriel Tellez, Diego Luis Gonzalez, T. L. Einstein, *Interacting Steps With Finite-Range Interactions: Analytical Approximation and Numerical Results*, Phys. Rev. E, 87, 052405, 2013.